Proceedings of the

SIXTEENTH SYMPOSIUM ON ENERGY ENGINEERING SCIENCES

May 13-15, 1998

ARGONNE NATIONAL LABORATORY

Argonne, Illinois

Cosponsored by

Office of Basic Energy Sciences
U.S. DEPARTMENT OF ENERGY

and

Energy Technology Division
ARGONNE NATIONAL LABORATORY

Coordinated by

Argonne National Laboratory
9700 South Cass Avenue
Argonne, Illinois 60439

SIXTEENTH SYMPOSIUM ON ENERGY ENGINEERING SCIENCES

FOREWORD

This Proceedings Volume includes the technical papers that were presented during the Sixteenth Symposium on Energy Engineering Sciences on May 13-15, 1998, at Argonne National Laboratory, Argonne, Illinois. The Symposium was structured into eight technical sessions, which included 30 individual presentations followed by discussion and interaction with the audience. A list of participants is appended to this volume.

The DOE Office of Basic Energy Sciences (BES), of which Engineering Research is a component program, is responsible for the long-term, mission-oriented research in the Department. The Office has prime responsibility for establishing the basic scientific foundation upon which the Nation's future energy options will be identified, developed, and built. BES is committed to the generation of new knowledge necessary to solve present and future problems regarding energy exploration, production, conversion, and utilization, while maintaining respect for the environment.

Consistent with the DOE/BES mission, the Engineering Research Program is charged with the identification, initiation, and management of fundamental research on broad, generic topics addressing energy-related engineering problems. Its stated goals are to improve and extend the body of knowledge underlying current engineering practice so as to create new options for enhancing energy savings and production, prolonging the useful life of energy-related structures and equipment, and developing advanced manufacturing technologies and materials processing. The program emphasis is on reducing costs through improved industrial production and performance and expanding the nation's store of fundamental knowledge for solving anticipated and unforeseen engineering problems in energy technologies.

To achieve these goals, the Engineering Research Program supports approximately 130 research projects covering a broad spectrum of topics that cut across traditional engineering disciplines. The program focuses on three areas: (1) mechanical sciences, (2) control systems and instrumentation, and (3) engineering data and analysis. The Sixteenth Symposium involved approximately one-fourth of the research projects currently sponsored by the DOE/BES Engineering Research Program.

The Sixteenth Symposium was held under the joint sponsorship of the DOE Office of Basic Energy Sciences and Argonne National Laboratory (ANL). Local arrangements were handled by Ms. Jacquie Habenicht and Ms. Marianne Adair of ANL Conference Services. Ms. Gloria Griparis of ANL's Information and Publishing Division, Technical Communication Services was responsible for assembling these proceedings and attending to their publication.

I am grateful to all who contributed to the success of the program, particularly to the participants for their excellent presentations and active involvement in discussions. The resulting interactions made this Symposium a most stimulating and enjoyable experience.

Robert Goulard, ER-15
Division of Engineering and Geosciences
Office of Basic Energy Sciences

Proceedings of the

SIXTEENTH SYMPOSIUM ON ENERGY ENGINEERING SCIENCES

May 13-15, 1998

Argonne National Laboratory

Argonne, IL

TABLE OF CONTENTS

Technical Session III — Multiphase Flows 1

Technical Session IV — Multiphase Flows 2

Technical Session V — Turbulence

Technical Session VI — Systems

Technical Session VII — Plasmas

Technical Session VIII — Nonlinear Fluid Dynamics

SPECTRAL PROPERTIES OF A BALLISTIC ELECTRON WAVEGUIDE

L. E. Reichl and Kyungsun Na

Center for Studies in Statistical Mechanics and Complex Systems
The University of Texas at Austin, Austin, TX 78712, U.S.A.

ABSTRACT

Low frequency conductance measurements on ballistic electron waveguides can yield useful information about the spectral properties of electrons in the waveguide. This information, in turn, can be used to estimate the amount of power absorbed by the waveguide in the presence of high frequency fields. High frequency fields can excite quasibound states in the waveguide.

THEORY

Our study of electron waveguides is part of a larger DOE project to study mechanisms underlying the emergence of decay processes in open quantum systems [1, 2, 3, 4], chaotic classical dynamics [5], and in addition to study the interface between these systems and the thermodynamic description of decay processes [6]. These questions are of particular importance at mesoscopic and atomic scales where one hopes to build controllable electron devices. Electron waveguides provide a laboratory for studying the quantum dynamics of open quantum systems. Near equilibrium this dynamics is controlled by spectral properties induced by waveguide channel shapes and impurities. At low temperatures, the strength of the coupling of the electrons in the waveguide to the thermal heat bath is determined by the size of the waveguide relative to the electron-phonon mean free path, L_{el-ph}. For devices smaller than this and smaller than electron-electron coulomb mean-free-path, L_{el-el}, the electron dynamics is determined only by wall shapes and impurities. Even at this level, the "free" electron dynamics can be very rich. The electrons in the waveguide form a two-dimensional Fermi gas. The Fermi momentum is determined by the density of electrons. Waveguide shape can induce bound states and quasibound states (as defined by singularities of the energy Green's function) in addition to the effects introduced by the continuous spectrum, even for noninteracting electrons. We will show some of these effects below.

Electron waveguides can be formed at the interface of semiconductor materials such as, for example, a GaAs/AlGaAs interface. Negatively charged metal gates on the AlGaAs surface force electrons out of the regions below them at the interface. In this way, the two dimensional electron gas at the interface can be confined to well defined waveguide shapes at the interface. The conduction properties of these systems is governed by the spectral properties of the energy Green's function for electrons in the channel. For simplicity we focus on the waveguide shape shown in Figure 1.

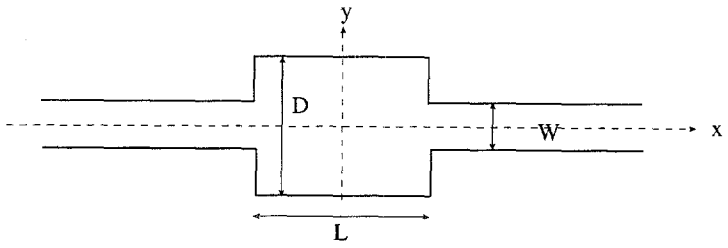

Figure 1. The waveguide.

First however, it is useful to consider a straight waveguide without a cavity. In the absence of cavities or bends in the waveguide, the electron energy spectrum is continuous along the direction of propagation and discrete along the direction transverse to the propagation direction. The different transverse states of the electron are called "channels". The energy of an electron in the n^{th} channel is

$$E = \frac{\hbar^2}{2m}[k_n^2 + (\frac{n\pi}{W})^2], \tag{1}$$

where n is an integer, m is the effective mass of the electron in the semiconductor material. Let $\epsilon_n = \frac{\hbar^2}{2m}(\frac{n\pi}{W})^2$. For Fermi energy, $E_f < \epsilon_1$. there is no propagation in the waveguide. For $\epsilon_1 < E_f < \epsilon_2$, one "channel" can propagate. For $\epsilon_n < E_f < \epsilon_{n+1}$, n channels can propagate. The retarded energy Green's function for the totally straight waveguide is

$$G(\mathbf{r}_1, \mathbf{r}_2; E + i\delta) = \frac{2m}{i\hbar^2 W}\sum_n \sin(\frac{n\pi y_1}{W})\sin(\frac{n\pi y_2}{W})\frac{e^{ik_n^+|x_1 - x_2|}}{k_n^+}, \tag{2}$$

where $k_n^+ = \sqrt{\frac{2m}{\hbar^2}}\sqrt{E - \epsilon_n + i\delta}$. Each channel is represented by a branch cut. For the n^{th} channel, the branch point is at energy, ϵ_n.

For the waveguide in Figure 1, the conduction is more complicated. Let x_L be a point to the left of the cavity and x_R a point to the right of the cavity. The conduction from a point to the left to a point to the right is given by the Landauer-Büttiker formula [7],

$$G = \frac{2e}{h}\sum_{i=1}^{n_c}\sum_{j=1}^{n_c}|T_{ij}|^2, \tag{3}$$

where T_{ij} is the transmission probability amplitude from channel i at x_L to channel j at x_R, and n_c is the maximum number of channels that can propagate at the given energy. For an energy range, $\epsilon_1 < E_f < \epsilon_2$, where only a single propagating mode exists in the leads, the retarded energy Green's function, $\hat{G}^+(E) = (E - \hat{H} + i\delta)^{-1}$, in the leads can be written $\hat{G}^+_{E_f}(x_L, y_L; x_R, y_L) = \frac{2}{W}g^+_{E_f}(x_L, x_R)\sin(\frac{\pi y_L}{W})\sin(\frac{\pi y_R}{W})$, where x is the longitudinal coordinate and y is the transverse coordinate. The transmission probability

amplitude from channel 1 in the left lead to channel 1 in the right lead is related to the Green's function [8,9] as

$$T_{11}(E_f) = \frac{i\hbar^2 k_{f,1}}{m} e^{ik_{f,1}(x_R - x_L)} g^+_{E_f}(x_L, x_R). \tag{4}$$

Thus, conduction measurements, at least for a few channels, can give us valuable information about the spectral properties of the waveguide.

In Figure 2 we show the transmission probability, $|T_{11}|^2$, for the waveguide in Figure 1 for two different cavity widths, $D = 120\mathring{A}$ (2.a) and $D = 200\mathring{A}$ (2.b). For both Figure 2(a) and 2(b), the cavity length is $L = 371.66\mathring{A}$ and the lead width is $W = 100\mathring{A}$. We see some interesting features in the conduction. An essential feature in understanding these plots is the shape of the cavity. Consider a closed rectangular billiard with the same size and shape as our cavity. Its energy eigenvalues are shown as black dots below the horizontal axis. The symmetries that determine the eigenstates of the billiard also strongly influence the waveguide. The waveguide cavity favors standing wave structures of similar probability distribution as the eigenstates of the billiard. The eigenstates of the billiard and standing wave structures in the cavity can be characterized by the number of transverse antinodes, n. Let us now consider Figure 2. At an energy of $E_f \approx 0.075$eV, there is an abrupt rise, from $|T_{11}| = 0$ to $|T_{11}| \approx 1$, in the transition probability. This is the lower edge of the conduction band of the 1^{st} channel. It appears in the Green's function as a branch point of a cut along the real energy axis.

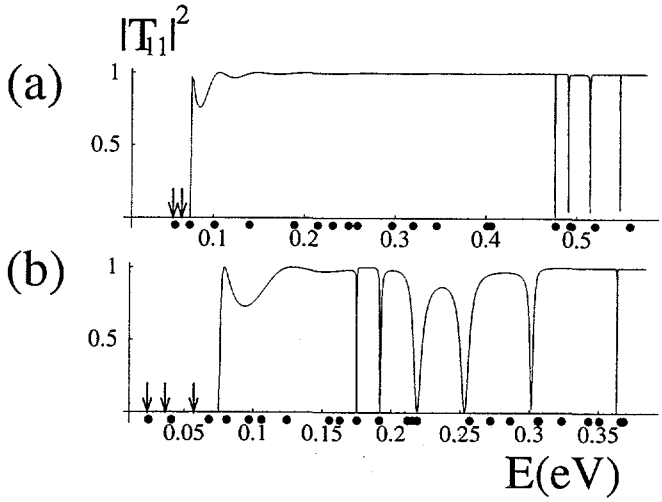

Figure 2a. Transmission probability versus Fermi energy for $W = 100\mathring{A}, L = 371.66\mathring{A}$, and $D = 120\mathring{A}$. Figure 2b. Transmission probability versus Fermi energy for $W = 100\mathring{A}$, L=371.66Å, and $D = 200\mathring{A}$.[1]

The two arrows in Figure 2(a) and the three arrows in Figure 2(b) are bound states of the waveguide. These are the waveguide analogs of the two bound states of the rectangular billiard which occur near those energies. These bound state are stable because they occur at energies below the conduction energy of the first channel in the waveguide. An electron in such a state has no way to escape from the cavity. These positive energy bound states

appear as poles on the real energy axis of the energy Green's function. The bound states for $E_f < \epsilon_1$, in Fig. 2.a are shown in Figure 3.

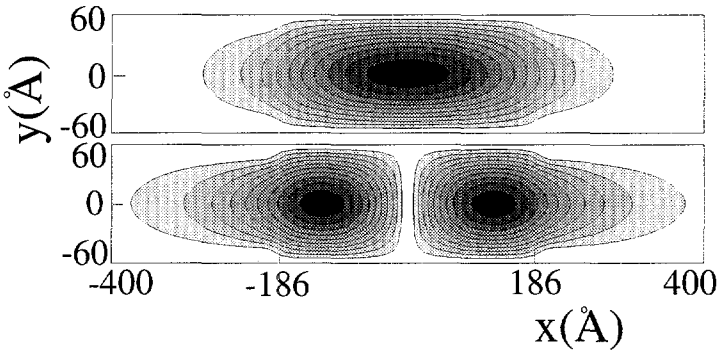

Figure 3. Waveguide bound states indicated by arrows in Figure 2(a).[1]

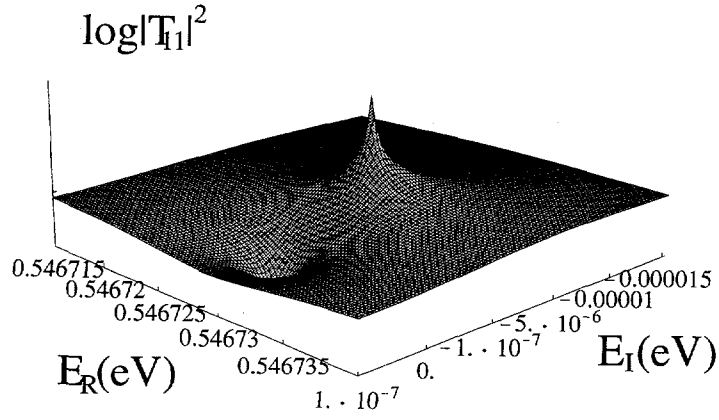

Figure 4. The complex energy pole which gives rise to the fourth conduction zero in Figure 2(a).[1]

For energies, $E_f > \epsilon_1$, we see several points where the conductance suddenly drops to zero. These result from quasi-bound states in the waveguide. Because of symmetries, electrons propagating in the first channel can not excite cavity structures with transverse quantum number $n = 2$, but they can excite structures with $n = 3$. These are the source of the conductance zeros in Figures 2(a) and 2(b). They are the result of quasibound states that can be formed in the cavity. Quasibound states are unstable. They have a finite lifetime which is proportional to the width of the conduction zero. They appear as poles in the complex energy plane of the energy Green's function. The pole corresponding to the fourth conduction zero in Figure 2(a) is shown in Figure 4. The distance of the pole from the real energy axis determines the lifetime of the quasibound state. The quasibound state shown in Figure 4 has a lifetime of $\tau = 9.14 \times 10^{-11}$sec. This lifetime is fairly typical of quasibound states in systems of this size.

Knowledge of spectral properties of the energy Green's function can be used to compute power absorption by the waveguide from external fields [2]. Let us consider a weak localized potential pulse applied to the waveguide. We assume that the electric field,

$e\mathrm{E}(x)\cos(\omega t)$, associated with this potential pulse is localized over a distance, d, greater than the cavity and it is centered on the cavity. We also assume that it varies only in the x-direction. We can use linear response theory [8, 10] to compute the power absorbed by electrons in the waveguide due to the potential pulse. The power absorption is determined by the spectral properties of the waveguide. The average power absorbed over one period of the applied field is

$$\Gamma(\omega_o) = e\int_0^{T_o}\int dx\ \langle J_x(t)\rangle\ \mathrm{E}(x)\cos(\omega_o t)$$

$$\sim \int dx \int dx'\ \mathrm{E}(x)\mathrm{E}(x') \int_0^{2\pi/\omega_o} d\tau \int dt \int dt'\ \cos(\omega_o t)\ \cos(\omega_o t')$$

$$\langle \hat{J}_x(x)\hat{G}^+(t)\hat{J}_x(x)\hat{G}^-(t')\rangle, \tag{5}$$

where $\hat{G}^+(t)$ and $\hat{G}^-(t)$ are the retarded and advanced Green's functions for the electron in the waveguide.

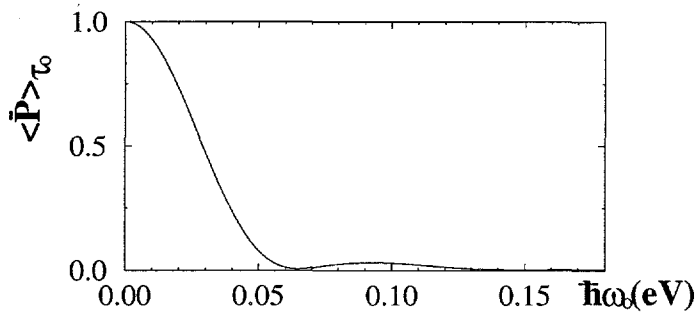

Figure 5. Average power absorption for a straight waveguide of width $W = 100\text{Å}$.

The power absorption for the straight channel can be computed exactly. For the energy interval with only one propagating mode and for $\hbar\omega_o \ll E_f$ it is [11]

$$\Gamma(\omega_o) = \left(\frac{\sin(\frac{dm\omega_o}{\hbar v_{f,1}})}{\frac{dm\omega_o}{\hbar v_{f,1}}}\right)^2, \tag{6}$$

where $v_{f,1} = \sqrt{k_f^2 - (\pi/W)^2}$. The power absorption for a waveguide with a cavity cannot be computed analytically. But it can be found numerically by using a closely spaced set of discrete energy eigenstates of the waveguide [2]. The spectral properties of the electron in the unperturbed waveguide completely determines the qualitative behavior of the power absorption. In Figure 5 we show power absorption for the straight waveguide. The continuous spectrum gives a continuous absorption as a function of the frequency of the applied field.

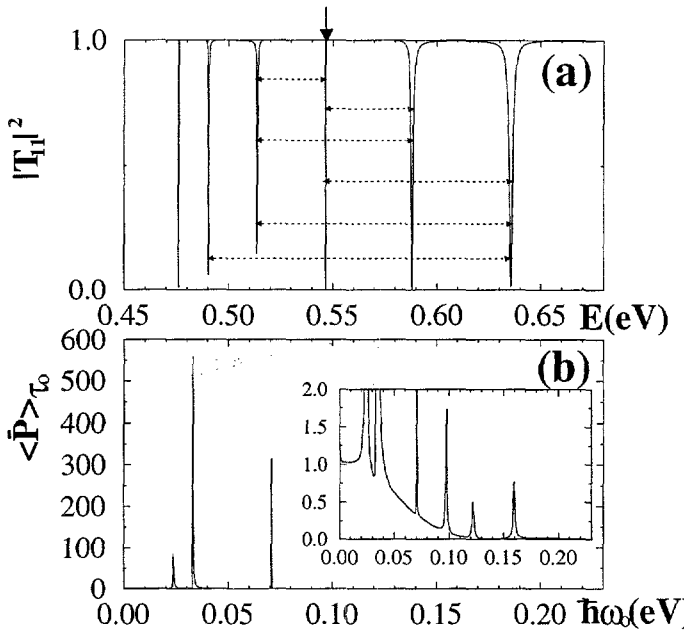

Figure 6. Average power absorbed by for cavity width, $D = 120\mathring{A}$ and Fermi energy, $E_f = 0.54672$eV.

In Figure 6 we show the power absorption for the waveguide with cavity for the case shown in Figure 2(a). There are peaks in the power absorption at the energy differences of the poles. The applied pulse favors transitions between the quasibound states of the waveguide.

ACKNOWLEDGEMENTS

The authors wish to thank DOE Grant No. DE-FG03-94ER14405 for support of this work, and the University of Texas at Austin High Performance Computing Center for use of their computer facilities. We also thank Alex de Lozanne for helpful discussions concerning experiments.

REFERENCES

1. KYUNGSUN NA and L.E. REICHL, "Electron Conductance and Lifetimes in a Ballistic Electron Waveguide", *J. Stat. Phys.* August (1998).
2. KYUNGSUN NA and L.E. REICHL, "Power Absorption and Quasi-bound State Excitation in a Ballistic Electron Waveguide", Preprint, The University of Texas at Austin, May (1998).
3. SUHAN REE and L.E. REICHL, "Aharonov-Bohm effect and Resonances in a circular quantum billiard", Preprint, The University of Texas at Austin, February (1998).
4. J. C. NICKEL and L.E. REICHL, "Intrinsic Decay Times and Spectral Widths of a Simple Hamiltonian System", Preprint, The University of Texas at Austin, February (1998).
5. See, for example, D.J. DRIEBE and G. ORDONEZ, "Polynomial shift states of a

chaotic map", *J. Stat. Phys.* 89 1087 (1997); D.J. DRIEBE, "Jordan blocks in a one-dimensional Markov map", *Computers Math. Applic.* 34 103 (1997).

6. See, for example, T. PETROSKY and I. PRIGOGINE, "The Liouville Space Extension of Quantum Mechanics," *Advances in Chemical Physics*, Volume 99, eds. I. Prigogine and S. Rice (John Wiley and Sons, 1997); T. PETROSKY and G. ORDONEZ, "Liouville extension of quantum mechanics: One-dimensional gas with function interaction", *Phys. Rev. A* 56 (1997).
7. R. LANDAUER, "Electrical Resistance of Disordered One- Dimensional Lattices", *Phil. Mag.* 21 863 (1970); R. LANDAUER, "Conductance Determined by Transmission:Probes and quantized constriction Resistance", *J. Phys.: Condens. Matter* 1 8099 (1989); M. BÜTTIKER, "Four Terminal Phase-Coherent Conductance", *Phys. Rev. Lett.* 57 1761 (1986).
8. D.S. FISHER and P.A. LEE, "Relation between Conductivity and Transmission Matrix", *Phys. Rev. B* 23 6851 (1981).
9. G. GARCIA-CALDERON, A. RUBIO, and R. ROMO, "Decay Widths for Double Barrier Resonant Tunneling", *J. Appl. Phys.* 69 3612 (1991).
10. R. KUBO, "A General Expression for the Conductivity Tensor", *Can. J. Phys.* 34 1274 (1956); H.U. BARANGER and A.D. STONE, "Electric Linear-Response Theory in an Arbitrary Magnetic Field:A New Fermi-Surface Formation, *Phys. Rev. B* 40 8169 (1989).
11. T.BRANDES, W. HÄUSLER, K. JAUREGUI, B. KRAMER, and D.WEINMANN, "Coulomb Interaction and Transport in Tunnel Junctions and Quantum Dots", *Physica B* 189 16 (1993), J.MASEK and B.KKRAMER, "On the Conductance of Finite Systems in the Ballistic Regime:Dependence of Fermi Energy, Magnetic Field, Frequency and Disorder", *Z Phys. B - Condens. Matter* 75 37 (1989).

CORRELATION-INDUCED SPECTRAL CHANGES AND ENERGY CONSERVATION

Emil Wolf

Department of Physics and Astronomy and Rochester Theory Center for Optical Science and Engineering, University of Rochester, Rochester, NY 14627, USA

ABSTRACT

A brief account is presented of recent researches relating to the phenomenon of correlation–induced spectral changes. After a discussion of the question of consistency of this phenomenon with energy conservation, some examples of its application are noted.

INTRODUCTION

It has become rather clear from researches carried out during the last few years that there are some basic questions concerning spectra of light and other radiation, which have completely escaped the attention of physicists. This claim may perhaps seem less surprising if we recall that traditional spectroscopy deals mainly with radiation produced by thermal sources. Because such sources radiate largely by the process of spontaneous emission they are spatially highly incoherent. In more recent times sources have been developed which are essentially fully coherent, such as single mode lasers or are partially coherent, i.e. they are neither completely coherent nor fully incoherent. Among them are some X–ray sources but there are others. It turns out that the spectrum of a field generated by a partially coherent source may differ – sometimes very drastically – from the source spectrum. Moreover, it has been predicted theoretically some years ago that the spectrum of light and of other radiation may change on propagation, even in free space. This phenomenon has attracted a good deal of attention and has by now resulted in the publication of well over 100 papers on this subject, both theoretical and experimental ones [1].

The spectral changes, which have their origin in spatial correlation properties of the source, may be of very different kinds. They may, for example, consist of redshifts or blueshifts of spectral lines, narrowing or broadening of the lines or generation of new ones. Moreover, different spectral changes may occur in different directions of observation.

It may appear at first sight that correlation–induced spectral changes violate energy conservation. That this is not so was demonstrated under somewhat restricted circumstances in several papers [2-4]. We have recently derived a general energy conservation law for fields generated by random, statistically stationary sources of any state of coherence and we have shown

that correlation–induced spectral changes do not violate this law [5]. We have also formulated a generalized optical cross–section theorem for fields of arbitrary states of coherence [6]. In the first part of my talk I will present a brief account of some of these investigations. In the second part I will briefly discuss some potential applications of this phenomenon.

SPECTRUM OF THE RADIATED FIELD

For the sake of simplicity we will base our analysis on scalar theory of statistical wave fields. A treatment based on electromagnetic theory has also recently been obtained [7].

Consider a fluctuating source occupying a finite domain D. Let $p(\mathbf{r},t)$ denote the source density distribution (which may be regarded as a scalar analogue of the polarization density) at a point $\mathbf{r}$, at time t and let $E(\mathbf{r},t)$ be the field generated by the source. We take $p(\mathbf{r},t)$ and $E(\mathbf{r},t)$ to be the complex analytic signal representations of a real source variable and a real field variable (ref. 8, Sec. 3.1). Both $p(\mathbf{r},t)$ and $E(\mathbf{r},t)$ are considered to be random variables. We assume that their temporal fluctuations are characterized by ensembles that are statistically stationary. Let

$$\tilde{p}(\mathbf{r},\omega) = \frac{1}{2\pi}\int_{-\infty}^{\infty} p(\mathbf{r},t)\, e^{i\omega t} dt \tag{1}$$

be the temporal Fourier transform of $p(\mathbf{r},t)$, with a similar definition of the temporal Fourier transform $\tilde{E}(\mathbf{r},\omega)$ of $E(\mathbf{r},t)$ [9]. The spectrum $S_p(\mathbf{r},\omega)$ of the source distribution and the spectrum $S_E(\mathbf{r},\omega)$ of the field distribution may then be defined by the formulas ([8], p. 58)

$$\left\langle \tilde{p}^*(\mathbf{r},\omega)\tilde{p}(\mathbf{r},\omega')\right\rangle = S_p(\mathbf{r},\omega)\,\delta(\omega-\omega'), \tag{2a}$$

$$\left\langle \tilde{E}^*(\mathbf{r},\omega)\tilde{E}(\mathbf{r},\omega')\right\rangle = S_E(\mathbf{r},\omega)\,\delta(\omega-\omega'), \tag{2b}$$

It follows from elementary radiation theory (cf. [5], Sec. II) that the field at frequency ω, at a point P specified by position vector $\mathbf{r} = r\mathbf{u}$, ($\mathbf{u}^2 = 1$), in the far zone (see Fig. 1), is given by the formula

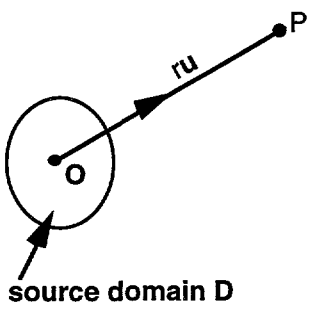

$$\tilde{E}^{(\infty)}(\mathbf{ru},\omega) \sim k^2 \frac{e^{ikr}}{r} \int_D \tilde{p}(\mathbf{r}',\omega)\, e^{-ik\mathbf{u}\cdot\mathbf{r}'}\, d^3\mathbf{r}', \tag{3}$$

where $k = \omega/c$, c being the speed of light in vacuo. On substituting from Eq. (3) into Eq. (2b) one readily finds that the spectrum of the far field is given by the formula

$$S_E^{(\infty)}(\mathbf{ru},\omega) = \frac{k^4}{r^2} \int_D \int_D W_p(\mathbf{r}',\mathbf{r}'',\omega) e^{-ik\mathbf{u}.(\mathbf{r}''-\mathbf{r}')}\, d^3\mathbf{r}' d^3\mathbf{r}'', \tag{4}$$

where $W_p(\mathbf{r}',\mathbf{r}'',\omega)$ is the cross–spectral density of the polarization, defined by the generalization of Eq. (2a):

$$\langle \tilde{p}^*(\mathbf{r}',\omega)\, \tilde{p}(\mathbf{r}'',\omega') \rangle = W_p(\mathbf{r}',\mathbf{r}'',\omega)\, \delta(\omega - \omega'). \tag{5}$$

If we introduce the spectral degree of coherence of the source density by the formula

$$\mu_p(\mathbf{r}',\mathbf{r}'',\omega) = \frac{W_p(\mathbf{r}',\mathbf{r}'',\omega)}{\sqrt{S_p(\mathbf{r}',\omega)}\ \sqrt{S_p(\mathbf{r}'',\omega)}} \tag{6}$$

and assume that the source spectrum is the same at every source point [i.e. that $S_p(\mathbf{r},\omega) \equiv S_p(\omega)$] we readily find that the spectrum of the far field is given by the expression

$$S_E^{(\infty)}(\mathbf{r},\omega) = M(\omega,\mathbf{u},r)\, S_p(\omega), \tag{7}$$

where

$$M(\omega,\mathbf{u},r) = \frac{k^4}{r^2} \int_D \int_D \mu_p(\mathbf{r}',\mathbf{r}'',\omega)\, e^{-ik\mathbf{u}.(\mathbf{r}''-\mathbf{r}')}\, d^3\mathbf{r}' d^3\mathbf{r}''. \tag{8}$$

The formula (7), together with Eq. (8), shows that the spectrum $S_E^{(\infty)}$ of the far field depends not only on the source spectrum S_p but also on the correlation properties of the source, as first predicted in ref. [10] for fields generated by sources of a simpler class. Moreover, because the "spectral modifier "$M(\omega, \mathbf{u}, r)$ in Eq. (7) depends on the unit vector $\mathbf{u}$, the spectrum of the far field will be different, in general, in different directions of observation.

CONSISTENCY OF CORRELATION–INDUCED SPECTRAL CHANGES WITH ENERGY CONSERVATION

In order to show that the changes in spectra of the radiated field which are caused by source correlations do not violate energy conservation it is necessary to formulate an energy conservation law for random fields whose statistical properties are represented by stationary ensembles. Such a

conservation law was derived in ref. 5. Because of limitations of space we will only briefly indicate its derivation.

The flux vector $\mathbf{F}_\omega(\mathbf{r})$ of the field may be defined by the formula

$$\mathbf{F}_\omega(\mathbf{r})\delta(\omega-\omega') = -\frac{i}{2k}\left[\left\langle \tilde{E}^*(\mathbf{r},\omega)\nabla\tilde{E}(\mathbf{r},\omega') - \tilde{E}(\mathbf{r},\omega')\nabla\tilde{E}^*(\mathbf{r},\omega)\right\rangle\right]. \tag{9}$$

If one expresses $\tilde{E}$ in terms of the source distribution p, takes the divergence of both sides, uses several vector identities and integrate the resulting expression over a surface σ enclosing the source one finds [for details see Sec. III of ref. 5] that

$$\int_\sigma \mathbf{F}_\omega(\mathbf{r})\cdot\mathbf{n}d\sigma = 4\pi k^4 \int_D\int_D W_p(\mathbf{r},\mathbf{r}',\omega)\,\frac{\sin\left(k|\mathbf{r}-\mathbf{r}'|\right)}{k|\mathbf{r}-\mathbf{r}'|}\,d^3r\,d^3r'. \tag{10}$$

Formula (10) is the integral form of a *new energy conservation law for statistically stationary fields of any state of coherence.*

In order to show that correlation–induced spectral changes do not violate energy conservation we use the well–known fact that in the far zone the flux vector and the spectral densities are, (with a suitable choice of units), related by the simple formula ([8], Eq. (5.7-32)]

$$\mathbf{F}_\omega^{(\infty)}(r\mathbf{u}) = S_E^{(\infty)}(r\mathbf{u},\omega)\,\mathbf{u}. \tag{11}$$

If one integrates the outward normal components of this equation over a large sphere centered at a point in the source domain and uses the expression (4) for $S_E^{(\infty)}$ one finds that

$$\int_{(4\pi)} \mathbf{F}_\omega^{(\infty)}(r\mathbf{u})\cdot\mathbf{u}\,r^2d\Omega = k^4\int_{(4\pi)}d\Omega\int_D\int_D W_p(\mathbf{r}',\mathbf{r}'',\omega)\,e^{-ik\mathbf{u}\cdot(\mathbf{r}'-\mathbf{r}'')}\,d^3r'd^3r'', \tag{12}$$

where we have used the fact that an element of a spherical surface of radus r is equal to $r^2d\Omega$, $d\Omega$ denoting an element of solid angle. The angular integrations are taken over the whole 4π solid angle generated by the unit vector $\mathbf{u}$. If we interchange the order of the integrations on the right and use the well–known identity [ref. 8, p. 123]

$$\int_{(4\pi)} e^{-ik\mathbf{u}\cdot(\mathbf{r}-\mathbf{r}')}d\Omega = 4\pi\,\frac{\sin\left(k|\mathbf{r}-\mathbf{r}'|\right)}{k|\mathbf{r}-\mathbf{r}'|} \tag{13}$$

Eq. (12) reduces to the energy conservation law (10). Since in obtaining this result we have used the formula (4) for the far zone spectrum, we have demonstrated that correlation–induced spectral changes are in agreement with the law of conservation of energy. Such changes will be generated by most partially coherent sources, including sources with spherical symmetry, a fact which perhaps may not be entirely surprising if one realizes that the spectrum of a source and the spectrum of a field are physically quite different entities. This distinction, which is obviously relevant to spectroscopy, does not appear to have been generally recognized until very recently.

SOME APPLICATIONS

Several applications of the phenomenon of correlation–induced spectral changes are currently being investigated. We will briefly mention some of them.

A potential application is to remote sensing. Suppose that one wishes to determine the angular diameters and the angular separation of two identical, spatially incoherent, circular sources, e.g. a double star, from measurements made far away from them (see Fig. 2). The principle of

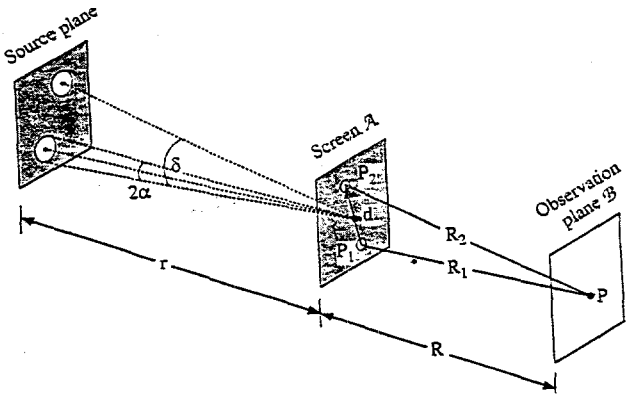

Fig. 2 Configuration illustrating the principle of the method for determining the angular diameter and angular separation of double stars from spectroscopic measurements.

the method is illustrated in Fig. 2. One passes light from the two sources through small openings at points P_1 and P_2 in an opaque screen $\mathcal{A}$. Even though the light from the two sources is spatially incoherent, it becomes partially coherent when it reaches the openings, as a result of propagation and superpostion ([8], Sec. 4.4.4). The degree of coherence of the light at P_1 and P_2 gives rise to spectral changes in the plane of observation $\mathcal{B}$ (See Fig. 3). From the modulation which the spectrum exhibits one can determine the stellar diameter and the angular separation of the two sources [11]. This prediction was confirmed by laboratory experiments [12].

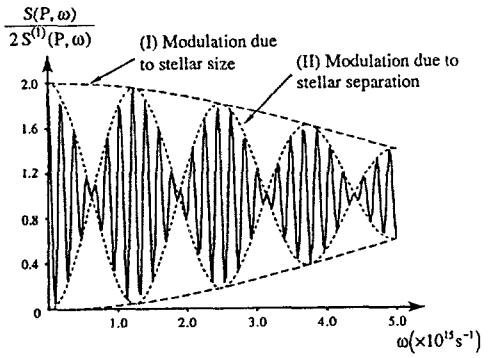

Fig. 3 Illustrating the changes in the spectrum produced on superposing two beams at a point P, from two identical stellar source. $S(P,\omega)$ is the spectrum at P when the light reaches this point via both the openings and $S^{(1)}(P,\omega)$ is the spectrum which would be produced at P if the light, assumed to originate in a blackbody source, was passed through only one of the openings. For details see ref. [11].

The phenomenon of correlation–induced spectral changes also offers a possibility for constructing new types of spectral filters, called coherence filters ([13], [14]). They are based on the fact that one can change the degree of coherence of a source by the use of a suitable optical system. A very versatile system of this kind, is shown schematically in Fig. 4.

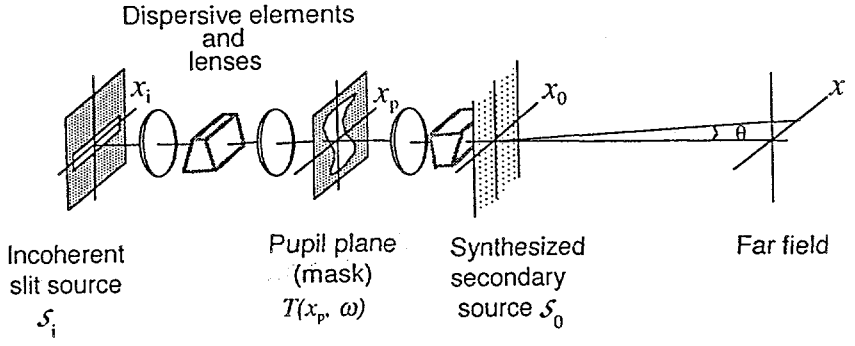

Fig. 4 A schematic diagram of an optical system due to Indebetow [15], for synthesizing a partially coherent secondary source S_0 from an incoherent source S_1. The degree of coherence of the synthesized source can be controlled by an appropriate choice of the pupil mask in the plane x_p, y_p. For fuller description of the system see [14] or [15].

In the far–zone, the spectrum $S^{(\infty)}(\mathbf{ru}, \omega)$ at a distance r from the synthesized source, in a direction specified by a unit vector $\mathbf{u}$, is given by the formula {[13], Eq. (9)}

$$S^{(\infty)}(\mathbf{ru}, \omega) = F(\omega, r, \mathbf{u})\, S^{(0)}(\omega), \tag{14}$$

where $S^{(0)}(\omega)$ is the spectrum of the synthesized source. The function $F(\omega, r, \mathbf{u})$ which, for obvious reasons is called the *filter function*, depends on the coherence properties of the synthesized source which, in turn, depends on the choice of the transmission function of the pupil mask (for detail see [13] and [14]).

An interesting property of coherence filters is that their filtering properties depend on the direction of observation (indicated by the dependence of the filter function on the unit vector $\mathbf{u}$). This property could be used, for example, to fascilitate search for presence of particular lines in the spectra of astronomical sources because the transmission function of the pupil mask can be chosen so as to transmit each particular line of interest in a chosen direction of observation [14].

Another potential application of coherence filters, also discussed in ref. [14], is for signal coding, e.g. for use in cryptography, illustrated in Fig. 5. Information could be encoded in the pupil mask in the form of a checkerboard, for example. The filter functions for different directions of observation carry information stored in the different vertical strips of the pupil mask.

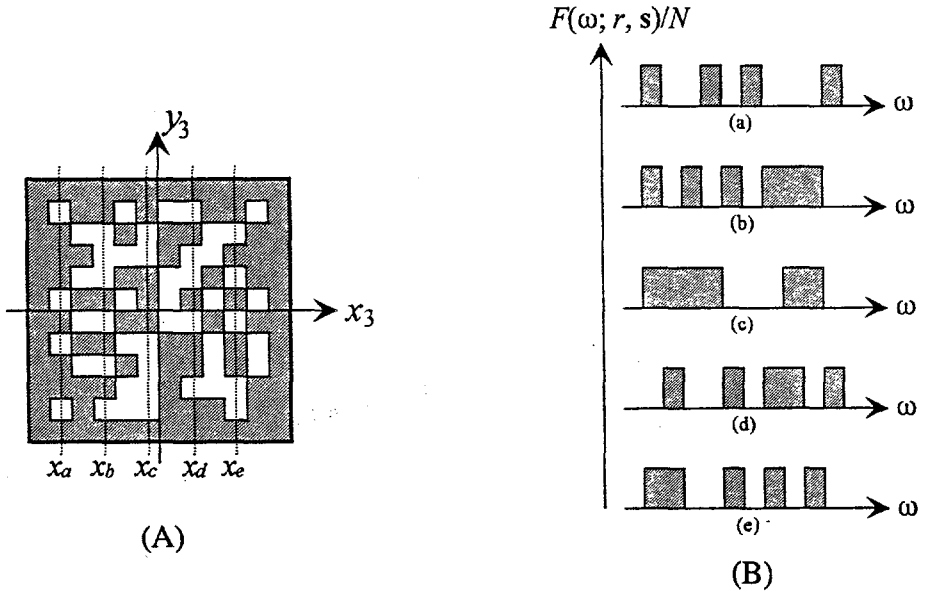

Fig. 5 Illustrating potential use of coherence filters for cryptography. The information is coded into the pupil mask (A) and can be recovered from measurements of the filtered spectra generated by the synthesized partially coherent secondary source which the mask generates (B). (Reproduced from [14]).

It should be clear from this brief overview that the phenomenon of correlation–induced spectral changes has revealed some rather unsuspected properties of light. They are of considerable relevance for spectroscopy and they suggest some interesting applications.

ACKNOWLEDGEMENT

Most of the research described in this talk was supported by the Department of Energy under grant DE-FG02-90ER 14119 and by the Air Force Office of Scientific Research under grant F49620-96-1-0400.

1. For a review of these publications, see E. WOLF and D. F. V. JAMES, *Rep. Progr. Phys.* (IOP Publishing, Bristol and London, 59, 771 (1996).
2. E. WOLF and A. GAMLIEL, *J. Mod. Opt.* 39, 927 (1992).
3. M. DUSEK, *Opt. Commun.* 100, 24 (1993).
4. G. HAZAK and R. ZAMIR, *J. Mod. Opt.* 41, 1653 (1994).
5. G. S. AGARWAL and E. WOLF, *Phys. Rev.* A 54, 4424 (1996).
6. P. S. CARNEY, E. WOLF and G. S. AGARWAL, *J. Opt. Soc. Amer. A* 14, 3366 (1997).
7. G. GBUR, D. F. V. JAMES and E. WOLF, submitted to *Phys. Rev. A.*
8. L. MANDEL and E. WOLF, *Optical Coherence and Quantum Optics*, Cambridge University Press, Cambridge (1995).
9. Because the realizations of stationary random processes do not die out as $t \to \pm\infty$ the Fourier transforms have to be interpreted as generalized functions.
10. E. WOLF, *Phys. Rev. Lett* . 56, 1370 (1986).
11. D. F. V. JAMES, H. C. KANDPAL and E. WOLF, *Astrophys. J.* 445, 406 (1995).
12. H. C. KANDPAL, K. SAXENA, D. S. MEHTA, J. S. VAISHYA and K. C. JOSHI, *J. Mod. Opt.* 42, 447 (1995).

13. E. WOLF, T. SHIRAI, H. CHEN and W. WANG, *J. Mod. Opt.* 44, 1345 (1997).
14. T. SHIRAI, E. WOLF, H. CHEN and W. WANG, *J. Mod. Opt.* 45, 799 (1998).
15. G. INDEBETOW, *J. Mod. Opt.* 36, 251 (1989).

SUB-SINGLE-ELECTRON CHARGE TRANSFER AND SHOT NOISE IN NANOSTRUCTURES

Konstantin K. Likharev

State University of New York at Stony Brook, Stony Brook, NY 11794-3800

ABSTRACT

The interplay of quasi-continuous (sub-single-electron) and discrete (single-electron) charge transfer is the basis for several physical phenomena predicted and observed since the mid-1980s, including single-electron-tunneling (SET) and Bloch oscillations. From the applications perspective, these effects are currently considered to be the only possible basis for the implementation of logic single-electron devices and circuits, since they allow the problem of random background charge to be circumvented. More generally, the crossover between continuous and discrete charge transfer is a key issue for the development of any nanoscale electronics device. We have carried out a quantitative analysis of the crossover in nanostructures with diffusive conduction using the "drift-diffusion-Langevin" equation, taking into account the effects of screening, as well as electron-electron and electron-phonon scattering. Our main result is that the charge transfer discreteness δQ becomes small (~0.1 e) when the nanostructure length becomes about two orders of magnitude larger than the electron-phonon scattering length.

INTRODUCTION

In recent years single-electronics (for general reviews, see, e.g., Refs. 1) has become a major field of fundamental and applied physics, with hundreds of papers published annually. Numerous experiments with semiconductor, metallic, and superconductor single-electron devices and their theoretical analyses have made some substantial contributions to solid state physics. Moreover, single-electron tunneling has made possible the new and distinct field of single-electron spectroscopy (for a recent review, see Ref. 2). Several applications of single-electron devices in analog electronics, including supersensitive electrometry, absolute thermometry, and fundamental standards of current, are also being actively developed. There are also interesting opportunities in terahertz wave detection and imaging; for a recent review see, e.g. Ref. 3.

The situation with digital applications is much more complex [3]. While single-electron devices may potentially make possible integrated circuits of unparalleled density (beyond 10^{11} gates per cm^2), they face a substantial obstacle: the randomness of background ("offset") charges. Almost all the single-electron logic devices currently being proposed are vulnerable to this effect which essentially precludes their use in circuits of any appreciable integration scale. An important exception are single-electron devices using resistive coupling between charged islands, including R-SET logic [4] and tunneling phase logic (TPL) [5], which are insensitive to offset charges. These devices, however, face another major

challenge: their operation needs the coexistence of two different mechanisms of charge transfer: *discrete* and *continuous* (for a popular review of this issue, see Ref. 6).

For example, current due to tunneling through an energy barrier with low transparency can be described as the result of *discrete* jumps of single electrons, each carrying the fundamental unit of charge, e. The best known consequence of this discrete electron transfer is "shot noise" in tunnel junctions (for a comprehensive review, see Ref. 7). At not very high temperatures ($k_BT < eV/2$, where V is the voltage drop across the barrier), and not very high observation frequencies ω ($\hbar\omega < eV/2$), this noise may be described with the famous Schottky formula

$$S_I(\omega) = 2eI, \tag{1}$$

in which S_I is the spectral density of current fluctuations, and I is the average tunneling current.

On the other hand, macroscopic metallic conductors do *not* exhibit shot noise. This is evidence of *continuous* charge transfer inside these conductors, i.e. their ability to transfer sub-single-electron amounts of charge. This fact can be explained as follows: in good (diffusive) conductors, an adequate description of electron transport may be achieved using electron wave packets extended over a distance of the order of the elastic mean free path l which is much longer than the electric field screening distance λ (the Debye or Thomas-Fermi length), so that all potential deviations from the local electroneutrality are compensated at distances well below l. This means that as far as charge transfer is concerned, the ensemble of conducting electrons can be described as a continuous fluid without voids. The electric charge Q transferred by the fluid is proportional to the shift x of the fluid as a whole with respect to the crystal lattice. The shift is *not* quantized, and hence neither is Q.

Though there seems to be a general consensus that an increase in conductor size leads to a crossover from discrete to continuous conduction, the location of the crossover has not been established. Experimentally, several earlier studies [8] have not given a definite answer to this question. Very recently, a convincing proof of (quasi)continuous conduction in very thin (3-nm) Cr films with a length of several micrometers at low (sub-1-Kelvin) temperatures was finally obtained [9]. The length dependence has not however, been studied in any detail.

Also, until very recently there was no reliable theoretical indication of the crossover. We believe that our recent analyses have provided theoretical solutions for this problem for diffusive conductors [10-12] and single-electron arrays [13]. The goal of this paper is to give a brief review of our work in this direction.

CHARGE TRANSFER DISCRETENESS AND SHOT NOISE

Firstly, we have analyzed [13] the general conditions under which the transport of charge through a conductor may be considered as (quasi)continuous, i.e., having the discreteness $\delta Q << e$. The definition of δQ can be most readily introduced in the interesting case of negligible thermal and quantum fluctuations:

$$k_BT << \max [eV_t, eV], \qquad G << e^2/h, \tag{2}$$

in which V_t is the possible Coulomb blockade threshold of the conductor and G its effective conductance. However, even in this most simple of cases, the definition depends essentially on the relation between the characteristic time scale τ of an experiment and the average current I through the system. In single-electronics, an adequate measure of current is the parameter

$$f_s = I/e. \tag{3}$$

(If a system exhibits SET oscillations [1], f_s is their frequency).

A. If $f_s \tau >> 1$, (i.e. either the time scale τ is large, or the dc current is high, or both), δQ may be defined as follows:

$$\delta Q = S_I(0)/2I. \tag{4}$$

If charge Q transfer through a system is a Poissonian series of jumps of fixed height δQ, Eq. (4) may be obtained strictly by repeating the well-known derivation of the Schottky formula (1). If the jump height is also random, Eq. (4) is still applicable as an estimate of the average jump height.

B. In the opposite limit, when τ is much shorter than the average spacing between the charge jumps (f_s^{-1}), we are essentially dealing with the Coulomb blockade regime. In this case an adequate definition of δQ is as follows:

$$\delta Q = C_{ef} V_t, \tag{5}$$

in which C_{ef} is the effective input capacitance of the conductor of interest. δQ given by this formula is the fraction of the initial electric charge of the system, which cannot relax due to the Coulomb blockade; e.g., for a single tunnel junction $\delta Q = e/2$ [1].

Since diffusive conductors do not exhibit the Coulomb blockade, the white noise is the decisive factor that determines the conduction type, and we have focused our attention on this property. Earlier theoretical studies (for their review see, e.g., Ref. 14) have indicated that for very short diffusive conductors, low-frequency shot noise should be close to the Schottky value (1). According to Nagaev [15], the shot noise should be suppressed only if the length L of a diffusive conductor becomes much the same as the electron-phonon scattering length $l_{e\text{-}ph}$. However, in these early works the effects of screening on fluctuations were not analyzed. Since the screening effects in good conductors are extremely strong (screening length λ is of the order of inter-atomic distance a), it was not clear whether those results would be valid for realistic samples with $L >> \lambda$.

THEORETICAL APPROACH

In order to understand the effect of screening on fluctuations in diffusive conductors, we have applied the Boltzmann-Langevin approach developed earlier by Kogan and Shul'man [16] to obtain a very simple and effective "drift-diffusion-Langevin" equation for the current density $\boldsymbol{j}(\boldsymbol{r}, t)$ in an arbitrary point:

$$\boldsymbol{j} = \sigma \boldsymbol{E} - D\nabla\rho + \boldsymbol{j}_s(\boldsymbol{r}, t). \tag{6}$$

Here $\boldsymbol{E}(\boldsymbol{r}, t)$ is a local electric field and $\rho(\boldsymbol{r}, t)$ is the local electric charge density ($\boldsymbol{E}$ and ρ are also related via the Poisson equation); σ and D are the local conductance and diffusion coefficient, respectively, while $\boldsymbol{j}_s(\boldsymbol{r}, t)$ is the effective density of fluctuation sources with the following correlator:

$$<\boldsymbol{j}_s(\boldsymbol{r}, t)\, \boldsymbol{j}_s(\boldsymbol{r}', t')> = S(\boldsymbol{r})\, \delta(\boldsymbol{r}-\boldsymbol{r}')\, \delta(t-t'), \tag{7a}$$

in which $S(\boldsymbol{r})$ is the local source intensity:

$$S(\boldsymbol{r}) = (2/3)\, e^2\, \tau(\boldsymbol{r})\, N(\boldsymbol{r})\, v_f^2(\boldsymbol{r}) \int_0^\infty f(\varepsilon, \boldsymbol{r})[1 - f(\varepsilon, \boldsymbol{r})]\, d\varepsilon. \tag{7b}$$

Here τ is the elastic scattering time and N is the density of states, both on the Fermi surface, v_f is the Fermi velocity, and $f(\varepsilon, \boldsymbol{r})$ is the electron distribution function. In equilibrium, Eqs. (7) may be reduced to the fluctuation-dissipation theorem, but these equations are also applicable to nonequilibrium situations (in which case the stationary distribution $f(\varepsilon, \boldsymbol{r})$ has to be found using appropriate methods of solid state theory). We have used this approach to find [10-12] the spectral density $S_I(\omega)$ of current fluctuations for diffusive conductors with various relations between the sample length L, effective screening length λ, electron-electron scattering length $l_{e\text{-}e}$, and electron-phonon scattering length $l_{e\text{-}ph}$, for two typical geometries (sandwich-type samples and thin conductors over the ground plane). Low-frequency noise has been found to be independent of the geometry.

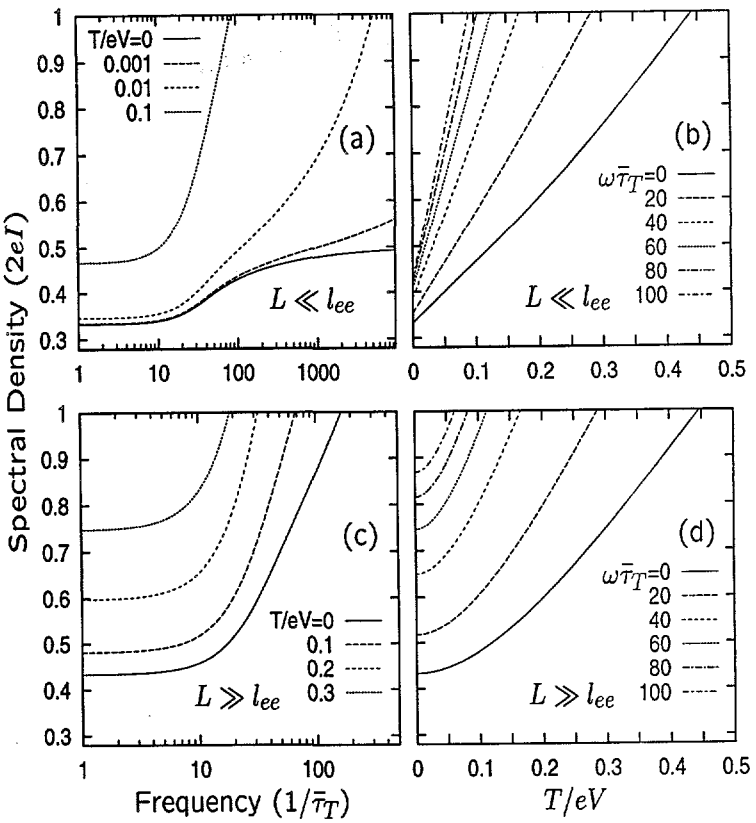

Figure 1. Frequency and temperature dependence of the spectral density of current fluctuations in the limits of weak (a,b) and strong (c,d) electron-electron scattering. (After Ref. 11).

BASIC RESULTS

In our first work [10] we have considered the effect of screening on the shot noise, neglecting for the time being the electron-electron and electron-phonon scattering (i.e. assuming $L \sim \lambda << l_{e\text{-}e}, l_{e\text{-}ph}$). Somewhat counter-intuitively, we have found that the low-frequency noise $S_I(0)$ does not depend on the L/λ ratio. Looking back, the reason for this insensitivity is the specific character of noise sources j_s: as evident from Eq. (7b), they result from elastic electron scattering, i.e. random, sudden changes of electron momentum without any immediate change of electric charge density, and thus do not explicitly produce screenable charge imbalance (though such imbalance eventually arises because of the finite sample length). This sort of perturbation is not directly affected by screening strength.

This is why we have switched our attention to inelastic electron scattering. Figure 1 shows that in the case of negligible electron-phonon scattering ($L \sim l_{e\text{-}e} << l_{e\text{-}ph}$), electron-electron scattering provides for only quantitative change in shot noise which generally remains close to the Schottky value [11]. However, when L becomes larger than the electron-phonon scattering length $l_{e\text{-}ph}$, the situation changes substantially: at $\beta \equiv L/l_{e\text{-}ph} >>1$, the shot noise intensity goes down as $\beta^{-2/5}$, for any relation between L and $l_{e\text{-}e}$ (Fig. 2).

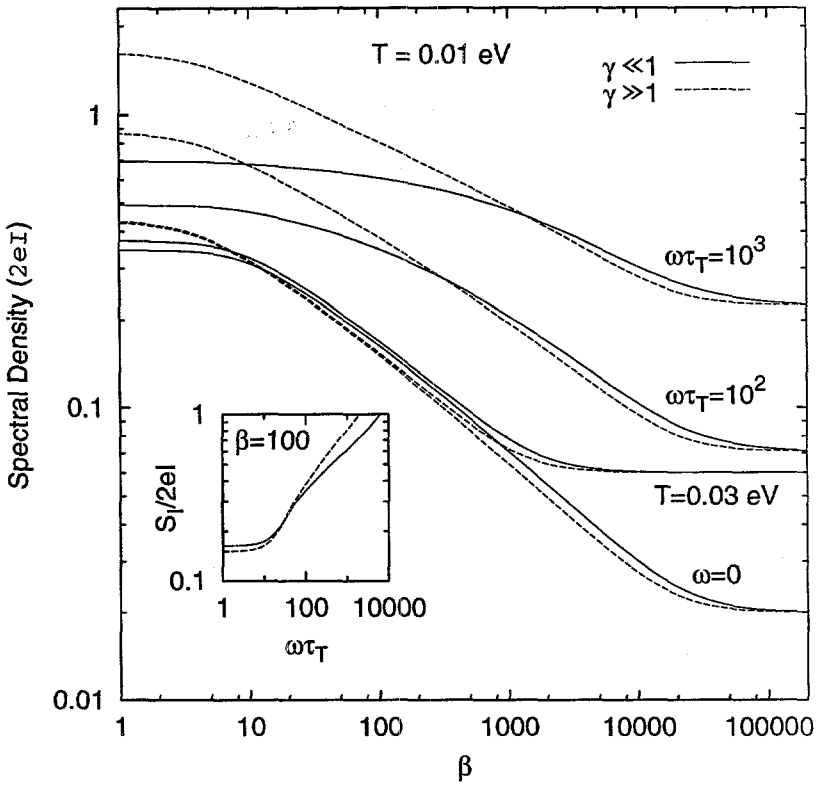

Figure 2. Spectral density of current fluctuations as a function of at $\beta \equiv L/l_{e\text{-}ph}$ for the cases $L/l_{e\text{-}e} << 1$ (solid lines) and $L/l_{e\text{-}e} >>1$ and several frequencies. Inset shows the noise density as a function of frequency for $\beta = 100$. (After Ref. 12.)

As an afterthought, these results have a simple physical explanation: the usual shot noise described by Eq. (1) may be considered qualitatively as a result of "overheating" of the electron subsystem to the effective temperature $T_e \sim eV/2k_B$ with the applied electric field, since $eV/2$ is the average energy of the electron inside the conductor. Electron-electron interaction (both screening and e-e scattering) cannot drain this extra energy from the system, while inelastic electron-phonon scattering passes the extra energy from electrons to the crystal lattice and hence cools down the electrons and reduces the shot noise.

DISCUSSION

To summarize, we have obtained a convincing theoretical proof that in order to have the shot noise suppressed much below its Schottky value and hence to implement the effectively continuous

electron transfer in a diffusive conductor, its length L should be much longer than the electron-phonon screening length $l_{e\text{-}ph}$. Our group has also taken the first steps towards the experimental confirmation of this theoretical prediction. A special low-noise electronic setup has been developed to measure white noise, with a sensitivity which allows such measurements to be made even at low temperatures. In order to test it, the white noise of a resonant tunneling diode (RTD) has been measured [17] as a function of tunneling current at temperature 4.2 K. As predicted by theory [14], as the current increases the shot noise is reduced to one half of the Schottky value (1). Our plans are to use this setup for the measurement of shot noise in diffusive nanostructures.

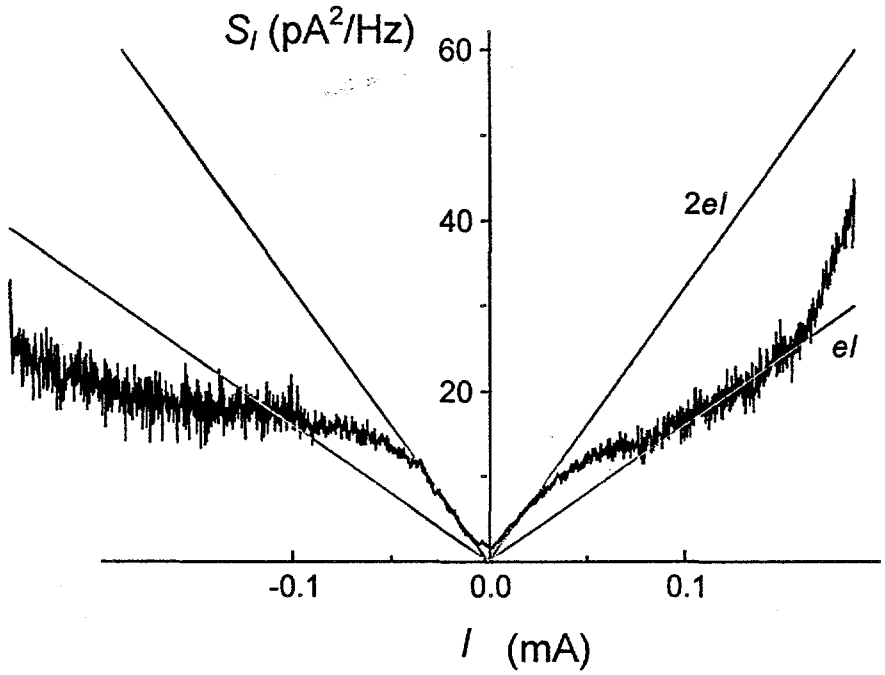

Figure 3. Shot noise in resonant tunneling diode (black curve) as a function of dc current. The straight lines correspond to the full Schottky value and its 50% suppression.

Another direction of our future work will be the analysis of the crossover between quasi-continuous and discrete electron transfer in systems with hopping conduction. In fact, in order to be used in resistive single-electron devices the impedance $Z(\omega)$ of a conductor must be very high,

$$\mathrm{Re}\, Z^{-1}(\omega) << G << e^2/\hbar, \tag{8}$$

at all frequencies ω up to $\sim e^2/\hbar C$ [1]. In practice, condition (8) requires the dc resistance $R = Z(0)$ to be of the order of a few MΩ or higher. Simultaneously, the linear size of the conductor should be small, so that its stray capacitance C remains low,

$$C << e^2/k_B T. \tag{9}$$

For typical present-day low-temperature experiments, C may be up to 10^{-15} F, so that the length L of the conductor may be as large as a few micrometers. Here there is hope of satisfying conditions (8) and (9) with diffusive thin film conductors [9]. For prospective room-temperature applications, however, condition (9) requires the conductor size to be much smaller (one nanometer or less). Since the electron-

phonon scattering length is rather long on this scale (e.g., >10 nm in silicon at typical doping levels), there is little hope of satisfying the charge quasi-continuity condition $l_{e\text{-}ph} \ll L$ in nanometer-scale diffusive conductors.

On the other hand, at hopping conduction (see, e.g., Ref. 18), an electron loses a considerable part of its energy with every jump, i.e. the average hopping distance $\langle r \rangle$ plays a role similar to $l_{e\text{-}ph}$ at diffusive conduction. Since in typical hopping materials $\langle r \rangle$ is of the order of one nanometer, these is hope that conductors with L of the order of a few nanometers will exhibit substantial suppression of the Schottky noise.

We have carried out a preliminary study [13] of this problem using a very crude model of a hopping conductor, a 1D array of small tunnel junctions. Numerical calculations of $S_I(0)$ have been carried out using the Monte-Carlo Single Electron Simulator (MOSES) which had been developed in our group [19]. The calculations have shown that the shot noise may be suppressed by a factor of $1/N$, where N is the number of tunnel junctions in the array. However, very close to the Coulomb blockade threshold there is no suppression, i.e. the noise is *always* described by Eq. (1). Moreover, in uniform arrays with zero background charge the Coulomb blockade is rather substantial, so that Eq. (5) gives the charge discreteness $\delta Q \sim e$.

We hope that in hopping conductors (as well as in 2 and 3D tunnel junction arrays with random parameters), due to the rich statistics of the localized states, the Coulomb blockade threshold may be averaged out effectively. As a result, both conditions of the (quasi) continuous charge transfer may be satisfied virtually everywhere. If our analysis shows this to be true at least in some cases, we will start looking for practical systems satisfying these conditions, and hence providing sub-single-electron charge transfer at room temperatures.

If our search is successful, it may have important implications for the development of single-electron digital circuits.

ACKNOWLEDGMENTS

The theoretical work at Stony Brook described in this review was carried out in collaboration with D. Averin, K. Matsuoka, and Y. Naveh. A parallel experimental effort is being carried out by V. Kuznetsov, E. Mendez, J. Bruno, and J.T. Pham. The work is supported by OER under grant # DE-FG02-95ER14575.

REFERENCES

1. K.K. LIKHAREV, *IBM J. Res. Devel.* 32, 144 (1988); D.V. AVERIN and K.K. LIKHAREV, in: *Mesoscopic Phenomena in Solids*, ed. by B. Altshuler *et al.*, Elsevier, Amsterdam (1991), p. 173; *Single Charge Tunneling*, ed. by H. Grabert and M.H. Devoret, Plenum, New York (1992).

2. L.P. KOUWENHOVEN, C.M. MARKUS, P.L. MCEUEN, S. TARUCHA, R.M. WESTERVELT, N.S. WINGREEN, in: *Mesoscopic Electron Transfer*, ed. by L. Sohn *et al.*, Kluwer, Dordrecht (1997), p. 105.

3. K.K. LIKHAREV, "Single Electron Devices and Their Applications", to be published in *Proc. IEEE* (January 1998).

4. K. LIKHAREV, *IEEE Trans. on Magn.* 23, 1142 (1987); A.N. KOROTKOV, "Theoretical Analysis of the Resistively-Coupled Single-Electron Transistor", LANL e-Archive #cond-mat/9803038 (1998).

5. R. KIEHL and T. OHSHIMA, *Appl. Phys. Lett.* 67, 2494 (1995); T. OHSHIMA and R. KIEHL, *J. Appl. Phys.* 80, 912 (1996); T. OHSHIMA, *Appl. Phys. Lett.* 69, 4059 (1996).

6. T. CLAESON and K.K. LIKHAREV, *Sci. Amer.* 266, 80 (1992).

7. D. ROGOVIN and D.J. SCALAPINO, *Ann. Phys.* 86, 1 (1974).

8. A.N. CLELAND, J.M. SCHMIDT, and J. CLARKE, *Phys. Rev. B* 45, 2950 (1992); D. POPOVIC, C.J.B. FORD, J.M. HONG, and A.B. FOWLER, *Phys. Rev. B* 48, 12349 (1993); L.S. KUZMIN and YU.A. PASHKIN, *Physica B* 194-196, 1713 (1994); T. HOLST, D. ESTEVE, C. URBINA, and M.H. DEVORET, *Phys. Rev. Lett.* 77, 3889 (1996); P. Joyes, D. Esteve, and M.H. Devoret, *Phys. Rev. Lett.* 80, 1956 (1998).

9. W. ZHENG, J.R. FRIEDMAN, D.V. AVERIN, S. HAN, and J.E. LUKENS, "Observation of Strong Coulomb Blockade in Resistively Isolated Tunnel Junctions", preprint (1998).

10. Y. NAVEH, D.V. AVERIN, and K.K. LIKHAREV, *Phys. Rev. Lett.* 79, 3482 (1997). [Later, some of the results were published by K.A. NAGAEV, *Phys. Rev. B* 57, 4628 (1998).]

11. Y. NAVEH, D.V. AVERIN and K.K. LIKHAREV, "Noise Properties and AC Conductance of Mesoscopic Diffusive Conductors with Screening", LANL e-Print Archive #cond-mat/9801188; submitted to *Phys. Rev. B* (1998).

12. Y. NAVEH, D.V. AVERIN, and K.K. LIKHAREV, "Shot Noise in Diffusive Conductors: A Quantitative Analysis of Electron-Phonon Interaction Effects", LANL e-Print Archive #cond-mat/9803335; submitted to *Phys. Rev. B* (1998).

13. K.A. MATSUOKA and K.K. LIKHAREV, "Shot Noise of Single-Electron Tunneling in 1D Arrays", LANL e-Print Archive #cond-mat/9801219; to be published in *Phys. Rev. B* 57 (June 15, 1998).

14. M.J.M. DE JONG and C.W.J. BEENAKKER, in: *Mesoscopic Electron Transport*, ed. by L.L. Sohn *et al.*, Kluwer Academic Publishers, Dordrecht (1997), p. 225.

15. K.E. NAGAEV, *Phys. Lett. A* 169, 103 (1992); *Phys. Rev. B* 32, 4740 (1995).

16. SH.M. KOGAN and A.YA. SHUL'MAN, *Sov. Phys. - JETP* 29, 467 (1969).

17. V. KUZNETSOV, E.E. MENDEZ, J. BRUNO, and J.T. PHAM, "Shot Noise Enhancement in Resonant Tunneling Structures under a Magnetic Field", submitted to *Phys. Rev.* (1998).

18. N.F. MOTT and J.H. DAVIES, *Electronic Properties of Non-Crystalline Materials*, 2nd ed., Oxford Univ. Press, Oxford (1979); N.F. MOTT, *Conduction in Non-Crystalline Materials*, 2nd ed., Clarendon Press, Oxford (1993); B.I. SHKLOVSKII and A.L. EFROS, *Electronic Properties of Doped Semiconductors*, Springer, Berlin (1984); *Hopping Transport in Solids*, ed. by M. Pollak and B. Shklovskii, Elsevier, Amsterdam (1991); *Electron-Electron Interactions in Disordered Systems*, ed. by A.L. Efros and M. Pollak, Elsevier, Amsterdam (1985).

19. MOSES 1.1 (in both MS-DOS and UNIX versions) is available for anonymous ftp from hana.physics.sunysb/pub/moses.

VORTEX LINE FLUCTUATIONS IN HIGH TEMPERATURE SUPERCONDUCTORS

S. Teitel

Department of Physics and Astronomy
University of Rochester, Rochester, New York 14627

Peter Olsson

Department of Theoretical Physics
Umeå University, 901 87 Umeå, Sweden

ABSTRACT

We carry out large scale numerical simulations of the anisotropic uniformly frustrated 3D XY model, as a model for vortex line fluctuations in high T_c superconductors in an applied magnetic field. Considering different values of applied magnetic field and system anisotropy, we find that in all cases there is a single phase transition associated with the vortex line lattice melting. We carry out the first systematic analysis of the superconducting correlation length parallel to the applied field in the vortex line liquid phase. We find our results to collapse onto a universal curve as the temperature decreases towards the melting transition, allowing us to make a realistic prediction for the size of this correlation length in real high T_c materials.

INTRODUCTION

In the presence of an applied magnetic field $H_{c1}(T) < H < H_{c2}(T)$, the low temperature state of a clean type II superconductor is the Abrikosov vortex line lattice [1], consisting of a triangular lattice of perfectly straight lines of vorticity in the phase angle of the complex superconducting wavefunction ψ. The lines are parallel to the magnetic field, with a density given by B/ϕ_0; B is the magnetic field that penetrates the sample ($B < H$), and $\phi_0 = hc/2e$ is the flux quantum. In high critical temperature superconductors, the combination of the higher temperatures and the anisotropy of the weakly coupled CuO layers results in greatly enhanced thermal fluctuations. Several theoretical models [2,3] have therefore led to the prediction that upon heating the vortex line lattice should melt into a a vortex line liquid. Experimentally [4], the observation of a sharp discontinuous vanishing of resistivity,

coinciding with a sharp discontinuous jump in equilibrium magnetization, has been cited as evidence for a first order equilibrium phase transition in both YBCO and BSCCO. In YBCO, this transition has further been found to coincide with a sharp singularity in the specific heat [5].

The association of this experimentally observed transition with the vortex lattice melting has been generally, but not universally [6], accepted. The melting of the vortex lattice at T_m, with the onset of vortex line diffusion, leads to the onset of finite linear resistivity in the direction perpendicular to the applied magnetic field. However some theoretical arguments [7] have predicted that superconducting coherence parallel to the applied field could persist above melting, and vanish only at a higher transition T_c. Some experimental evidence for this scenario has been found in "flux transformer" experiments [8], and in experiments with a controlled amount of columnar defects [9]. Other "flux transformer" experiments [10] find only a single transition, but suggest that the correlation length parallel to the applied magnetic field, just above melting, can still be of the surprising large micron scale.

MODEL

The system of many strongly interacting vortex lines is a complex many body statistical system. Analytic methods can only be applied to rather simplified models. In order to help establish the true structure of the phase diagram and the possible thermodynamic states, we have introduced [11,12] the use of large scale Monte Carlo simulations of the "uniformly frustrated" three dimensional XY model, as a model for a fluctuating superconductor. Starting with the Ginzburg-Landau free energy functional for a fluctuating superconducting and making the London approximation that the amplitude of the superconducting wavefunction is constant outside of a vortex core, $\psi(\mathbf{r}) = |\psi| e^{i\theta(\mathbf{r})}$, taking the magnetic field to be uniform throughout the sample, and discretizing the continuum to a cubic mesh of points, one arrives at the Hamiltonian for the 3D XY model [12],

$$\mathcal{H}[\theta_i] = -\sum_{\langle ij \rangle} J_{ij} \cos(\theta_i - \theta_j - A_{ij}) \ . \tag{1}$$

Here θ_i is the phase angle of the wavefunction at site i of the cubic mesh, the sum is over nearest neighbor bonds, $A_{ij} = (2\pi/\phi_0) \int_i^j \mathbf{A} \cdot d\mathbf{l}$ is the integral of the magnetic vector potential across the bond, and $J_{ij} = J_z$ or $J_\perp$ is the anisotropic coupling in the direction of the bond. If we identify the discrete spacing along $\hat{\mathbf{z}}$ as the distance d between copper-oxide planes, and the discrete spacing in the xy plane as representing the short length cutoff for a vortex core of radius ξ_0, we have [13]

$$J_\perp \equiv \frac{\phi_0^2 d}{16\pi^3 \lambda_\perp^2} \ , \qquad J_z = \frac{\phi_0^2 \xi_0^2}{16\pi^3 \lambda_z^2 d} \ , \tag{2}$$

where $\lambda_\perp$ and λ_z are the magnetic penetration lengths within and normal to the copper-oxide planes, respectively. The anisotropy in couplings is then

$$\frac{J_z}{J_\perp} = \left(\frac{\lambda_\perp}{\lambda_z}\frac{\xi_0}{d}\right)^2 \quad . \tag{3}$$

The density of vortex lines per unit cell of the numerical mesh is given by the parameter

$$f \equiv \frac{\xi_0^2 B}{\phi_0} = \left(\frac{\xi_0}{a_v}\right)^2 \tag{4}$$

where a_v is the average spacing between vortex lines.

In our model of Eq.(1) we ignore spatial variations and fluctuations in the internal magnetic field, taking $\nabla \times \mathbf{A} = B\hat{\mathbf{z}}$ a uniform constant. This should be valid provided [12] that B is so large that the spacing between vortex lines $a_v \ll \lambda_\perp$ (so the magnetic fields associated with each vortex line strongly overlap), yet B is small enough that $a_v \gg \xi_0$ (so details of the vortex cores are not important). The anisotropy must also be such that $d < \lambda_\perp^2/\lambda_z$, so that Josephson coupling between the planes dominates over magnetic coupling [3]. We consider here only the case where the applied magnetic field is oriented along the anisotropy direction $\hat{\mathbf{z}}$.

Despite the considerable effort of different workers [15] numerically simulating the Hamiltonian (1), the very slow process associated with vortex line cutting has made it exceedingly difficult to equilibrate the simulations and obtain the true equilibrium states of the system. Early simulations [12,13] suggested two distinct transitions, $T_m < T_c$, with an intermediate superconducting vortex line liquid state. Very recently however, Hu *et al.* [16], carrying out very long simulations on large systems with parameter values $f = 1/25$ and $J_z/J_\perp = 1/10$, found clear evidence for only a single first order vortex lattice transition with $T_m = T_c$. These results have been confirmed in independent simulations by Koshelev and by Nguyen and Sudbø [17]. Ryu and Stroud [18] however have argued that these results hold only for values of $J_z/J_\perp \ll 1$. In their simulations of an isotropic system, $J_z/J_\perp = 1$, they continue to suggest two transitions.

In order to clarify this situation, we have carried out new simulations of the Hamiltonian (1) for several different values of $J_z/J_\perp$ and f, including the isotropic case. Our results show clearly that in all cases there is only a single transition, associated with the vortex line lattice melting, in agreement with Hu *et al.* In these simulations, we have also carried out the first systematic calculation of the phase correlation length parallel to the applied field, in order to establish the extent of longitudinal superconducting coherence in the vortex line liquid.

RESULTS

To establish the phase transitions in the system we compute three main quantities [13]: the helicity moduli parallel and perpendicular to the the applied magnetic field, Υ_z and $\Upsilon_\perp$, and the vortex-vortex correlation function $S(\mathbf{k}_\perp)$, where $\mathbf{k}_\perp$ is a wavevector in the plane transverse to the applied magnetic field. Υ_z and $\Upsilon_\perp$ measure the density of superconducting

electrons; their vanishing indicates the loss of superconducting coherence in the respective direction. For an ordered vortex lattice, $S(\mathbf{k}_\perp)$ will have sharp Bragg peaks at the reciprocal lattice vectors $\mathbf{k}_\perp = \mathbf{K}$; the vanishing of these peaks indicates the melting transition. Since $S(\mathbf{K})$ is finite even the liquid, due to the presence of a smooth non-singular background, we take as our vortex lattice ordering parameter $DS(\mathbf{K}) \equiv S(\mathbf{K}) - S(\mathrm{R}_x[\mathbf{K}])$, where $\mathrm{R}_x[\mathbf{K}]$ is $\mathbf{K}$ reflected through the x axis. Since the vortex liquid is symmetric under such a reflection, while the vortex lattice is not, we have $DS(\mathbf{K}) > 0$ in the lattice, while $DS(\mathbf{K}) = 0$ in the liquid.

In Fig. 1 below, we plot our results for Υ_z, $\Upsilon_\perp$, and $DS(\mathbf{K})$ for the specific isotropic case of $J_z/J_\perp = 1$, $f = 1/20$, for systems of size $L_\perp = 40$ and $L_z = 32$, 64, 128. Our runs are for typically $2 \times 10^6 - 10^7$ Monte Carlo passes per mesh site. We see that there is a very substantial finite size effect as L_z is varied. Only for the largest value $L_z = 128$ does it become clear that $DS(\mathbf{K})$ and Υ_z vanish at the same temperature $T_m \simeq 1.4J$; the vortex lattice melts at exactly the same temperature that longitudinal superconducting coherence is lost. The sharp discontinuous drop in Υ_z and $DS(\mathbf{K})$ at T_m indicates that the transition is first order. A similar conclusion is arrived at by consideration of energy histograms exactly at T_m, which show the system to be switching back and forth between two distinct states of different energy. Note that $\Upsilon_\perp$ is seen to vanish at a temperature considerably below T_m. This represents the unpinning of our vortex lattice from the numerical mesh that approximates the continuum; a vortex lattice in a smooth continuum is free to slide transverse to the applied magnetic field, and this sliding motion in principle gives rise to flux flow resistance (random pinning sites in real experimental samples are believed to pin the vortex lattice and remove this sliding motion as a source of resistivity). Our observation that $\Upsilon_\perp = 0$ for a considerable temperature range below T_m indicates that our numerical discretization is not significantly effecting behavior at the vortex lattice melting.

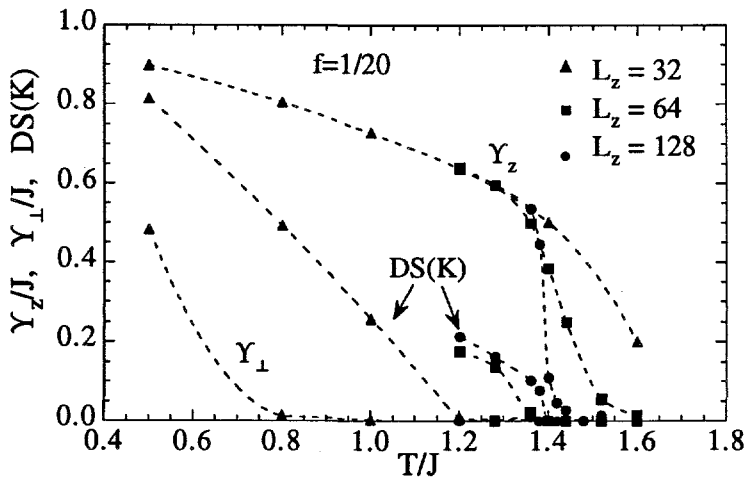

FIG. 1. Helicity moduli $\Upsilon_\perp$ and Υ_z, and vortex lattice order parameter $DS(\mathbf{K})$, versus temperature T for vortex line density $f = 1/20$ and isotropic couplings ($J \equiv J_z = J_\perp$), for system sizes $L_\perp = 40$, $L_z = 32, 64, 128$. Vortex lattice melting coincides with the loss of longitudinal superconductivity at $T_m/J \simeq 1.4$.

In a similar fashion we have considered, and determined the value of T_m, for the cases $f = 1/20$ with $J_z/J_\perp = 1/9$ and $1/40$, and for $f = 1/12$ with $J_z/J_\perp = 1/9$. In all cases we found only a single transition associated with the vortex lattice melting.

To investigate the length scale over which longitudinal superconducting correlations persist into the vortex line liquid, we consider now the phase angle correlation function

$$C(z) \equiv \frac{1}{L_\perp^2}\sum_{\mathbf{r}_\perp}\langle\psi^*(\mathbf{r}_\perp,z)\psi(\mathbf{r}_\perp,0)\rangle = \frac{1}{L_\perp^2}\sum_{\mathbf{r}_\perp}\langle e^{-i[\theta(\mathbf{r}_\perp,z)-\theta(\mathbf{r}_\perp,0)]}\rangle \sim e^{-z/\xi_z} \tag{5}$$

where the exponential decay, expected only for the vortex line liquid phase $T > T_m$, determines the correlation length ξ_z.

In Fig. 2 we plot an example of $C(z)$ vs. z for the specific case of $f = 1/20$, $J_z/J_\perp = 1/9$, and $T = .056 > T_m$. The straight line on the semi-log plot shows a good agreement with the expected exponential decay. Fitting $C(z)$ to an exponential, self consistently using data restricted to the range $\xi_z < z < L_z/3$, we determine $\xi_z(T)$ in the vortex line liquid phase, for the different parameter values we have considered. The resulting data is shown in Fig. 3.

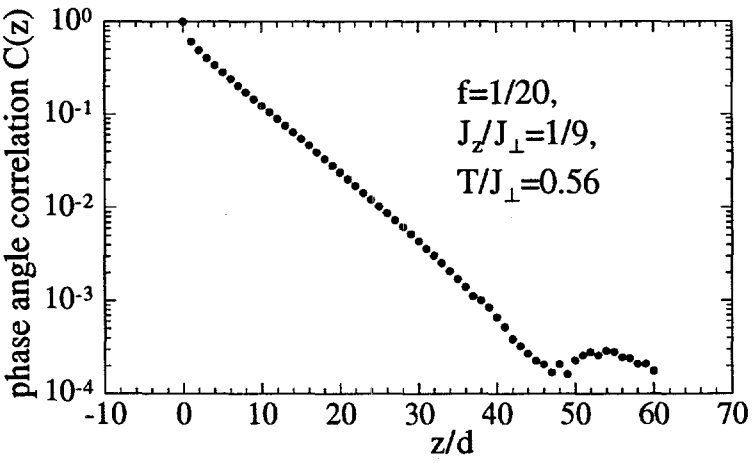

FIG. 2. Phase angle correlation function $C(z)$ vs. z for a particular $T > T_m$. A fit to an exponential decay determines the correlation length ξ_z.

We now show that the data of Fig. 3 can be collapsed onto a universal curve, as T approaches T_m. Measured in units of the interplanar spacing, the dimensionless ξ_z/d should depend only on the other dimensionless parameters $J_z/J_\perp$ and f. For small magnetic fields with $a_v \gg \xi_0$, we expect that ξ_z should not depend on the vortex core size ξ_0 [19]. The only combination of $J_z/J_\perp$ and f that is independent of ξ_0 is $f(J_\perp/J_z)$. If we further expect that ξ_z/d should remain proportional to $1/d$, we conclude that $\xi_z/d \sim 1/\sqrt{f(J_\perp/J_z)}$. In Fig. 4 we replot the data of Fig. 3 as $\sqrt{f(J_\perp/J_z)}$ (ξ_z/d) vs. T/T_m. We see that as $T \to T_m$, all the data collapses nicely to a single curve. Only at higher temperatures, where ξ_z/d can decrease no further than unity due to the intrinsic discreteness of the system, do the curves separate.

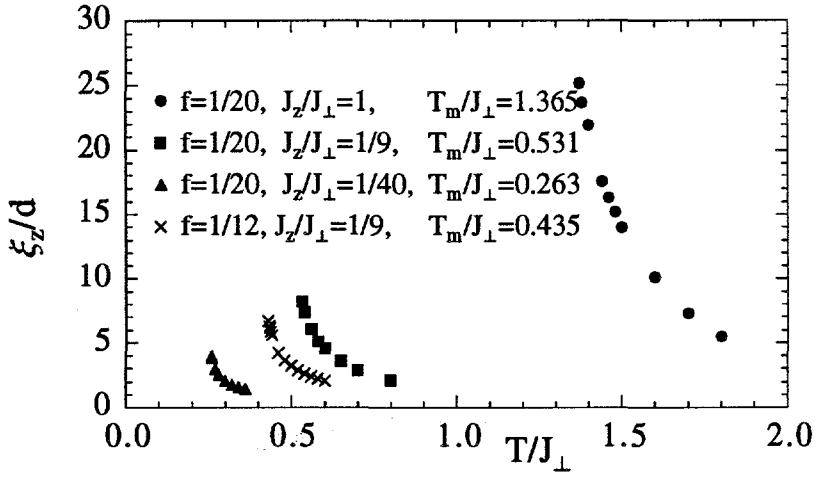

FIG. 3. Correlation lengths $\xi_z(T)$ vs. T in the vortex line liquid phase, for various values of vortex line density f and anisotropy $J_z/J_\perp$.

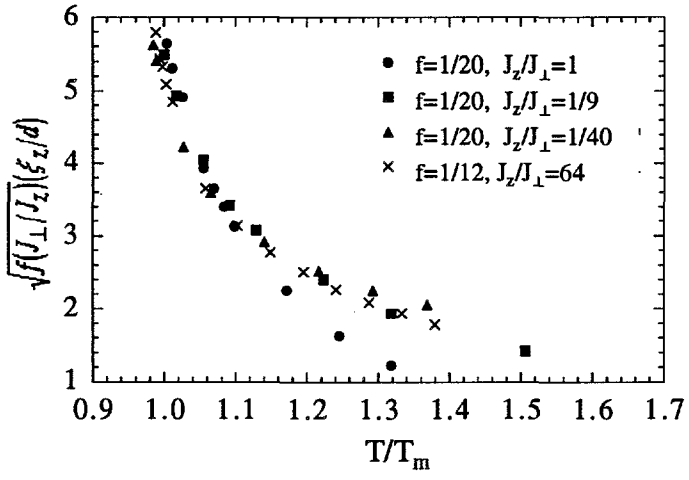

FIG. 4. Data of Fig. 3 rescaled and plotted as $\sqrt{f(J_\perp/J_z)}\ (\xi_z(T)/d)$ vs. T/T_m. The data collapses onto a universal curve as T approaches T_m.

From Fig. 4, and using Eqs.(3) and (4), we conclude that the longitudinal phase coherence correlation length in the vortex line liquid, just above the melting T_m, is given by

$$\xi_z(T_m) \simeq 6\sqrt{\frac{J_z}{fJ_\perp}}d = 6\left(\frac{\lambda_\perp}{\lambda_z}\right)a_v \ . \tag{6}$$

Note that our result is independent of the vortex core size ξ_0, and the interplanar spacing d, indicating that for the parameters considered, our numerical mesh is playing no significant role in the vortex lattice melting, and that the melting is behaving as in a smooth continuum. Once the parameters are varied such that ξ_z, as given by Eq.(6) above, would fall below the

length d (which represents the physical spacing of the CuO planes), we expect to enter a new regime of "quasi-two dimensional" behavior.

Our result in Eq.(6) is in qualitative agreement with recent simulations carried out by Nordborg and Blatter [20], who used the greatly simplified "two dimensional boson" approximation, in which vortex lines interact only through segments which are at equal heights. Measuring vortex rather than phase angle correlations, they found $\xi_z \simeq 1.7(\lambda_\perp/\lambda_z)a_v$. The main conclusion of our own simulations is therefore to show that the more realistic vortex line interactions contained in our 3D XY model increases the correlation length by a factor of approximately 3.5.

We can now apply Eq.(6) to YBCO, for which the continuum limit is appropriate. Using the values $\lambda_\perp/\lambda_z \simeq 1/7$, we find for a magnetic field of $B \simeq H = 4T$ with $a_v = 0.45\ \mu m$, the result $\xi_z(T_m) \simeq 0.038\ \mu m$. This result is well below the micron size length scale suggested by the flux transformer experiments. It remains to be seen whether the explanation of the flux transformer experiments lie in either a dynamic, rather than an equilibrium, effect, or in the highly non-uniform nature of the experimental geometry.

ACKNOWLEDGMENT

This work has been supported by the U.S. Department of Energy under grant DE-FG02-89ER14017, by the Swedish Natural Science Research Council Contract No. E-EG 10376-305, and by the resources of the Swedish High Performance Computing Center North (HPC2N).

REFERENCES

[1] M. Tinkham, *Introduction to Superconductivity*, (R.E. Krieger Co., Malabar, FL, 1980).

[2] D. R. Nelson and H. S. Seung, Phys. Rev. B **39**, 9153 (1989); A. Houghton, R. A. Pelcovits and A. Sudbø, Phys. Rev. B **40**, 6763 (1989); E. H. Brandt, Phys. Rev. Lett. **63**, 1106 (1989); L. I. Glazman and A. E. Koshelev, Phys. Rev. B **43**, 2835 (1991).

[3] D. S. Fisher, M. P. A. Fisher, and D. A. Huse, Phys. Rev. B **43**, 130 (1991); L. I. Glazman and A. E. Koshelev, Phys. Rev. B **43**, 2835 (1991).

[4] U. Welp, J. A. Fendrich, W. K. Kwok, G. W. Crabtree, and B. W. Veal, Phys. Rev. Lett. **76**, 4809 (1996); D. T. Fuchs, E. Zeldov, D. Majer, T. Tamegai, S. Ooi, and M. Konczykowski, Phys. Rev. B **54**, R796 (1996).

[5] A.Schilling, R. A. Fisher, N. E. Phillips, U. Welp, W. K. Kwok, and G. W. Crabtree, Phys. Rev. Lett. **78**, 4833 (1997).

[6] M. A. Moore, Phys. Rev. B **55**, 14136 (1997); A. K. Kienappel and M. A. Moore, preprint cond-mat/9804314

[7] M. V. Feigelman, V. B. Geshkenbein, L. B. Ioffe, and A. I. Larkin, Phys. Rev. B **48**, 16641 (1993); Z. Tešanović, Phys. Rev. B **51**, 16204 (1995).

[8] H. Safar, P. L. Gammel, D. A. Huse, S. N. Majumdar, L. F. Schneemeyer, D. J. Bishop, D. López, G. Nieva and F. de la Cruz, Phys. Rev. Lett. **72**, 1272 (1994); F. de la Cruz, D. López and G. Nieva, Philos. Mag. B **70**, 773 (1994).

[9] A. V. Samoilov, M. V. Feigelman, M. Konczykowski and F. Holtzberg, Phys. Rev. Lett. **76**, 2798 (1996).

[10] D. López, E. F. Righi, G. Nieva and F. de la Cruz, Phys. Rev. Lett. **76**, 4034 (1996).

[11] Y.-H. Li and S. Teitel, Phys. Rev. Lett. **66**, 3301 (1991).

[12] Y.-H. Li and S. Teitel, Phys. Rev. B **47**, 359 (1993) and *ibid.* **49**, 4136 (1994).

[13] T. Chen and S. Teitel, Phys. Rev. B **55**, 11766 (1997).

[14] D. S. Fisher in *Phenomenology and Applications of High Temperature Superconductors*, edited by K. Bedell *et al.* (Addison-Wesley, Reading, MA, 1992), p.287.

[15] R. E. Hetzel, A. Sudbø and D. A. Huse, Phys. Rev. Lett. **69**, 518 (1992); D. Domínguez, N. Grønbech-Jensen and A. R. Bishop, Phys. Rev. Lett. **75**, 4670 (1995); E. A. Jagla and C. A. Balseiro, Phys. Rev. Lett. **77**, 1588 (1996); A. K. Nguyen, A. Sudbø and R. E. Hetzel, Phys. Rev. Lett. **77**, 1592 (1996); T. J. Hagenaars, R. E. Hetzel, W. Hanke, M. Leghissa and G. Saemann-Ischenko, Phys. Rev. B **55**, 11706 (1997); S. Ryu and D. Stroud, Phys. Rev. Lett. **78**, 4629 (1997); A. K. Nguyen and A. Sudbø, Phys. Rev. B **57** 3123 (1998).

[16] X. Hu, S. Miyashita and M. Tachiki, Phys. Rev. Lett. **79**, 3498 (1997).

[17] A. E. Koshelev, Phys. Rev. B **56**, 11201 (1997); A. K. Nguyen and A. Sudbø, preprint cond-mat/9712264.

[18] S. Ryu and D. Stroud, to appear Phys. Rev. B1, 01 June 1998.

[19] The interactions between different vortex lines are independent of the core size ξ_0. However the self interaction of a bending vortex line can depend on ξ_0. This may lead to weak logarithmic dependencies on ξ_0. See E. H. Brandt, J. Low Temp. Phys. **26**, 735 (1977).

[20] H. Nordborg and G. Blatter, Phys. Rev. Lett. **79**, 1925 (1997).

FAST THERMAL TRANSPORT AND PHASE-CHANGE

Dongsik Kim, Mengqi Ye, Cynthia M. Hipwell,
Leslie M. Phinney, Jennifer Lukes, Jian-Gang Weng,
Costas P. Grigoropoulos, and Chang-Lin Tien

Department of Mechanical Engineering
University of California,
Berkeley, CA 94720

ABSTRACT

The coupling of the laser energy into the liquid, the heating and the ensuing phase change transformations generate energy and momentum transfer phenomena of fundamental scientific interest. The pulsed-laser-induced ablation of strongly absorbing liquids and the generation of acoustic transients are studied in the present work. Research has also been conducted to understand the rapid phase-change mechanism and the dynamics of microbubble growth when a nanosecond duration laser pulse irradiates a highly absorbing solid surface contacting a transparent liquid. Porous silicon exhibits unique characteristics, such as quantum confinement, a high-surface-to-volume ratio and structural disorder, which lead to enhanced optical properties. The thermal and radiative transport in porous silicon was modeled theoretically and probed experimentally by a dual-probe technique of picosecond temporal resolution. A novel approach utilizing ultra-short (femtosecond and picosecond) laser radiation has been proposed to overcome stiction problems that cause catastrophic failure in micro-electro-mechanical systems (MEMS). The method is based on the release of the trapped residual moisture via electronic desorption excited by the ultra-short laser pulse.

PULSED LASER-INDUCED ABLATION OF ABSORBING LIQUIDS

The interaction of short laser pulse with liquid matter has been a subject of interest owing to the important scientific issues raised, such as the study of thermophysics of rapid-phase transition and material-ablation mechanisms, as well as to its extensive practical applications. A number of investigations have examined the mechanisms of pulsed laser induced ablation of absorbing liquids in connection with a variety of biomedical application [1,2,3]. When a liquid medium is irradiated by a laser pulse, acoustic transients are generated either by a purely thermoelastic mechanism or by the combined effect with other nonlinear processes such as liquid evaporation, dielectric breakdown, and electrostriction [4,5,6]. The acoustic excitation by such processes bear significant effect upon the ablation mechanism. The optically enhanced acoustic field can also be utilized in several applications, including photoacoustic spectroscopy, nondestructive testing of materials [7], and liquid assisted laser cleaning [8,9].

Nanosecond Excimer Laser Ablation of Aqueous Solutions

A KrF excimer laser (λ=248 nm, FWHM=24 ns) was used for the ablation of aqueous solutions of K_2CrO_4 [10]. K_2CrO_4 was selected as a dye to adjust the absorption coefficient of the aqueous solutions because of its chemical stability and lack of fluorescence. A laser-flash photography technique has been employed to acquire image sequence with nanosecond time resolution, Figure 1(a) shows the ablation process in the liquid (top panel) and into the ambient air (bottom panel). In the liquid, a cavity starts forming after the end of the pulse with simultaneous release of a shock wave into the ambient air. At longer times, a pressure wave is observed in the liquid, leaving in its wake cavitation bubbles. The ejected plume and a second discontinuity develop behind the leading shock front. At t =1 μs, the shadowgraphs show a deep cavity and large scale hydrodynamic motion of the liquid. The ablation process has been modeled numerically, by solving the heat transfer in the liquid and the compressible gas dynamics in the ejected plume. The computational approach described in [11] was used for the latter. At moderate laser fluences for which the vaporization is explosive, the kinetic relation for the vapor flux was applied at the liquid/vapor interface. At higher fluences, the front temperature was fixed at the spinodal limit of superheat (~ 0.84 T_{cr}). The comparison between the experimentally measured shock wave locations in the air and the computational results given in Figure 1(b) for different K_2CrO_4 mass concentrations (i.e., absorption coefficients) shows good agreement.

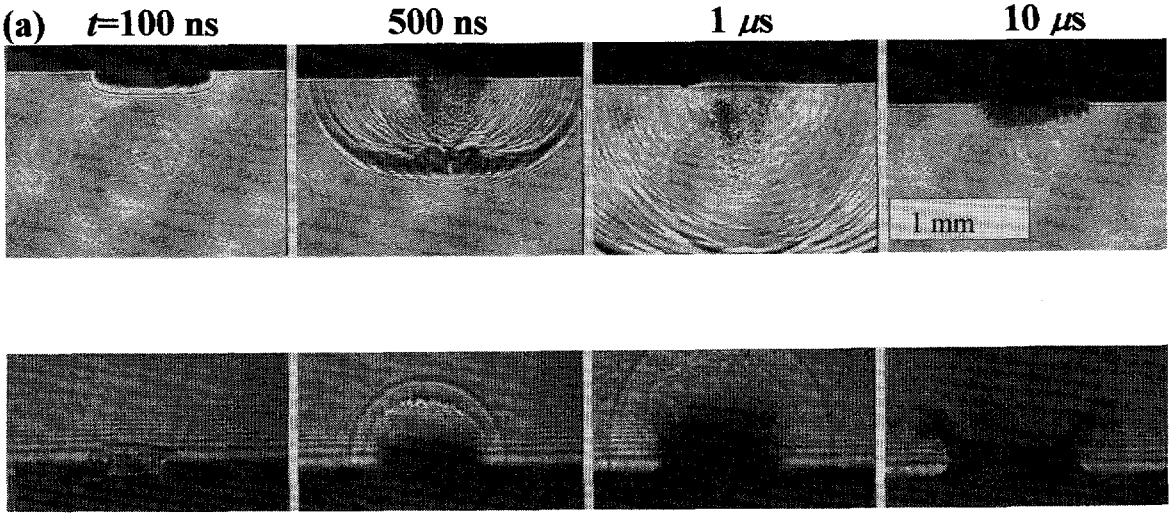

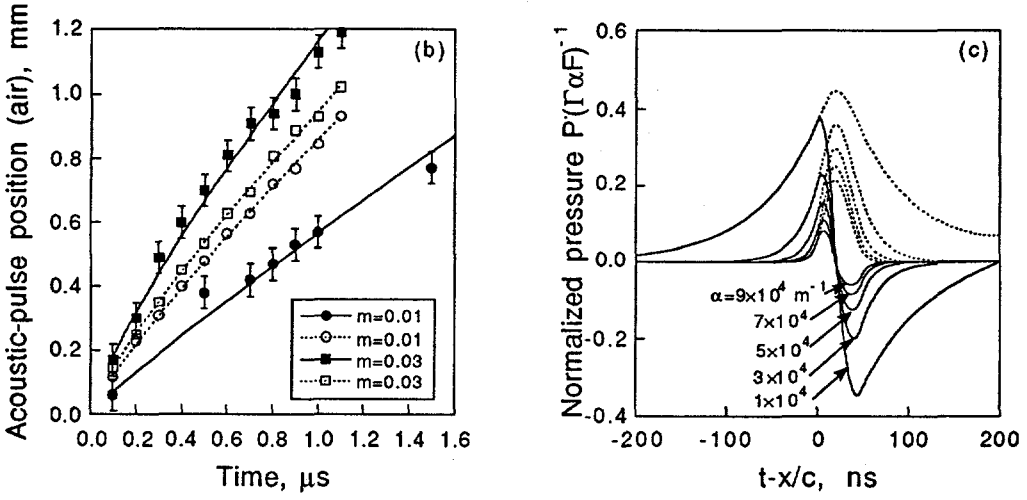

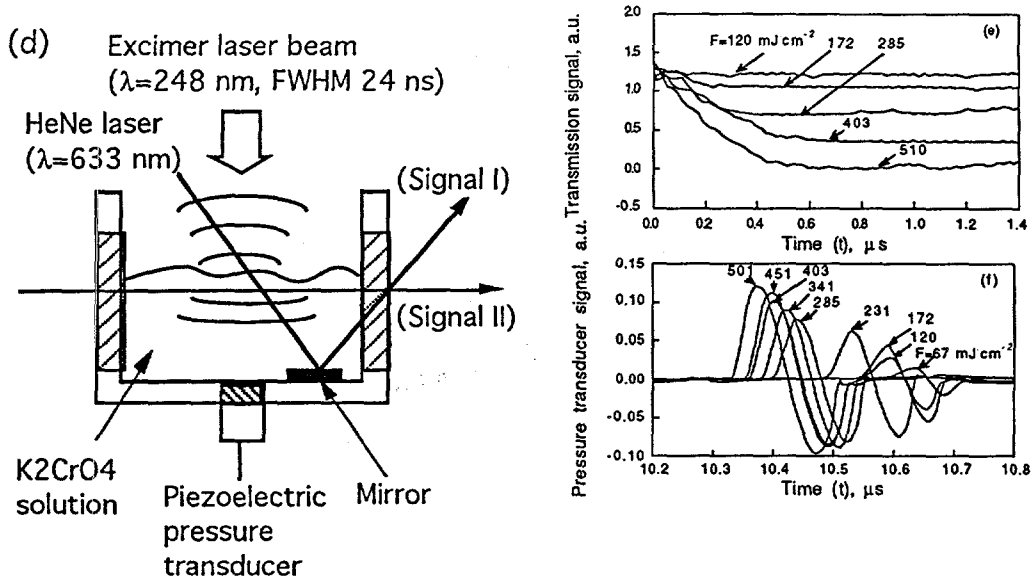

Figure 1 (a) Sequence of Images by Laser Flash Photography in the Liquid (Upper Row) and Air (Lower Row). (b) Measured Propagation Distance of Acoustic Pulses in the Air. (Dashed Lines and Open Markers: Numerical Calculation). (c) Temporal Profiles of Normalized Thermoelastic Stress for Various Absorption Coefficients (t=200 ns; x, Distance from Free Surface to Detector; c, Speed of Sound; Grüneisen Parameter $\Gamma = c^2\beta/C_p$). (d) Experimental Setup for Pressure Measurement, and Optical Transmission Detection. (e) Optical-Transmission Signal. (f) Temporal Shape of Acoustic Pulse in the K_2CrO_4 Solutions for Several Laser Fluences.

The stress field induced by surface heating of a semi-infinite liquid can be modeled based on the thermoelastic expansion of the liquid subjected to transient heating (the so called "thermal shock"). The thermoelastic-stress transients are calculated for excimer-laser pulses having triangular temporal intensity profile and the results are displayed in Fig. 1(c) for various absorption coefficients. The plot shows that the threshold value of the tensile pressure for ablation (F=0.2 ~ 0.4 J/cm^2) is approximately 1.8 ~ 3.6 MPa. The HeNe-laser (λ=633 nm) transmission signal I in Fig. 1(d) represents the collective effect of light scattering by the ablation plume and the vapor-cavity formation in the liquid. Figs. 1(e), and (f) exhibit the temporal profiles of the transmission signal I and the corresponding acoustic transients at various laser fluences (K_2CrO_4 concentration m=0.01 by mass fraction; absorption coefficient α=5.5×10^4 m^{-1}), respectively. The transmission signal starts developing a noticeable drop at a laser fluence of about 160 mJ/cm^2 ,which can be regarded as the "cavity-formation threshold". In the one-dimensional case, the temporal profile of the thermoelastic pressure produced in the presence of a free surface is composed of symmetrical components of compression and rarefaction waves. However, since the recoil momentum supplied by the ablation-plume ejection is balanced by the time-integrated pressure, the positive component of the pressure pulse exceeds the negative one at laser fluences above the ablation threshold. The total recoil momentum calculated by integrating the pressure transient with respect to time indicates that the ablation threshold is between 0.2 and 0.4 J/cm^2. On the other hand, the maximum surface temperature rise obtained by numerical calculation is only 13 ~ 53 K at laser fluences from 0.1 to 0.4 J/cm^2. This verifies that the ablation process is initiated by photomechanical effects at temperatures substantially below the saturation temperature corresponding to the ambient atmospheric pressure. The surface-ablation process can be interpreted in terms of a mechanical "rupture" of the liquid surface effected by large tensile stress [2,3,12].

CO_2-Laser Induced Ablation of Water

In these experiments [13], a CO_2-laser beam was focused on the water surface; the total energy deposited on the liquid was controlled by varying the pulse duration using an acousto-optic modulator. The ablation threshold was determined by observing the formation of surface cavity (i.e., the open hole formed by surface depression) induced by the recoil action of the vapor plume. The inception of ablation (crater formation) occurred at laser fluence F=0.4 J/cm^2 (laser-pulse duration 2 μs). Numerical calculation (heat conduction equation for two-dimensional axisymmetric geometry with temperature dependent thermal properties) yielded maximum temperature rise close to the saturation

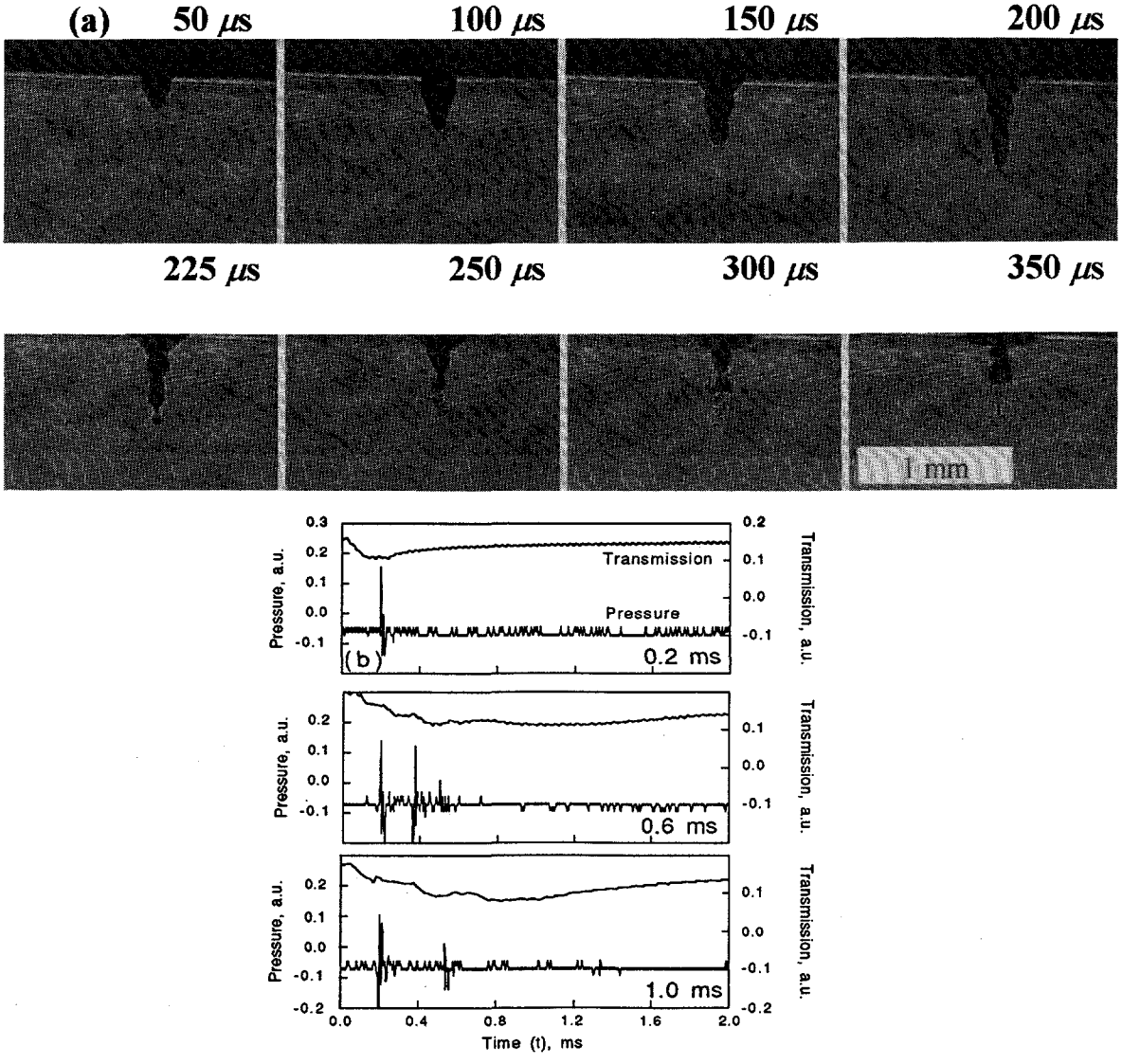

Figure 2 (a) Sequence of Images by Laser-Flash Photography in the Ablation of Water by a CO_2-Laser Pulse. (Beam Diameter, 50 μm; Pulse Duration, 0.4 ms, Power, 4.4 W). (b) Acoustic Transients and Simultaneously Detected Transmission Signals for Several Laser-Pulse Durations (Laser Power Density = 0.22 MW/cm^2).

temperature at the ambient pressure, indicating that the thermodynamic process of the phase transition is largely isobaric.

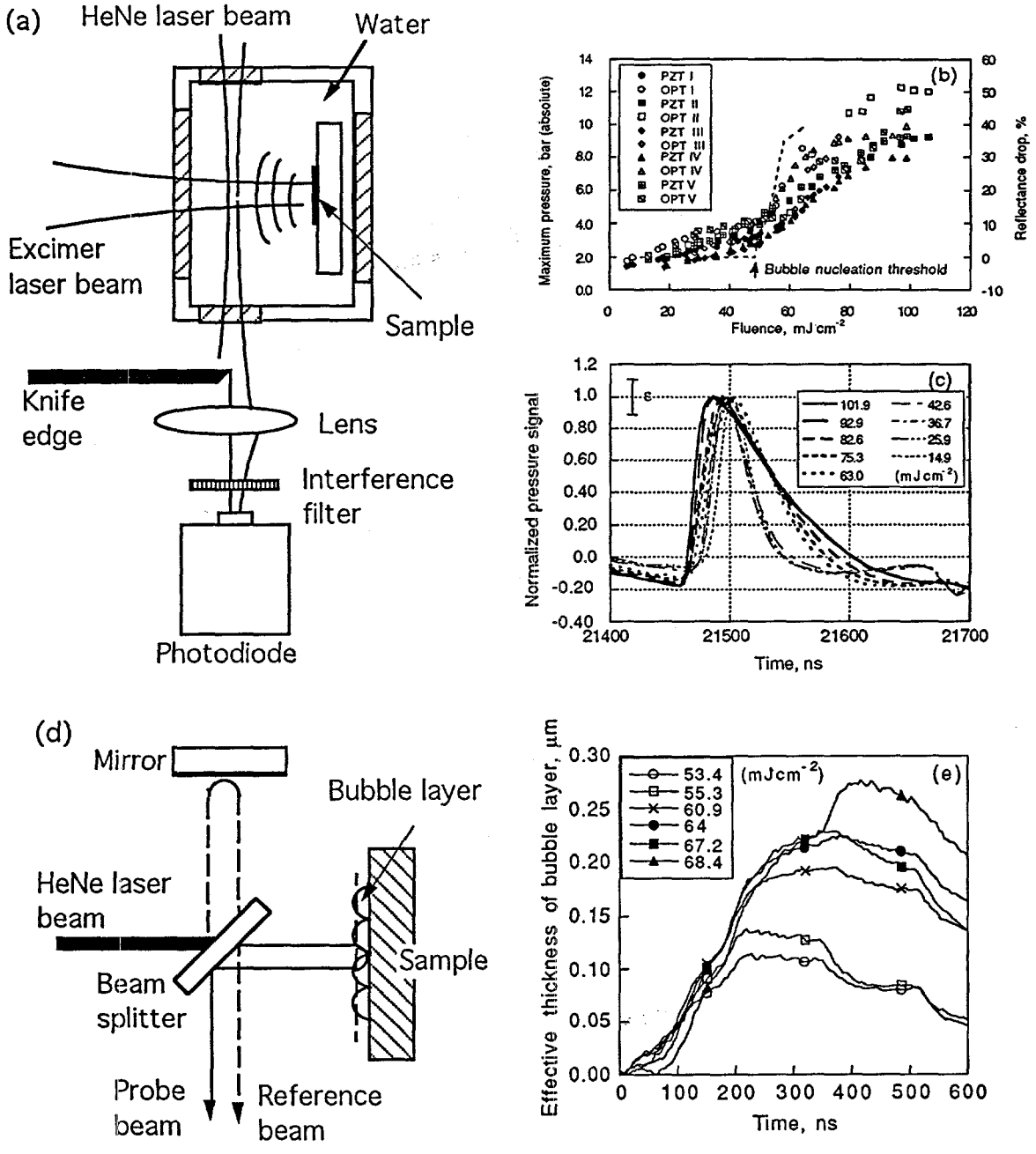

Figure 3 Experimental Setup for (a) Photoacoustic Probe Beam Deflection Technique and (d) Interferometry for Bubble-Kinetics Detection. (b) Pressure-Pulse Amplitudes Measured by Piezoelectric Transducer ("PZT") and Optical Deflection Probe ("OPT"). Dashed Lines Denote the Amplitude of Optical Specular Reflectance Drop. (c) Normalized Pressure Pulses Detected by Piezoelectric Transducer. (e) Effective Thickness Variation of the Bubble Layer.

The physical mechanism of the acoustic-transient generation was elucidated by considering the surface-cavity dynamics visualized by shadowgraph imaging. For laser pulses shorter than 0.2 ms, the surface cavity grows until the end of the pulse due to the recoil momentum supplied by the vapor plume. However, if the laser-pulse duration exceeds 0.2 ms, fragmentation of the cavity takes place, blocking further increase of the cavity depth as shown in Fig. 2(a). Growth of the cavity is obstructed when its depth to radius ratio reaches a certain value, at which instant, the surface cavity is fragmented, creating cavitation bubbles.

Fig. 2(b) displays the acoustic transients together with the simultaneously detected optical-transmission signals (probe II in Fig. 1(d)) for laser-pulse lengths, t_p = 0.2, 0.6, and 1.0 ms. A single acoustic pulse is detected for t_p = 0.2 ms. Further increase of the laser-pulse duration induces multiple acoustic pulses but the first pulse is always observed at around 0.2 ms. The present work confirms the question of stability of the equilibrium profile posed in [14]. A qualitative argument on this instability development can be obtained by considering the vaporization flux (laser-energy supply), hydrostatic pressure and surface tension, with the last two acting as destabilizing forces. The physical origin of the fragmentation of the long-cylindrical vapor cavity can be understood drawing upon the similarity with classic stability theory [15].

VAPORIZATION OF LIQUIDS ON A PULSED LASER-HEATED SOLID SURFACE

The transient development of the bubble nucleation process and the onset of phase change were monitored by simultaneous application of optical reflectance and scattering probes [16,17]. Thermodynamic considerations such as the degree of superheat in a liquid-vapor transition at the nanosecond time scale had never been addressed before this investigation. To this end, a backside photothermal reflectance technique was successfully implemented to measure non-intrusively the temperature field development during the rapid vaporization [18], yielding superheat in excess of 100K to propel vapor growth.

Laser-flash photography showed that a pressure pulse having a flat profile is launched into the liquid, traveling with sonic speed in a direction normal to the irradiated surface. This pressure wave of tens of nanosecond pulse width was detected non-intrusively by a photoacoustic technique with resolution as low as 1 bar [19]. While crossing a probe beam (Fig. 3(a)), a pressure wave introduces a refractive index gradient across the probe beam waist. Transient pressures detected by both a piezoelectric transducer and the photoacoustic (PA) deflection method are shown in Fig. 3(b). When the laser fluence is low, i.e. below the vaporization threshold, the pressure is generated thermoelastically, and has narrow temporal width, scaling with the time required for temperature rise, i.e., the excimer laser pulse width. At fluences exceeding the vaporization threshold, there exists another contribution of stemming from the bubble growth, which prolongs the pressure pulse (Fig. 3(c)).

The nanosecond-laser-induced bubble growth process can be approximated via invoking the picture of a growing thin vapor film. If the surface roughness of the film (or size of the individual bubbles in the early stage) is much smaller than the wavelength of the probe laser beam, a Michelson interference technique (Fig. 3(d)) can be used to detect the thickness of the vapor film (or more precisely, the effective thickness of the bubble layer) [20]. Whereas multiple bubbles form on the surface, their average size is represented by the effective medium thickness displayed in Fig. 3(e), which is less than 0.3 μm for the range of fluences shown. The thickness of the vapor film starts to increase rapidly after the laser-pulse absorption, attaining a maximum value at a few hundred nanoseconds after the laser pulse. On the basis of the interference and scattering measurements, regimes of the bubble growth and collapse process were distinguished. The early stage of bubble growth is largely dominated by an inertia-controlled process, with the bubble growth speed estimated to be of the order of 1 m/s.

OPTICAL PROPERTIES AND RADIATIVE TRANSFER IN POROUS SILICON

Technology's demand for smaller, faster, and more efficient microelectronic devices has spurred the development of advanced materials with novel structures. Porous silicon, an advanced material of great current interest, has a structure characterized by nanometer-sized silicon crystallites, disordered crystallite arrangement, and extremely high surface area. This structure gives porous silicon special properties which make it, unlike bulk silicon, viable for use in optoelectronic applications such as laser-based optical communications [21] or light-emitting diodes (LEDs). As in many microelectronic devices, microscale heat transfer [22] will be an important factor in the performance of optoelectronic devices based on porous silicon.

A new five-level model for radiative transitions has been developed to predict energy absorption in porous silicon on picosecond time scales [23]. Information critical for the development of silicon-based optical devices in applications such as optical switching is provided by this model. Parameters for this model were ascertained from short time scale photoinduced absorption spectra for p-type porous silicon samples. The dual beam picosecond continuum technique [24], a novel pump-and-probe technique, was developed to generate these spectra. This technique is extremely important because it facilitates single-shot, high signal-to-noise ratio measurement of differential absorption/transmission spectra on the picosecond time scale.

The principle of dual beam measurement is to excite a material with a strong pump beam and then to measure transmission through pumped and unpumped regions of the material simultaneously with a pair of weaker continuum probe pulses at various time delays with respect to the pump pulse. The continuum pulses are generated by passing a 1064 nm beam through an H_2O/D_2O cell and a beam splitter. By measuring various time delay points with respect to the pump pulse, the temporal profile of the transmission response can be reconstructed.

Differential transmission spectra for p-type porous silicon samples were obtained from comparison of pumped to unpumped spectra and were integrated over wavelength to yield the integral differential transmission [25]. This result, in Fig. 4, shows increased absorption at very short time scales as compared to steady state. The thermal impact of this increased absorption in porous

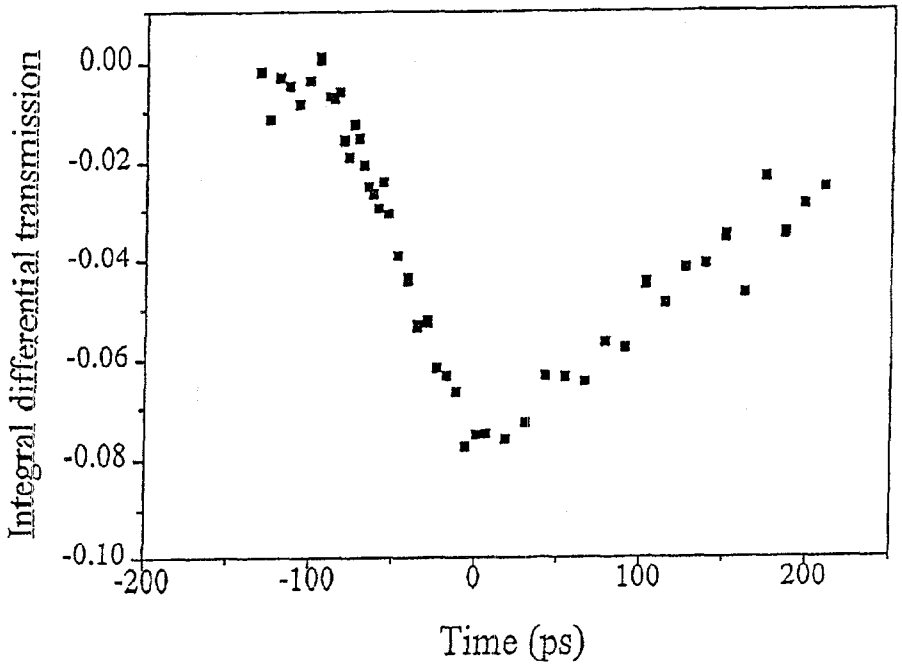

Figure 4 Integral Differential Transmission vs. Time

silicon is significant and must be considered in the design and optimization of high frequency devices and in short-pulse laser processes.

REDUCTION OF STICTION USING ULTRASHORT-PULSE LASER RADIATION

Adsorption of liquid or gas molecules onto surfaces is a frequently encountered problem in micro-manufacturing and material processing. The presence of these molecules may cause leakage current, oxidation, or contamination in microelectronic systems and may increase the incidence of a failure mode called stiction in microelectromechanical systems (MEMS) [26]. By applying ultrashort-pulse laser radiation, undesirable molecules can be desorbed due to the induced electronic excitations [27]. Detailed study of ultrashort-pulse laser interaction with semiconductors has already shown that electrons absorb the incident photon energy first and become "hot", or in other words, attain high kinetic energy. If the laser pulse duration is larger than the characteristic relaxation time, τ_p (on the order of $10^{-12} - 10^{-10}$ seconds), the electrons will give energy to the lattice and return to the ground state, which results in heating of the bulk material. However, if the laser pulse duration is short, a carrier-lattice nonequilibrium state is created in which the population of "hot" electrons will be large. As those electrons have enough energy to change the electronic state of bonded surface molecules, they enable the adsorbed molecules to desorb.

Physical and numerical modeling was performed to study energy transport between the carrier and lattice. Calculation was carried out for an undoped silicon layer ($\sim 2\mu m$ thick) irradiated by a 150 fs laser pulse laser at 790 nm and 3.82 mJ/cm^2[27]. Fig. 5 shows the transient temperature profile at the silicon surface, in which the carrier temperature (a statistical representation for carrier energy) reaches 1600 K while the lattice temperature remains almost unchanged. The highly nonequilibrium state between the carrier and lattice indicates the potential of this technique to electronically desorb unwanted molecules. Compared with other desorption techniques, such as bake-out, hot-air knife, or convection oven drying, the most important advantage of this technique is that it does not cause significant lattice heating. A scaling analysis of carrier and lattice temperature

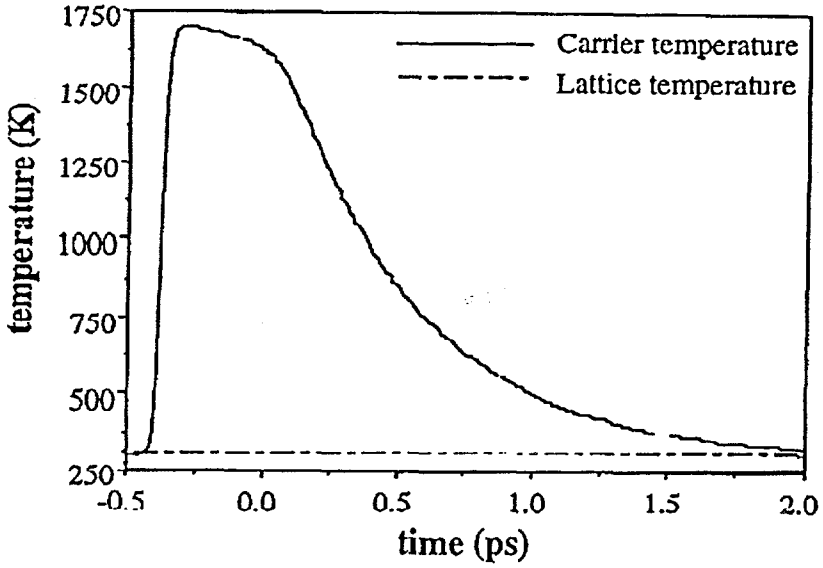

Figure 5 Transient Temperature Profiles at Silicon Surface

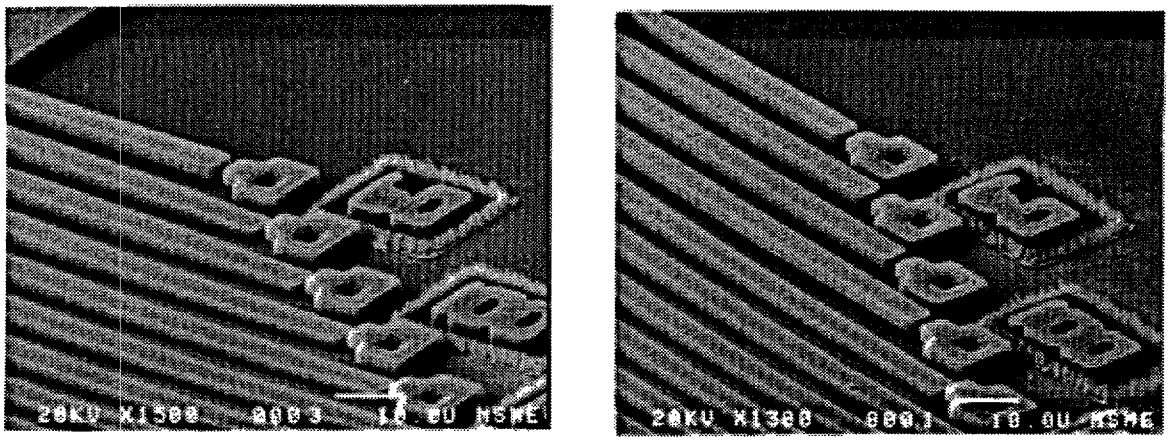

(a) (b)

Figure 6 Polysilicon Cantilevers a) before Irradiation, and b) after Irradiation

indicates that a pulse duration less than one picosecond is required before significant electronic desorption occurs [28].

An experimental demonstration was conducted to further confirm the feasibility of this technique [29]. One of the experiments is shown in Fig. 6, in which the cantilevers are exposed to 150 fs laser with the wavelength of 790 nm and intensity of 18 mJ/cm^{2}for 5 seconds. Three cantilevers were successfully released.

ACKNOWLEDGEMENT

This work was supported by the Department of Energy, Office of Basic Energy Sciences under Grant DE-FG03-95ER14562.

REFERENCES

1. T. F. DEUTSCH, 'Medical Applications of Lasers," *Phys. Today*, October, 56 (1988).
2. A. A., ORAEVSKY, S. L. JACQUES, and F. K. TITTEL, "Mechanisms of Laser Ablation for Aqueous Media Irradiated under Confined-Stress Conditions," *J. Appl. Phys*, 78, 1281 (1995).
3. G. PALTAUF, and H. SCHMIDT-KLOIBER, "Microcavity Dynamics During Laser-Induced Spallation of Liquids and Gels," *Appl. Phys. A* 62, 303 (1996).
4. F. V. BUNKIN, and V. M. KOMISSAROV, "Optical Excitation of Sound Waves," *Sov. Phys. Acou.* 19, 203 (1973).
5. L. M. LYAMSHEV, and L. V. SEDOV, "Optical Generation of Sound in a Liquid: Thermal Mechanism (Review)," *Sov. Phys. Acou.* 27, 4-18 (1981).
6. L. M. LYAMSHEV, and K. A. NAUGOL'NYKH, "Optical Generation of Sound: Nonlinear Effects (Review)," *Sov. Phys. Acou.* 27, 357 (1981).
7. C. B. SCRUBY, and L. E. DRAIN, *Laser Ultrasonics: Techniques and Applications*, Adam Hilger, Bristol (1990).
8. J. B. HÉROUX, S. BOUGHABA, I. RESSEJAC, E. SACHER, and M. MEUNIER, "CO_2 Laser-Assisted Removal of Submicron Particles From Solid Surfaces," *J. Appl. Phys.* 79, 2857 (1996).
9. H. K. PARK, C. P. GRIGOROPOULOS, W. P. LEUNG, and A. C. TAM, "A Practical Excimer Laser-Based Cleaning Tool for Removal of Surface Contaminants, *IEEE Trans. Compon. Packag. Manufact. Techn.* 17A, 631 (1994).

10. D. KIM, M. YE, and C. P. GRIGOROPOULOS, "Pulsed Laser-Induced Ablation of Absorbing Liquids and Acoustic-Transient Generation," *Appl. Phys. A*, in press (1998)
12. J. C. FISHER, "The Fracture of Liquids," *J. Appl. Phys.* 19, 1062 (1948).
14. J. G. ANDREWS, and D. R. ATTHEY, "Hydrodynamic Limit to Penetration of a Material by a High-Power Beam," *J. Phys. D: Appl. Phys.* 9, 2181 (1976)
15. S. CHANDRASEKHAR, *Hydrodynamic and Hydromagnetic Stability*, Dover Publications, Inc., New York (1961).
16. O. YAVAS, P. LEIDERER, H. K. PARK, C. P. GRIGOROPOULOS, C. C. POON, W.P. LEUNG, N. DO, and A. C. TAM, "Optical Reflectance and Scattering Studies of Nucleation and Growth of Bubbles at a Liquid-Solid Interface Induced by Pulsed Laser Heating," *Phys. Rev. Lett.* 70, 1830, (1993).
17. O. YAVAS, P. LEIDERER, H. K. PARK, C. P. GRIGOROPOULOS, N. DO, C. C. POON, and A.C. TAM, "Optical and Acoustic Study of Nucleation and Growth of Bubbles at a Liquid -Solid Interface Induced by Nanosecond-Pulsed Laser Heating," *Appl. Phys. A* 58, 407, (1994).
18. H. K. PARK, X. ZHANG, C. P. GRIGOROPOULOS, C. C. POON, and A. C. TAM, "Transient Temperature Development During the Vaporization of Liquids on a Pulsed-Laser Heated Solid Surface," *J. Heat Transf.* 118, 702 (1995).
19. H. K. PARK, D. KIM, C. P. GRIGOROPOULOS, and A. C. TAM, "Pressure Generation and Measurement in the Rapid Vaporization of Water on a Pulsed-Laser-Heated Surface," *J. Appl. Phys.* 80, 4072 (1996).
20. D. S. KIM, H. K. PARK, and C. P. GRIGOROPOULOS, "Interferometric Study of the Growth of Pulsed-Laser-Generated Submicron Bubble Layer on a Solid Surface," National Heat Transfer Conference, HTD 323, 69, also submitted to *Int. J. Heat Mass Transf.* (1998).
21. B. HAMILTON, "Porous Silicon," *Semicond. Sci. Technol.* 10, 1187 (1995).
22. C. L. TIEN, T. QIU, and P. M. NORRIS, "Microscale Thermal Phenomena in Contemporary Technology," *Thermal Sci. Eng.* 2, 1 (1994).
23. M. C. HIPWELL and C. L. TIEN, "Short Time-Scale Radiative Transfer in Light-Emitting Porous Silicon," to appear in *Int. J. Heat Mass Transfer* (1998).
24. M. C. HIPWELL, C. L. TIEN, X. L. MAO, and R. E. RUSSO, "The Dual Beam Picosecond Continuum Technique for Measurement of Short Time-Scale Transmission Spectra," to appear in *Exptl. Heat Transfer* (1998).
25. M. C. HIPWELL, C. L. TIEN, X. L. MAO, and R. E. RUSSO, "Picosecond Differential Transmission Measurements on Porous Silicon," to appear in *Microscale Thermophys. Eng.* (1998).
26. R. B. COMIZZILI, R. P. FRANKENTHAL, P. C. MILNER, and J. D. SINCLAIR, "Corrosion of Electronic Materials and Devices," *Science*, 234, 340 (1986).
27. K. FUSHINOBU, L. M. PHINNEY, and N. C. TIEN, "Ultrashort-Pulse Laser Heating of Silicon to Reduce Microstructure Adhesion," *International Journal of Heat and Mass Transfer*, 39, 3181 (1996).
28. L. M. PHINNEY, and C. L. TIEN, "Surface Contaminant Removal Using Short-Pulse Lasers," in *Transport Phenomena in Materials Processing and Manufacturing*, HTD-Vol. 336, FED-Vol. 240, A. S. Lavine et al., eds., 55 (1996).
29. N. C. TIEN, S. JEONG, L. M. PHINNEY, K. FUSHINOBU, and J. BOKOR, "Surface Adhesion Reduction in Silicon Microstructures using Femtosecond Laser Pulses," *Applied Physics Letters*, 68, 197 (1996).

NMR STUDIES OF MULTIPHASE FLOWS – III

S. A. Altobelli and E. Fukushima

New Mexico Resonance
Albuquerque, NM 87108, U. S. A.

ABSTRACT

Because Nuclear Magnetic Resonance (NMR) techniques are non-invasive, can image many types of motion, can distinguish materials and are immune to the deleterious effects of opacity they are natural experimental tools for multiphase flow studies. On the other hand, NMR techniques can be slow and have usually provided information on a single phase of a multiphase system. Recent advances in "rapid" imaging and 1-dimensional studies of batch sedimentation show progress in matching NMR imaging time scales to dynamic processes. A new solid/liquid suspension system which allows direct measurement of both phases has also been developed, and is demonstrated in three experimental geometries.

INTRODUCTION

Nuclear Magnetic Resonance (NMR), as practiced in these studies, involves commonplace liquids flowing inside a strong, nearly uniform magnetic field. Protons (^{1}H nuclei) in these liquids resonate with radio frequency (rf) magnetic fields, which allows one to probe the "spin-system" by applying short rf pulses and much slower magnetic field gradients. rf signals elicited from the protons give information on the position and motion of selected parts of the sample, and the spatial and temporal measurement scales can be varied. Parts of the sample may be selected by location and also by type of material. Since the interaction with the proton is mediated by rf, optical opacity is not a problem. Note, however, that the rf wavelength does not

determine the resolution of the measurement. NMR methods have already been applied to several multiphase flows, and we summarize the results to support the idea that useful measurements are possible.

Our recent work has been toward exploiting NMR techniques more fully by developing more rapid measurements and eliminating, or at least skirting, the limitations inherent in doing liquid state NMR. To do rapid imaging, one must develop a plan for scanning that doesn't overtax your instrument and that produces the desired signal to noise ratio. The choice of materials and the arsenal of imaging techniques is restricted. Recent two-dimensional imaging experiments with liquid/solid systems achieving frame rates up to 5 Hz provide indications of the trade-off between imaging speed and quality currently available. Imaging times may also be reduced by lowering the dimensionality of the data. This idea has been applied to the classic problem of batch sedimentation in the last few years, and a new approach to analysis of these experiments is presented here.

Although it is possible to learn many things about suspensions by interrogating a single phase, there are also many important parameters that aren't easily determined. One may, for example, measure the liquid fraction in a voxel and deduce the solid fraction by subtraction. Measuring the velocity of the liquid phase, however, does not in general directly provide the velocity of the solid phase. With NMR imaging, a further complication is that small (sub-voxel size) gas bubbles are not distinguished from, say, plastic particles. Not only does this complicate sample production and make leak prevention crucial, it eliminates the possibility of measurements in three-phase systems. In recent studies of granular flows, we have been able to use liquid state NMR techniques by choosing dry materials containing oils, e.g., natural seeds and grains and manufactured pharmaceutical pills. Incorporating these materials into liquid/solid or gas/liquid/solid flow systems has only been done very recently, and initial results of these experiments will be described.

In terms of the demands placed on the instrument, it is much more difficult to study solids and gases directly via NMR, but some progress has been made on these fronts, too (Kuethe, et al 1998).

BACKGROUND ON NMR APPLICATIONS

NMR of fluid motion is discussed in detail by Callaghan (1991) in the highly recommended book on NMR microscopy. Reviews specific to flowing fluids include Caprihan & Fukushima (1990) and Pope & Yao (1993). Maneval et al (1993) concentrated on applications to multiphase flows. Gladden (1994) has provided a broad and comprehensive review in the engineering literature. The technical details of this type of NMR imaging may be found in these sources, and are not discussed here.

Concentrated Suspensions

There have been several studies of particle migration in concentrated suspensions motivated by ideas of Leighton & Acrivos [1987], both in wide gap Couette flows [Abbott et al 1991; Mondy et al 1994; Corbett et al 1995, Tetlow et al 1998], and in pipes [Altobelli et al

1991, Sinton & Chow 1991, Seymour et al 1993, Hampton et al (1997)]. These studies determined that migration of particles from high shear regions to low shear regions occurs irreversibly, and that migration rate is a function of total strain, and a strong function of particle diameter. Migration rates do not depend on strain rate or the viscosity of the suspending liquid. The NMR data was used to validate the model developed by Phillips et al (1992). A finite volume model of concentrated suspensions in eccentric Couette flow also compared well with NMR image data [Phan-Thien et al 1995]. Hampton et al (1997) measured the fluid fraction and fluid phase velocity in nearly neutrally buoyant suspensions with solid fractions in the range 0-50%. Measurements were made for different ratios of particle to tube diameter as well as for different distances along the flow system in order to determine the scaling for development of the velocity and concentration profiles. Measured profiles were compared to the Phillips model and to a model which explicitly involves the velocity fluctuations of the particles [Jenkins and McTigue 1990, Nott and Brady 1994].

If we compare our early and more recent pipe flow studies [Altobelli et al 1991 and Hampton et al 1997], imaging time has gone from 40 minutes to 8 minutes and the imaging matrix has increased from 32 x 32 to 128 x 128. These improvements were possible mainly because we collected 3-dimensional data in the early study, but only 2-dimensional data in the more recent one.

Granular Flow

It is possible to study granular dynamics using liquid state NMR imaging by judicious choice of materials. The dynamics of mustard seeds, flowing in a rotating, horizontal, half-filled cylinder have been studied in some detail [Nakagawa et al 1993; Yamane et al 1998]. Oil-bearing seeds and grains and liquid-filled pharmaceutical pills are suitable for these studies, which provide information on density variation, depth of flowing layers, and average velocity in the granular media. NMRI techniques have also been useful in studies of flow-induced segregation of granular materials in the same geometry [Metcalf & Shattuck 1996; Hill et al 1997]. In these studies, imaging times were a few minutes and 2-dimensional images of 128 x 128 were made. Velocity and velocity fluctuation images have been made in these flows, and each velocity component requires twice the static imaging time and components of the velocity fluctuation tensor require four to eight times the static acquisition time. For comparison with theory in this field, the so-called granular temperature is an important quantity.

Porous Media Flow

The number and type of NMR porous media studies is growing rapidly. See, for example, Proceedings of the Third International Meeting on Recent Advances in MR Applications to Porous Media in *Magnetic Resonance Imaging* **14**(7/8), 697-1006 (1996).

Both model and natural porous media are being used. Many experiments use special NMR techniques that allow measurements of velocity in the range of a fraction of a mm/s even in the presence of background magnetic gradients due to the media itself. Measurement of velocity correlation functions is important in this field for comparison with theories of dispersive processes.

APPROACHES TO RAPID IMAGING

Rapid two-dimensional imaging

Rapid NMRI techniques were pioneered by Mansfield (1977) and have been extended to measurements of flow velocity more recently. For example, echo-planar sequences were used to make 32x32 two-dimensional in-plane velocity images of turbulent puffs in 56 ms [Kose 1991a] and an equivalent out-of-plane velocity was made in 21 ms [Kose 1991b]. More recently, Lowe and coworkers have measured axial flow velocities in a pipe with a constriction by a technique called RUFIS requiring only 11 ms [Madio et al 1998]. Many rapid imaging techniques can't be implemented on older systems economically.

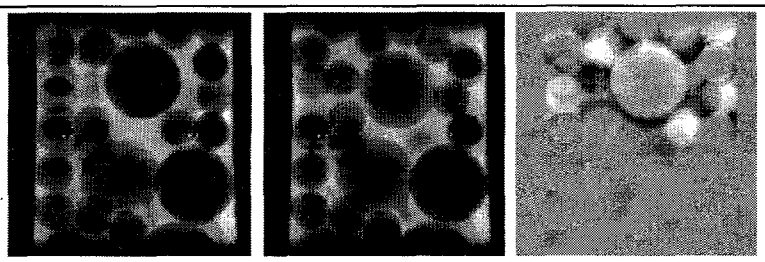

Figure 1. On the left and center, images obtained by averaging 4 successive frames of a RT-NMR image sequence are shown. On the right, the difference shows the flow induced rearrangement of the plastic spheres

It is very useful to see images in "real time" as they are acquired. Some medical imagers have such capabilities but smaller (and cheaper) hardware is now being developed for use in research and we have demonstrated imaging of simple buoyancy-driven multiphase flows [Kose et al 1997]. The images of Figure 1 were acquired with a real-time system and a 4.7T vertical bore magnet. An optimized conventional imaging system generated 128 x 128 images every 900 ms. The images shown are the average of 4 frames. This system makes otherwise impossible sample positioning simple.

Rapid one-dimensional imaging

In systems, or parts of systems, where gradients of concentration or velocity are absent or one-dimensional, NMR experiments can be performed much more rapidly. Two things contribute to this: first, the amount of material contributing to the signal from a voxel is increased, and second, the NMR data for a single projection can be taken in "one-shot". One-dimensional velocity profiles require a reference. The so called PGSE (Callaghan, 1991) experiment typically requires 8-16 datasets, but yields a propagator for each voxel. Exploiting one-dimensional systems may become an important aspect of dynamic NMR imaging.

We have recently started studying a classic 1-d multiphase flow field (Altobelli and Mondy, 1998). Batch flotation experiments were conducted with polydisperse suspensions of noncolloidal spherical glass micro-bubbles in an 80% glycerol 20% water mixture. The initial configuration of the suspensions was spatially uniform with solid fraction ϕ_i. The fluid fraction ρ_c (note: *not* fluid density) was measured as a function of height y and time t by one-dimensional NMR imaging. The continuous phase velocity $u_c(y, t)$ was calculated from the NMR data by an explicit scheme. The disperse phase velocity $u_d(y, t)$ was calculated from ρ_c and u_c, normalized by the Stokes velocity of the mean particle size, and then plotted versus the local solid fraction ϕ by using y and t as parameters. For experiments with ϕ_i of 0.2, 0.35, and 0.49, the points cluster

around a curve $(1-\phi)^{4.4}$ when ϕ is between ϕ_i and the maximum packing fraction ϕ_m. Thus, the kinematic assumption, $u_d = G(\phi)$, made in textbook descriptions of hindered settling also holds in these flows. Therefore, the NMR batch flotation experiment provided measurements of G over nearly the entire range of ϕ at each measurement time interval.

Continuity for the liquid phase can be written

$$\nabla \cdot \rho_c \mathbf{u}_c = -\frac{\partial \rho_c}{\partial t} \qquad [1]$$

so, assuming one dimensional flow, we have

$$\frac{\partial u_c}{\partial y} = \frac{-\frac{\partial \rho_c}{\partial t} - u_c \frac{\partial \rho_c}{\partial y}}{\rho_c} \qquad [2]$$

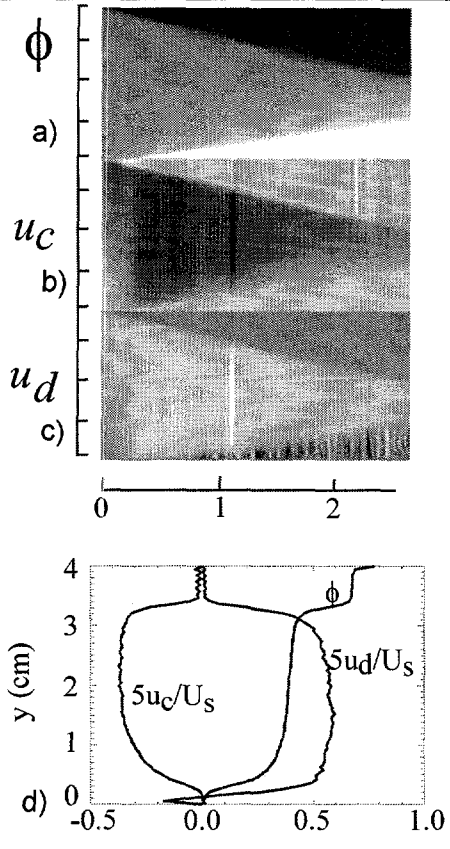

Figure 2. In a) the 1D NMR data scaled to show high solid fraction as dark and low solid fraction as light shades. In b) and c), the computed liquid and solid phase velocity images are shown. In d) a set of curves from t-1hour are plotted.

which is written this way because ρ_c is never zero. The partial derivatives of ρ_c are calculated from the data using three-point Lagrangian interpolation. At each time step, the right side of Equation [2] is evaluated for each y and the resulting $\frac{\partial u_c}{\partial y}$ is then integrated, using a five-point Newton-Coates formula, starting at $y=0$, $u_c=0$, to give u_c for the next time step.

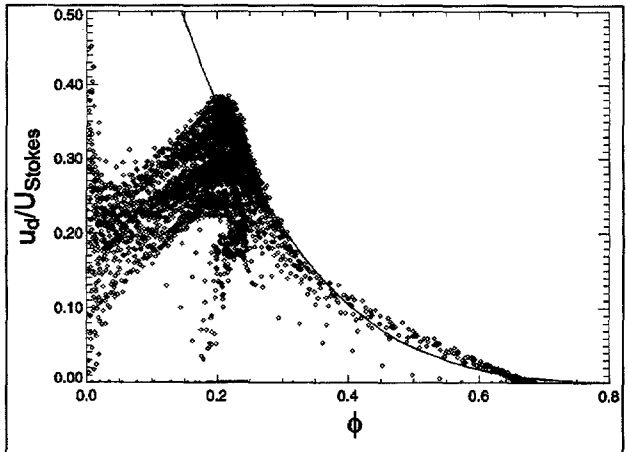

Figure 3 Solid phase velocity, normalized by the Stokes velocity of an average size particle, plotted as a function of solid fraction, point-by-point from images similar to those of figure 2d) and 2a). The overall average ϕ=0.2.

Figure 2a) shows a set of 1D NMR data taken from an initially uniform suspension with overall ϕ=0.35. The calculated velocities are shown in image form in parts b) and c), and curves selected at t=1 hour are plotted in d). The solid phase (glass micro-bubbles) was poly-disperse, and there is no clear layer on the time scale of the experiments. Thus, the hindered settling

function for this mixture can't be determined by conventional methods. Figure 3 shows data obtained at overall ϕ=0.2, where the image values for ϕ and u_d have been plotted point-by-point. The function $(1-\phi)^{4.4}$ has been overlaid for comparison.

NEW SYSTEM FOR MEASURING BOTH LIQUID AND SOLID PHASES

The materials that we image develop weak magnetization when immersed in a magnetic field. The magnetization is proportional to the number of nuclei in the measurement volume and it is established at a rate T_1 that is a material property. The NMR signal is evoked from the induced magnetization. Distinguishing materials based on T_1 is possible by several techniques, but here we make use of the vector character of the induced magnetization. Figure 4, top, shows the time course of magnetization of two materials after their magnetization has been inverted. Note that at t=160 ms the magnetization of the oil-filled pills is zero, but the silicone oil magnetization is large. An experiment performed at t=160ms will give information about the silicone oil alone. Likewise, 600 ms after the inversion, the silicone oil signal will be nulled and an experiment which reflects only the pills can be done.

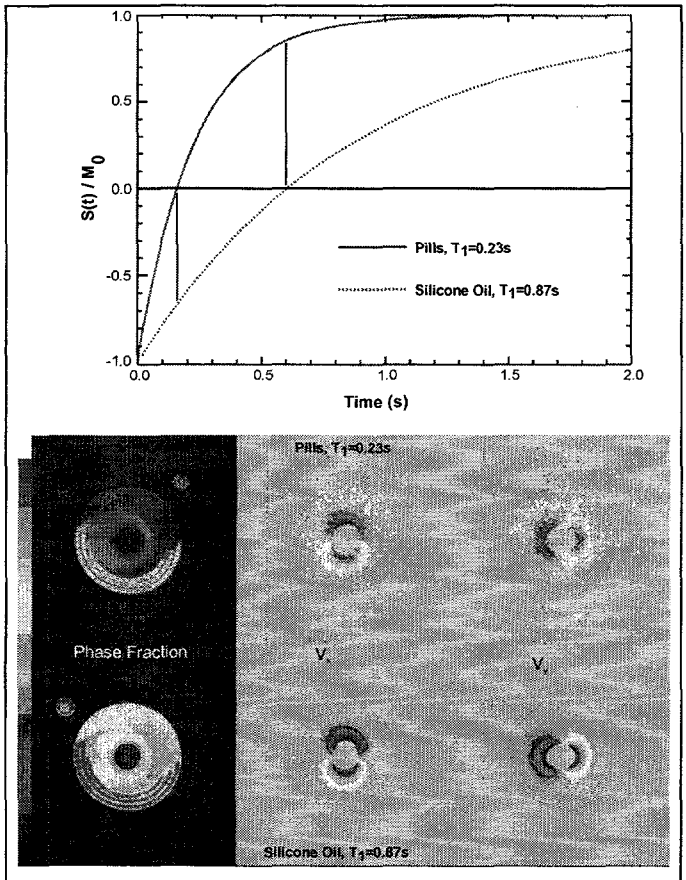

Figure 4 (Top) The liquid and 'solid' phases are distinguished by T_1 relaxation. (Bottom) a set of data obtained in horizontal Couette flow.

Silicone oils are available in a wide range of viscosity, and pills from 1 to 5 mm in outer diameter are available. A neutrally buoyant combination has not been found. The pills are not a perfect solid phase because they are a thin shell filled with a viscous liquid. We do think, however, that this system will generate useful new data in at least three areas: direct measurements of local phase slip, comparisons of velocity fluctuations in both phases, and allowing us to do some gas-liquid-solid measurements.

We are developing experiments in (short) vertical cylinders similar to the batch sedimentation experiments of the previous section, in horizontal rotating cylinders, and in horizontal Couette cells. In the bottom panel of figure 4, a set of measurements of a two-phase Couette flow (driven by rotation of the inner cylinder) are shown. On the left, images show the location of each of the phases, pill images are on top, silicone oil images are on the bottom. In this system, these two pieces of information are redundant. By summing them, a

third phase which gives no NMR signal could be located. The middle and right side pairs of images show the horizontal and vertical velocity components for the two phases.

SUMMARY AND CURRENT DIRECTIONS

Improvements in technique and reductions in the spatial dimensionality of the data have made more rapid NMR imaging possible. We are applying these techniques and a new hardware development which allows 'real-time' observations to various multiphase flow systems.

We have developed a new experimental system that allows measurement of both the liquid and solid phases of a suspension. This will allow new studies of phase slip, coupling between solid and liquid velocity fluctuations, and gas/liquid/solid systems.

Current directions include use of PGSE techniques and one-dimensional imaging in the new system, and further hardware developments required for direct gas and solid phase imaging.

REFERENCES

*Abbott JR, Tetlow N, Graham AL, Altobelli SA, Fukushima E, et al. 1991. Experimental observations of particle migration in concentrated suspensions: Couette flow. *J. Rheol.* 35:773-95

*Altobelli SA, Givler RC, Fukushima E. 1991. Velocity and Concentration Measurements of Suspensions by Nuclear Magnetic Resonance Imaging. *J. Rheology.* 35:721-34

*Altobelli SA, Mondy LA. 1998. Hindered floatation functions from NMR imaging. *Phys. Fluids*, in review

Callaghan PT. 1991. *Principles of Nuclear Magnetic Resonance Microscopy*, Oxford: Clarendon Press. 492 pp.

*Caprihan A, Fukushima E. 1990. Flow Measurements by NMR. *Physics Reports.* 198: 195-235

Corbett AM, Phillips RJ, Kauten RJ, McCarthy KL. 1995. Magnetic resonance imaging of concentration and velocity profiles of pure fluids and solid suspensions in rotating geometries. *J. Rheol.* 39:907-24

Gladden LF, Alexander P. 1996. Applications of nuclear magnetic resonance imaging in process engineering. *Meas. Sci. Technol.* 7: 423-35

*Hampton RE, Mammoli A, Graham A, Tetlow N, Altobelli S. 1997. Migration of Particles undergoing pressure driven flow in a circular conduit. *J. Rheol.* 41:621-40

*Hill KM, Caprihan A, Kakalios J. 1997. Bulk Segregation in Rotated Granular Material Measured by Magnetic Resonance Imaging. *Phys. Rev. Lett.* 78:50-53

Jenkins, JT and McTigue DF 1990. Transport Processes in concentrated suspensions: the role of particle fluctuations. *Two Phase Flows and Waves*, edited by DD Joseph and DG Schaeffer (Springer-Verlag, New York) 70-79.

Kose K. 1991. One-Shot Velocity Mapping Using Multiple Spin-Echo EPI and Its Application to Turbulent Flow. *J. Magn. Reson.* 92:631-35

Kose K. 1991. Instantaneous flow-distribution measurements of the equilibrium turbulent region in a circular pipe using ultrafast NMR imaging. *Phys. Rev. A* 44: 2495-2504

*Kose K, Haishi T, Caprihan A, Fukushima E. 1997. Real-Time NMR Imaging Systems Using Personal Computers. *J. Magn. Reson.* 124:35-41

*Kuethe DO, Caprihan A, Fukushima E, and Waggoner RA. 1998. Imaging lungs using inert fluorinated gases. *Magn. Reson. Med.* 39:85-88

Madio DP, Gach HN, Lowe IJ. 1998. Ultra-fast Velocity Imaging in Stenotically Produced Turbulent Jets Using RUFIS. *Magn. Reson. Med.* 39:574-80

Maneval JE, Powell RL, McCarthy MJ, McCarthy KL. 1993. Magnetic Resonance Imaging of Multiphase Systems. 127-68. In *Particulate Two-Phase Flow.* ed. M. C. Roco. Boston, MA: Butterworth-Heinemann

Mansfield P. 1977. Multi-planar image formation using NMR spin echoes. *J. Phys. C.* 10:L55-58

*Mondy LA, Brenner H, Altobelli SA, Abbott JR, Graham AL. 1994. Shear Induced Particle Migration in Suspensions of Rods. *J. Rheol.* 38:444-52

Metcalf G, Shattuck M. 1996. Pattern formation during mixing and segregation of flowing granular materials. *Physica A.* 233:709-17

*Nakagawa M, Altobelli SA, Caprihan A, Fukushima E, Jeong EK. 1993. Non-invasive Measurements of Granular Flows by Magnetic Resonance Imaging. *Experiments in Fluids.* 16:54-60

Nott PR and Brady JF. 1994. Pressure-driven flow of suspensions: simulation and theory. *J. Fluid Mech.* 275:157-99

Pope JM, Yao S. 1993. Quantitative NMR Imaging of Flow. *Concepts in Magnetic Resonance.* 5:281-302

*Seymour JD, Maneval JE, McCarthy KL, McCarthy MJ, Powell RL. 1993. NMR velocity phase encoded measurements of fibrous suspensions. *Phys. Fluids A.* 5:3010-12

Sinton SW, Chow AW. 1991. NMR Flow Imaging of Fluids and Solid Suspensions I Poiseuille Flow. *J. Rheol.* 35:735-72

*Tetlow N, Graham AL, Ingber MS, Subia SR, Altobelli SA. 1998. Particle migration in a Couette apparatus: Experiment and modeling. *J. Rheol.* 42:307-27

*Yamane K, Nakagawa M, Altobelli SA, Tanaka T, Tsuji Y. 1998. Steady particulate flows in a horizontal rotating cylinder. *Phys. Fluids.* 10(6): (In press)

---

*Indicates one or more authors are from New Mexico Resonance.

USE OF A MODIFIED LANGEVIN EQUATION TO REPRESENT PARTICLE TURBULENCE IN A NONHOMOGENEOUS FIELD

Ilias Iliopoulos and Thomas J. Hanratty

University of Illinois
Urbana, Illinois 61801 USA

ABSTRACT

A modified Langevin equation provides a stochastic model which represents the location and velocity of fluid particles that originate from a point source in a nonhomogeneous turbulence. Similar information can be obtained for solid particles if the Langevin equation is used to represent the fluid turbulence seen by the particles. These methods provide improved theoretical tools to calculate particle distribution and deposition in annular and dispersed flows.

INTRODUCTION

The Eulerian analysis of turbulent transport relates the flux at a fixed location in space, $N = -\overline{u_i c}$, to the gradient of mean concentration, $\overline{u_i c} = D^t \left(dC / dx_i \right)$, where D^t is a turbulent diffusion coefficient. A mass balance equation is used to calculate the concentration field. The Lagrangian approach describes the concentration field as resulting from a distribution of sources and sinks. The theoretical problem is to describe the behavior of a point source.

Lagrangian methods are attractive because the physics emerges in a more natural way and because they provide a sounder analysis in many cases. Advances in developing Lagrangian methods have been handicapped because of the difficulty of carrying out laboratory studies. However, the availability of supercomputers has opened new opportunities. This paper presents results of studies of the change of the location and the velocity of fluid particles and of solid particles that originate from a point source in a direct numerical solution (DNS) of turbulent flow in a channel. These are used to investigate the use of a stochastic method that represents the change of the fluid velocity with time along a typical trajectory of a fluid or of a solid particle. A statistical representation of the behavior of

a point source is obtained by averaging results from a large number of trajectories. The outcome of this study is the demonstration that a Langevin equation, which is adapted to a nonhomogeneous field, is an attractive model for the fluid turbulence.

The motivation for this work comes from studies of gas-liquid flows in pipes. A fundamental issue is the understanding of turbulence characteristics of droplets in a dispersed flow and their deposition on a wall. A number of important results have been obtained on the behavior of particles in a homogeneous, isotropic turbulence, but progress has been much slower in developing general ways to deal with nonhomogeneous fields.

Particle deposition may be viewed as occurring in two steps, diffusion to the vicinity of a wall and free-flight to the wall. An important parameter is the inertial time constant of the particle, τ_p, made dimensionless with the friction velocity and the kinematic viscosity. For aerosols, where $\tau_p^+ < 20$, free-flight starts inside the viscous wall region. An understanding of the influence of turbulence nonhomogeneities is of first order importance [1]. For the more massive droplets in an annular flow [2], and for sediment transport [3], $\tau_p^+ > 20$ and free-flight starts outside the viscous wall region. Nonhomogeneities close the wall are, thus, playing a minor role. However, both annular flow and sediment flow involve particle trajectories whereby particles originate at the wall and eventually deposit. In addition, gravitational forces can play an important role. Because of the complexity of these trajectories the classical (Eulerian) diffusion equation has conceptual difficulties.

DISPERSION OF FLUID PARTICLES

Any discussion of turbulent dispersion of fluid particles should start with Taylor's theory for a homogeneous, isotropic turbulence. Define $X(t)$ as the displacement along one coordinate, of a fluid particle which was at x=0 at t=0. The average for a large number of paths, $\langle X(t) \rangle$, is zero. However, $\langle X^2(t) \rangle$ is not zero and would be a measure of the spread of the particles. For molecular diffusion $2D = d\langle X^2 \rangle / dt$, where D is the molecular diffusion coefficient. A similar equation can be used to describe a turbulent diffusion coefficient which is a function of time, $E(t)$. For $t \to 0$ $E(t) = \overline{u^2} t$, where u is a component of the fluctuating velocity. For $t \to \infty$ $E(t) = \overline{u^2} \tau_L$, where τ_L is the Lagrangian time scale, $\tau_L = \overline{u^2} \int_o^\infty R_L(t)\,dt$, and R_L is the Lagrangian correlation coefficient, $R_L(t) = \langle u(0)u(t) \rangle / \langle u^2 \rangle$. The critical problem has been to adapt this theory to a nonhomogeneous field.

A modification of the Langevin equation developed by Thomson [4] is explored. Let $\vec{U}(t)$ be the velocity a fluid particle which had velocity $\vec{U}_o$ at the origin, $\vec{x}_o$, at t=0. This can be considered to be the sum of the average fluid velocity at $\vec{x}$ and a fluctuation, $\vec{u}$. The following equation is used to describe the change with time of a component of $\vec{u}$:

$$\frac{d\left(\frac{u_i}{\sigma_i}\right)}{dt} = -\frac{u_i}{\sigma_i \tau_i} + d\mu_i, \qquad (1)$$

where σ_i is the root-mean square of u_i in an Eulerian framework. Since a fully-developed flow is considered σ_i is only a function of the coordinate perpendicular to the wall, as is the average velocity in the flow direction, $\overline{U}_x$. The first term on the right side of (1) is a deterministic restoring force; the second is a random number which is uncorrelated in successive time intervals. For a homogeneous field, σ_i and τ_i are constant and the Lagrangian correlation coefficient is given by $R_L = exp(-t/\tau_L)$, with $\tau_i = \tau_L$.

To use (1), it is necessary to define the probability function $d\mu_i$ in terms of the Eulerian probability function for u_i. This is done by taking an ensemble average of (1). For the case being considered,

$$< d\mu_y >= \left(d\sigma_y / dy\right)dt \qquad (2)$$

This term opposes the tendency of fluid particles to move from regions of large turbulence to regions of low turbulence. It may be interpreted as resulting from a mean pressure gradient. Similarly, the following relations are obtained for higher moments, if an ergodic hypothesis is made, whereby Eulerian time averages are substituted for ensemble averages:

$$< d\mu_y^2 >= \left[\frac{2}{\tau_y} + D\left(\overline{u_y^2} / \sigma_y\right)\right]dt \qquad (3)$$

$$< d\mu_y^3 >= \left[\frac{3}{\tau_y}\frac{\overline{u_y^3}}{\sigma_y^3} + D\left(\overline{u_y^4} / \sigma_y^3\right) - 3D\sigma_y\right]dt \qquad (4)$$

$$< d\mu_y^4 >= \left[\frac{4}{\tau_y}\frac{\overline{u_y^4}}{\sigma_y^4} - \frac{12}{\tau_y} + D\left(\frac{\overline{u_y^5}}{\sigma_y^4}\right) - 4\frac{\overline{u_y^3}}{\sigma_y^3}D\sigma_y - 6D\left(\frac{\overline{u_y^3}}{\sigma_y^2}\right)\right]dt \qquad (5)$$

Here, $D=d/dy$.

The analysis is implemented by representing $d\mu$ as a sum of two Gaussian distributions

$$d\mu = pN_1\left(\mu_1, \sigma^2\right) + (1-p)N_2\left(\mu_2, \sigma^2\right) \qquad (6)$$

where μ_1, μ_2 are the means and σ^2, the variances of N_1 and N_2. Parameters p, μ_1, μ_2, σ^2 are selected so as to give the correct $< d\mu_1 >$, $< d\mu_2^2 >$, $< d\mu_3^3 >$, $< d\mu_4^4 >$.

The path of a fluid particle is obtained from the fluctuating velocity field, given by (1), and the known mean velocity by solving the equation $du_i^p / dt = U_i\left(x_o, t\right)$.

DISPERSION OF SOLID PARTICLES

For the situation considered in this paper, the path of a solid particle can be defined by considering only gravity and drag forces. The change in the velocity of the particle is given by

$$\frac{dV_i}{dt} = -\frac{3}{4}\frac{\rho_p}{\rho_F}\frac{C_D}{d_p}\left|\vec{V}-\vec{U}\right|\left(V_i-U_i\right)-g_i\left(1-\frac{\rho_F}{\rho_p}\right)\rho_p \qquad (7)$$

where C_D is the drag coefficient, and the path is obtained with the equation $du_i^p / dt = V_i\left(x_o, t\right)$.

The problem in solving (7) is the specification of $\vec{U}$. In the experiments in a DNS of channel flow, this velocity is given by the DNS at the position of the particle. In the model, U_i is given by (1).

However, there is a conceptual problem since (1) gives the change of velocity along the path of a fluid particle. In solving (7) the fluid velocity needs to be known along the path of a solid particle, which can be different. Therefore, the du_i / dt term appearing in (1) is now considered to be the time change of the fluid velocity seen by the solid particle. The term given by (2) can be interpreted as contributing to a mean pressure gradient in the fluid through which the particle is moving. Solid particles will tend to move from regions of high turbulence to regions of low turbulence. However, unlike the case of fluid particles, the mean pressure gradient in the fluid is not sufficient to oppose this tendency. As a consequence, a turbophoretic drift of solid particles occurs. A difficulty is using (3), (4), (5) exists in that derivatives in time of statistical properties of the fluid turbulence are replaced by substantial derivatives. However, the errors involved with this substitution will not be serious since they occur in terms in (3), (4), (5) which, usually, are not significant.

The principal change in using (1) is that the time constant, τ_i, will be different from that used for fluid particles. Some guidance on this matter can be obtained from work of Friedlander [5] and of Reeks [6], for homogeneous isotropic turbulence. These analyses show that τ_i / τ_L, for the case of zero gravitational effects, increases only by about 30 per cent as τ_L / τ_P varies from 1 to ∞. The effect of gravity is to cause a mean drift velocity, u_T. The influence of $u_T / \left(\overline{u^2}\right)^{1/2}$ is to decrease τ_i / τ_L. The magnitude of this effect, again, can be estimated from the analysis of Reeks.

RESULTS FOR FLUID PARTICLES

Fluid particle dispersion was studied for a source located at the edge of the viscous wall layer, $y^+ = 40$, so as to emphasize the influence of turbulence nonhomogeneities. Calculations with the Langevin model were found to agree reasonably well with the computer experiments by simply using a constant value of τ_i. However, better agreement was obtained by assuming that $\tau_i v^* / H$ is constant only beyond $y^+ = 40$. In the immediate vicinity of the wall $\tau_i v^{*2} / \upsilon$ was assumed to equal the Eulerian time constant. A signoidal curve was used to interpolate between the value at the wall and the value for the outer flow.

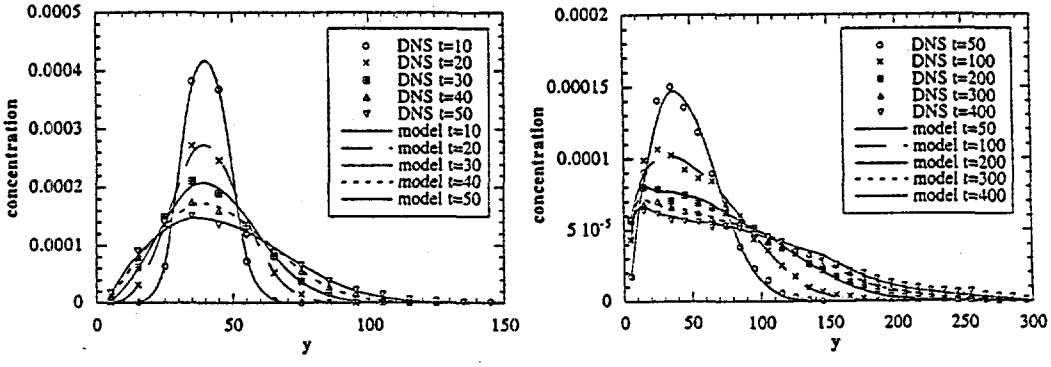

Figure 1. Concentration Profiles for Small and Large Times

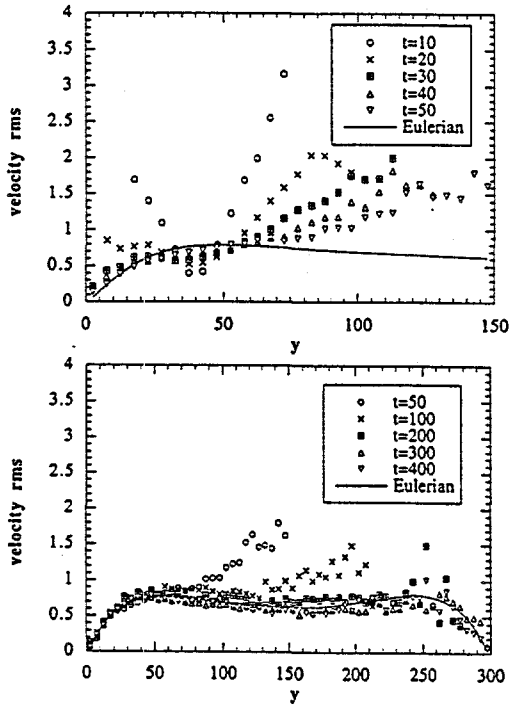

Figure 2. Root-Mean Squared Values of u_y Obtained from Computer Experiments

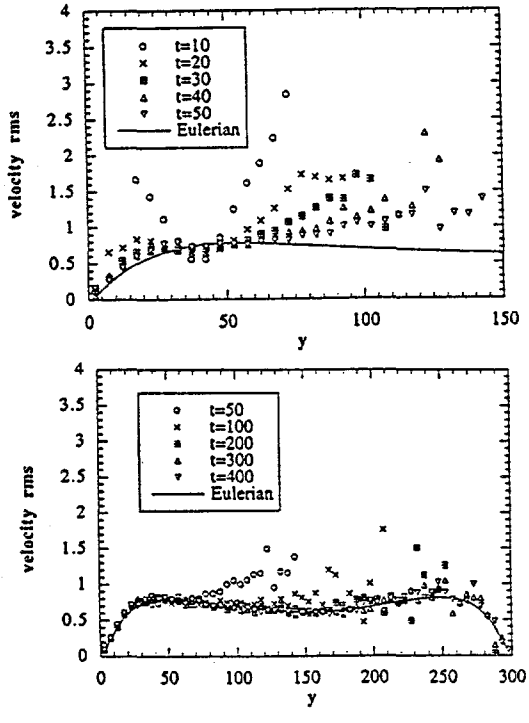

Figure 3. Root-Mean Squared Values of u_y Obtained with the Model

Figure 1 compares concentration distributions obtained in the computer experiments (the points) to calculations with the model (the curves). The ordinate is the distance from the wall made dimensionless with wall parameters. For small times a maximum is observed close to $y^+ = 40$, which is the origin for the particle paths. For t=∞ the particles will uniformly fill the whole channel. Good agreement is noted between the computer experiments and the model. Calculations with $< \mu_y >= 0$ give the unphysical result of an accumulation of fluid particles at the wall. Clearly, the use of (2) is necessary. Streamwise concentration profiles calculated with the model are also found to agree with the results from the computer experiments.

Figures 2 and 3 compare root-mean squared values of u_y at small and at large times. The curve represents Eulerian measurements. It is expected that $\left(\overline{u_y^2}\right)^{1/2}$ should equal the Eulerian results at very large times when the particles fill the channel. The model is seen to agree with the computer experiments. Similar agreement is obtained for the skewness of u_y.

RESULTS FOR SOLID SPHERES

In the study of the dispersion of solid spheres the particles were admitted to the field at the same velocity as the fluid. The channel was horizontal so that gravity was acting in the minus *y*-direction. A trajectory was terminated when the particle settled on the bottom wall. The conditions for the experiment were $\tau_p^+ = 20$, $\rho_p / \rho_F = 2650$, and $\left(\tau_L / \tau_p\right) = 0.7$. The ratio of the free-fall velocity to friction velocity was $u_T^+ = 0.46$ and the dimensionless radius of the particle, $a^+ = 0.18$.

In the model calculations the velocity of the fluid seen by the particles was represented by the Langevin equation. The time-constants were adjusted to be less than those characterizing the paths of fluid particles. The figures shown in this paper used τ_y, τ_z and τ_x that were respectively, 0.8, 0.8 and 0.5 of the values used for fluid particles. Results are presented in dimensionless form, where all velocities are made dimensionless with the friction velocity and all lengths are scaled with the ratio of the kinematic viscosity and the friction velocity.

Concentration profiles in the *y*-direction are shown in figure 4. Since the particles are removed from the field when the strike the bottom wall, no particles are left at a large time. Calculations of the number of particles remaining at different times (figure 5) give a measure of the rate of deposition. Good agreement between the model and the computer experiments is displayed in figures 4 and 5. Good agreement is also found for concentration profiles in the *x*-direction, for correlation coefficients of the fluctuating particle velocity, for correlation

coefficients of the fluctuating fluid velocity seen by the solid particles, and for profiles of the velocity fluctuations of the particles.

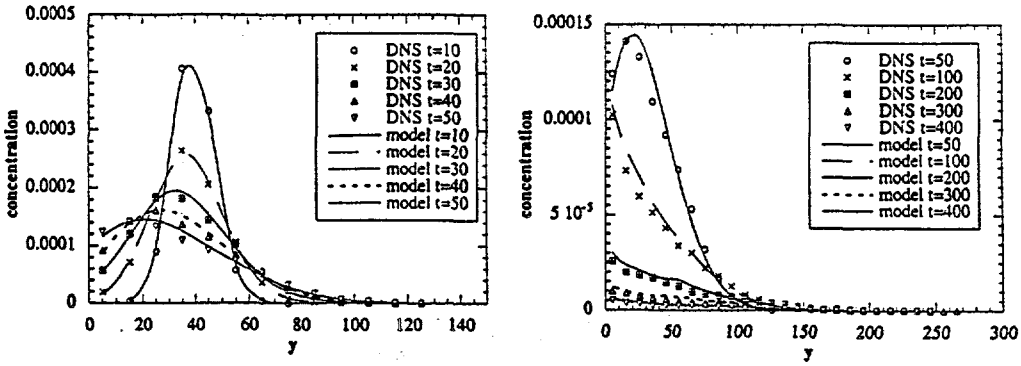

Figure 4. Concentration Profile of Solid Particles in the y-Direction.

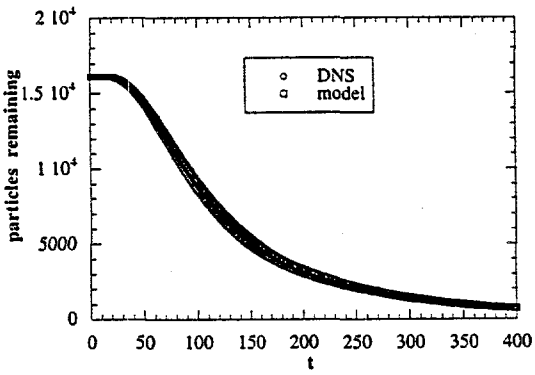

Figure 5. Particles Remaining in the Field at Different Times

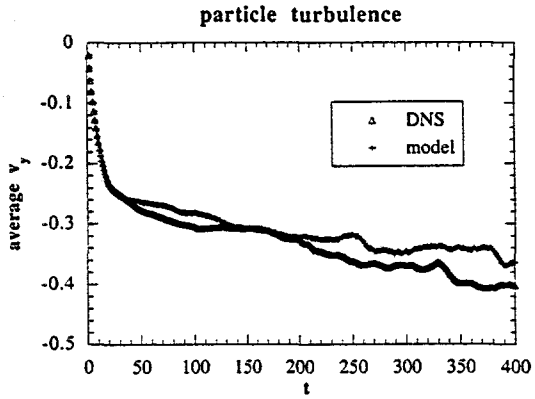

Figure 6. Mean velocity in the y-Direction of Particles in the Field at Different Times

Figure 6 gives the mean velocity in the y-direction of particles in the field at different times. The dimensionless terminal velocity equals -0.5. It is seen that the assumption, usually made in Eulerian analyses, that all the particles have a mean velocity in the y-direction equal to $-u_T$ is incorrect. A closer examination of the results in figure 6 reveals that the particles closer to the wall reach the terminal velocity. In fact, the deposition velocity equals the terminal velocity for $t > 100$. Figure 7 gives results from the computer experiment for root-mean square of the velocity in the y-direction. The large values of v_y-rms at the wall are a consequence of the influence of the settling velocity. If only results for which the mean velocity of the particles equals the terminal velocity ($y<100$; $t \geq 100$) are considered, a fluctuating v_y around u_T can be considered. The root-mean-square of v_y then equals zero close to the wall and is about 0.7 of the Eulerian value at larger y. This is consistent with calculations of Reeks [6] for a homogeneous isotropic field. Figure 8 gives results for the fluctuations of the x-velocity component (around the Eulerian mean velocity). Particularly noteworthy are the large fluctuations close to the wall, which could not be anticipated from calculations for a homogeneous field. These fluctuations result from transport of particles with large inertia from regions of high mean velocity to regions of low mean velocity.

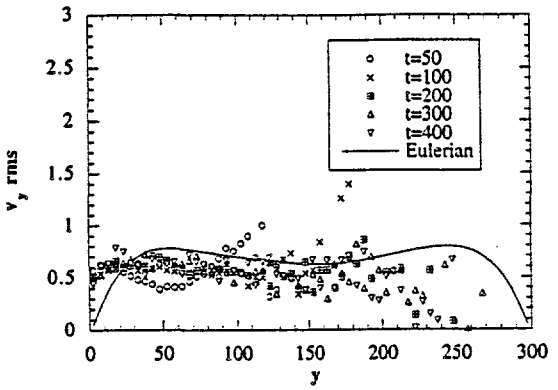

Figure 7. Root-Mean Square Values of the y-Velocity Component from the Computer Experiment

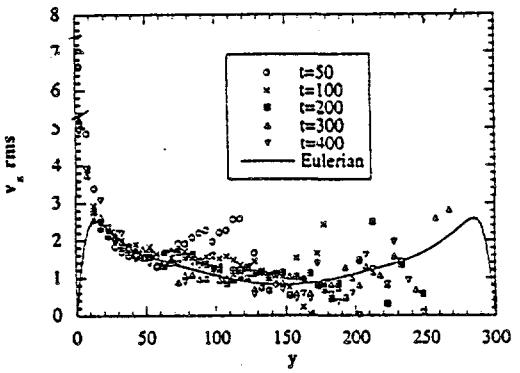

Figure 8. Root-Mean Square of Velocity Fluctuations in the x-Direction Relative to the Eulerian Mean Velocity

ACKNOWLEDGEMENT

This work has been supported by the U.S. Department of Energy and by the National Science Foundation.

REFERENCES

1. J. W. BROOKE, T. J. HANRATTY and J. B. McLAUGHLIN, "Free-Flight Mixing and Deposition of Aerosols," *Phys. Fluids* 6, 3404 (1994).

2. J. L. BINDER and T. J. HANRATTY, "Use of Lagrangian Methods to Describe Drop Deposition and Distribution in Horizontal Gas-Liquid Annular Flows," *Int. J. Multiphase Flow* 18, 803 (1992).

3. J. L. BINDER and T. J. HANRATTY, "Use of Lagrangian Statistics to Describe Slurry Transport," *A.I.Ch.E. Jl.* 39, 1581 (1993).

4. D. J. THOMSON, "A Random Walk Modelling of Diffusion in Nonhomogeneous Turbulence," *Q.J.R.Met.Soc.* 110, 1107 (1984).

5. S. K. FRIEDLANDER and H. F. JOHNSTONE, "Deposition of Suspended Particles from Turbulent Gas Streams," *Ind. Eng. Chem.* 49, 1151 (1957).

6. M. W. REEKS, "On the Dispersion of Small Particles Suspended in an Isotropic Turbulent Field," *J. Fluid Mech.* 83, 529 (1977).

CRITICAL HEAT FLUX IN SMALL DIAMETER CHANNELS

ISSAM MUDAWAR

Boiling and Two-Phase Flow Laboratory, School of Mechanical Engineering,
Purdue University, West Lafayette, Indiana 47907, U.S.A.

ABSTRACT

Ultra-high critical heat flux (CHF) data were obtained using high mass velocity, subcooled water flow through short, small diameter tubes. These tests produced the highest CHF of q_m = 27,600 W cm^{-2} reported in the literature for a uniformly heated tube. The data include broad ranges of tube diameter (D = 0.406 to 2.54 mm), mass velocity (G = 5000 to 134,000 kg m^{-2} s^{-1}), inlet temperature (T_i = 18 to 70 °C), and outlet pressure ($P_{p,o}$ = 2.5 to 172.4 bars). CHF increased with increasing mass velocity, increasing subcooling, decreasing tube diameter, and decreasing heated length-to-diameter ratio. This phenomenon was accompanied by physical "burnout" of the tube wall near the exit. Pressure drop for most conditions was fairly constant over the entire range of heat fluxes up to CHF, proving CHF was triggered even with negligible net vapor production. A new CHF correlation was developed whose accuracy surpasses those of all previous correlations in predicting ultra-high CHF data.

INTRODUCTION

Critical heat flux (CHF) refers to the heat transfer limit causing a sudden decrease in the heat transfer coefficient and possible catastrophic failure of a device in which evaporation or boiling is occurring. The high heat dissipation rates (greater than 100 W cm^{-2}) required in the electronics industry (e.g., supercomputers, power devices, military avionics modules) can be achieved without exceeding CHF by using relatively low mass velocity, flow boiling of dielectric coolants in small diameter channels [1-3]. On the other hand, cooling of devices such as high-power lasers, rocket nozzles, fusion reactor components, and particle accelerator targets necessitate what can be referred to as ultra-high heat flux cooling technologies. The heat flux requirements in these devices are roughly two orders of magnitude greater than those of electronic cooling. Heat

loads for fusion reactor components, for example, require dissipation of heat fluxes on the order of 10,000 W cm^{-2} [4]. Since these heat fluxes exceed the CHF attainable with common flow boiling systems, the ability to both greatly increase and predict the magnitude of CHF is of paramount importance to ultra-high heat flux applications. High mass velocity, subcooled flow boiling of water is required to insure that the extreme operating conditions in these applications maintain heat fluxes in the nucleate boiling regime safely below CHF.

Cooling Configurations

There are two main configurations for adaptation of small diameter two-phase flow to dissipate high heat fluxes. These are direct cooling and indirect cooling. As shown in Fig. 1(a), direct cooling involves immersion of the heat dissipating surface directly in a liquid coolant. This scheme shortens the thermal resistance between the surface and the coolant, enabling the dissipation of large heat fluxes at relatively low surface temperatures. However, the main drawback of this system is the need to ensure electrical and chemical compatibility between the device itself and the coolant. In electronic cooling, for example, direct cooling requires that the coolant be both inert and possess good dielectric properties. Only a few liquids are presently available (e.g., 3M's Fluorinerts) which satisfy these stringent requirement. An example of the direct cooling configuration is the cooling module developed for military avionics by Jimenez and Mudawar [5] and illustrated in Fig. 2.

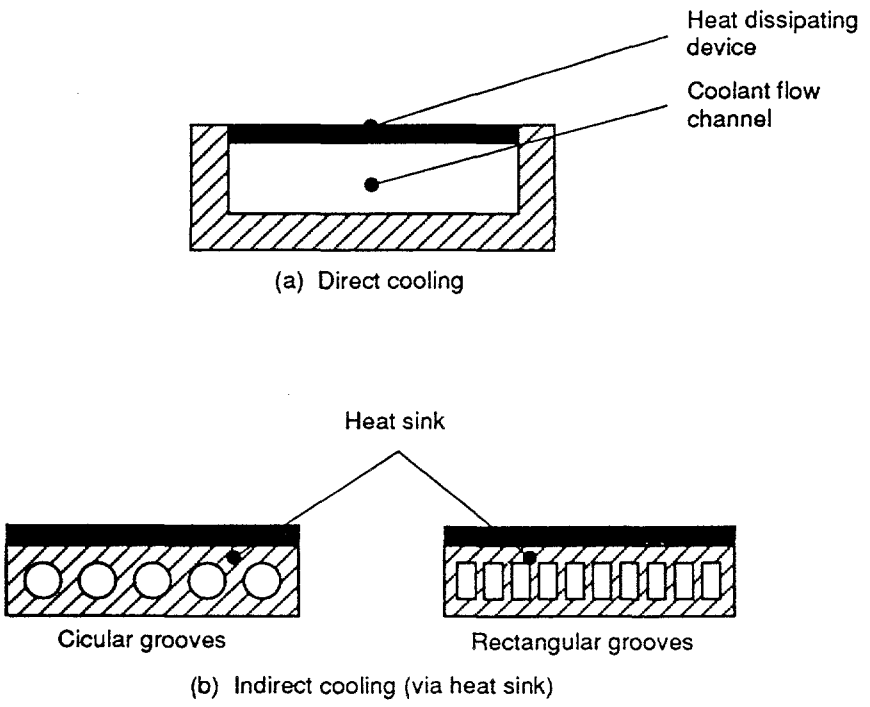

Figure 1. Small-Channel Diameter Two-Phase Heat Dissipation Using (a) Direct Cooling and (b) Indirect Cooling (Via Heat Sink).

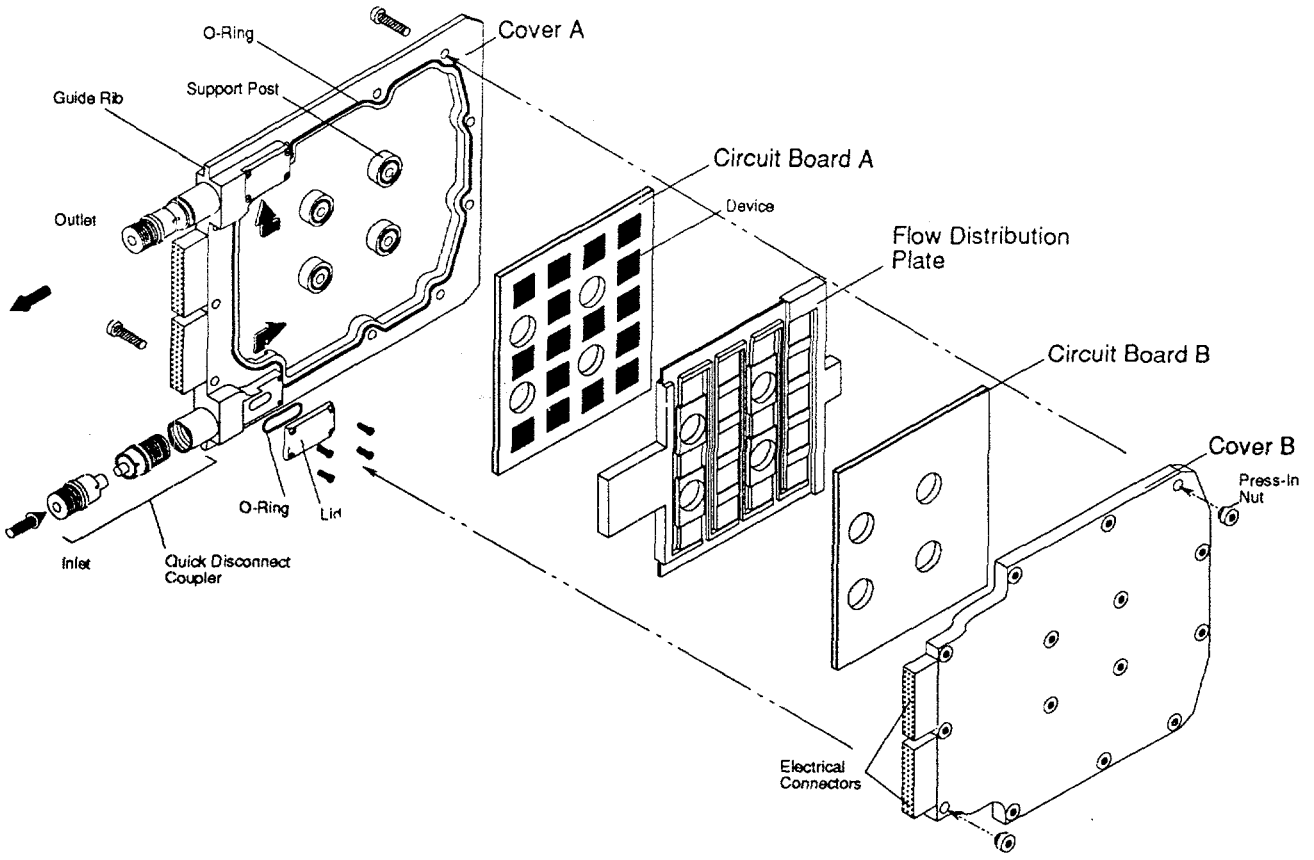

Figure 2 Avionics Module Utilizing Direct Cooling Configuration [5].

Figure 1(b) shows an alternative cooling scheme involving the use of a metallic heat sink to conduct the heat away from the heat dissipating surface to a coolant which is pumped inside circular or rectangular grooves in the heat sink. This scheme facilitates the use of essentially any coolant, providing the thermal engineer with great flexibility in coolant selection. However, indirect cooling increases the thermal resistance between the surface and the heat sink due to the heat diffusion resistance in the heat sink itself. An example of the indirect cooling configuration is the heat sink developed by Bowers and Mudawar [1-3] for computer electronics and shown in Fig. 3.

CHF Regimes

Low and high mass velocity flows are characterized by drastically different flow patterns as well as unique CHF trigger mechanisms. Shown on the left-hand side of Fig. 4 is a subcooled liquid entering a uniformly heated tube at low mass velocity. The combination of low mass velocity and a long tube often results in a near saturated vapor flow at the tube exit. Boiling occurs downstream from the inlet as the flow pattern develops from bubbly to slug and/or churn-turbulent, followed by annular. The boiling subsides when the liquid film in the annular regime becomes too thin to sustain bubble nucleation and forced convection heat transfer to the film, along

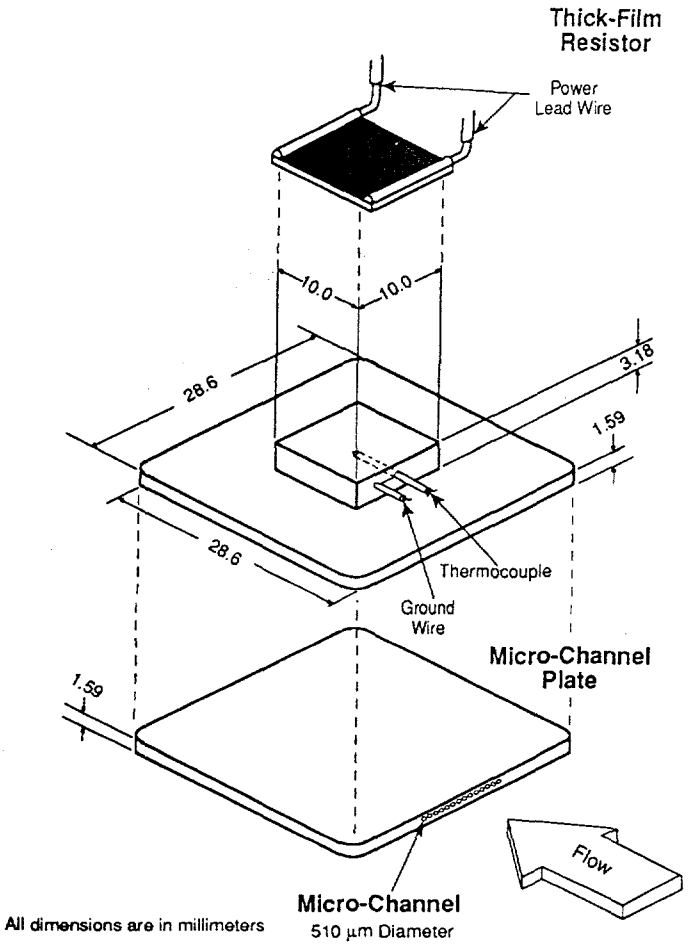

Figure 3. Micro-Channel Heat Sink [1].

with interfacial evaporation, ensue. Eventually, the film dries out due to complete liquid evaporation. Liquid film dryout is the mechanism responsible for the relatively low CHF values associated with saturated boiling in long tubes with low inlet subcooling.

High mass velocity flow in a short tube with high inlet subcooling results in subcooled boiling and higher CHF values as illustrated by the tube on the right-hand side of Fig. 4. Like the previous case, the flow is characterized by an inlet region of single-phase convection until the onset of nucleate boiling. Once nucleation begins, very small bubbles are formed creating a thin bubble boundary layer, and bubbles migrating toward the core quickly condense. The core temperature rises as a result of the energy transfer; however, the flow remains in the subcooled boiling region over its entire heated length. CHF can occur while the thermodynamic equilibrium quality is well below zero and is commonly referred to as departure from nucleate boiling (DNB). For high-flux

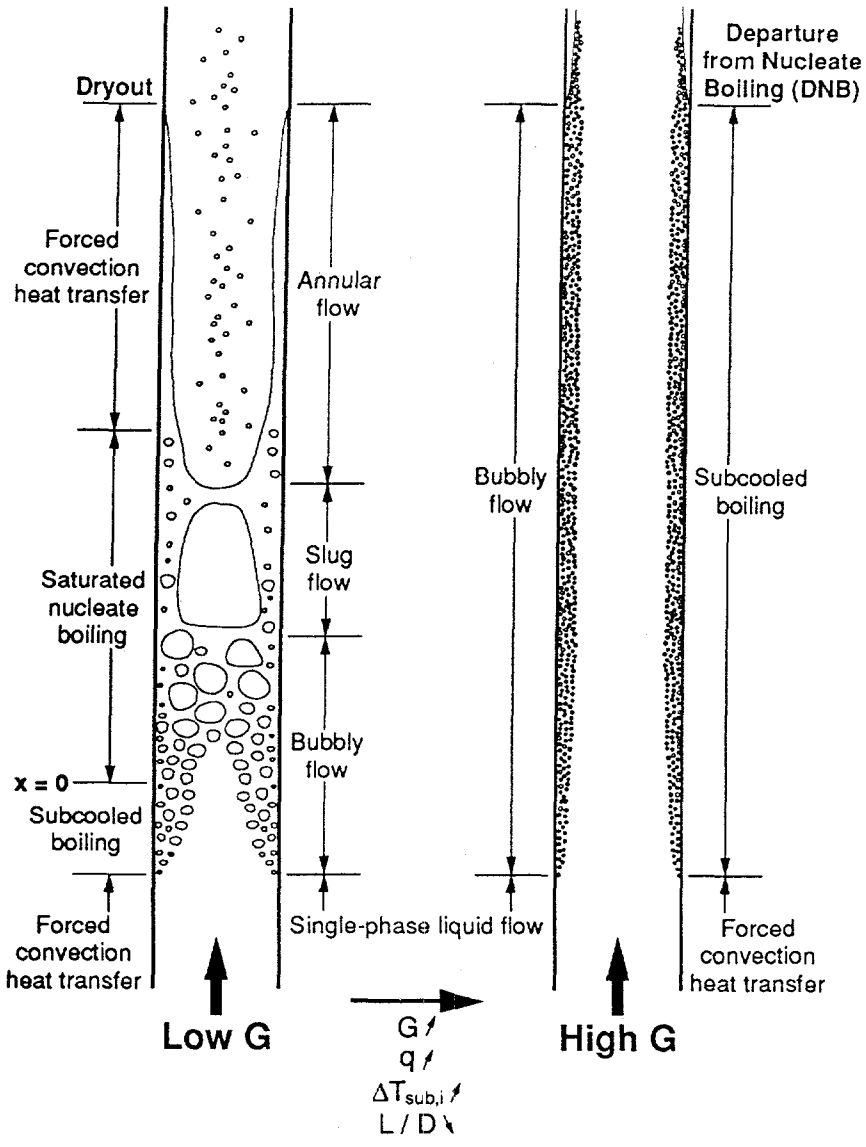

Figure 4. CHF in Low and High Mass Velocity Flows.

DNB, the term "burnout heat flux" is also used because physical destruction of the system will occur as a result of a large wall temperature excursion.

Previous studies have shown that CHF in any two-phase cooling configuration generally depends upon key parameters which include working fluid, geometry, mass velocity, subcooling, and pressure. Only a few studies have been published on the ultra-high CHF regime: Bergles [6], Ornatskii and Vinyarskii [7], Celata *et al.* [8] and Vandervort *et al.* [9].

A comprehensive review of prior ultra-high CHF work by the author has revealed many inconsistencies between the findings of earlier investigators which can be traced to one or more of the following: (1) inability to isolate the effects of key parameters while keeping all others constant, (2) very few short heated length-to-diameter ratio data, (3) inability to attain very high mass velocities (no data exist for mass velocities over 90,000 kg m^{-2} s^{-1}), and (4) inability to cover a broad range of pressures, especially for high mass velocities. While gaps in the data from previous studies were the result of poor isolation of parametric effects, most are actually due to limitations of the experimental apparatus used (e.g., limited pump pressure and/or flow rate capability, power supply limitations, test section construction).

In the present study, an experimental facility was designed to overcome the aforementioned limitations of prior ultra-high CHF work. The results of an extensive experimental investigation of CHF for water flow in small diameter tubes of short heated length are presented. Also included is a new correlation for accurate determination of ultra-high CHF.

EXPERIMENTAL METHODS

The present study demanded a flow loop capable of withstanding pressures nearing the critical point. Water was fed from a large reservoir to a high pressure piston pump which both increased the pressure and circulated the fluid through the loop. The high pressure pump consisted of three pistons operating out of phase to deliver a steady 15.1 liter min^{-1} (4 gpm) stream of water at a maximum pressure of 206.8 bars (3000 psi). A portion of the flow entered the test section while the balance returned to the reservoir through a by-pass.

The test section shown in Fig. 5 consisted of inlet and outlet power/instrumentation blocks that were identical in construction and designed for convenient connection to the test section using compression fittings. Each block was fabricated from two stainless steel plates separated by a thick plate of G-7 fiberglass plastic. One stainless steel plate in each block served as an electrode for electrical current flow from the power lead to the test section. The other stainless steel plate in each block was machined with pressure and temperature instrumentation ports in addition to a threaded connection for attaching a compression fitting for the water inlet or outlet. The detail in Fig. 5 shows an AISI stainless steel 304 (or Cu-Ni 30%) capillary tube silver soldered to copper support pieces at each end. Power cables from a d.c. power supply were connected to the two stainless steel plates mounted to the tube ends. Heat was generated in the tube by passing an electrical current as high as 700 amperes at 20 volts.

RESULTS

Test Conditions

Ultra-high CHF demands very high mass velocity flow of subcooled water through short, small diameter tubes at elevated pressures. Because of experimental difficulties, ultra-high CHF data (above 10 MW m^{-2}) are very limited. The present investigation incorporated a facility which overcame many of the difficulties encountered by prior investigators in obtaining such data. The

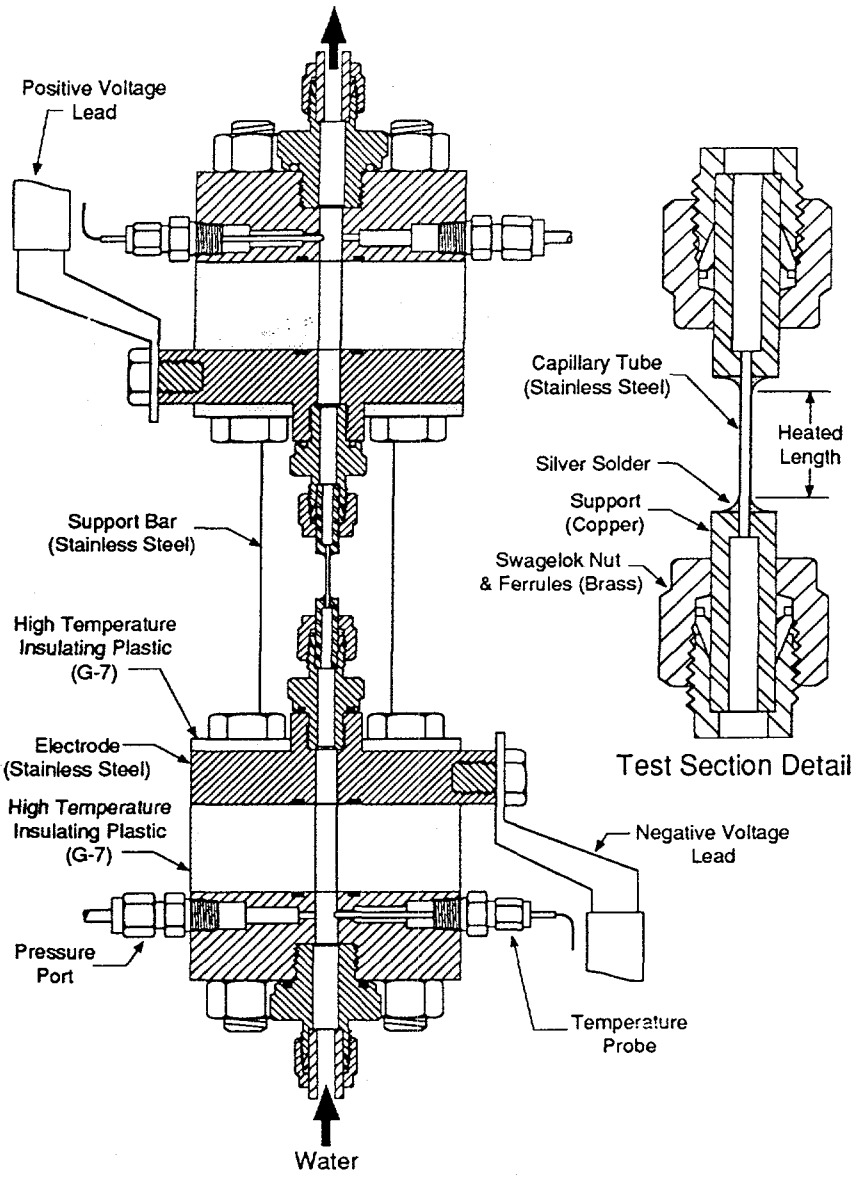

Figure 5. Schematic of Test Section.

unique attributes of this facility enabled testing at pressures approaching the critical point, reaching very high mass velocities, and accommodating the high pressure drops associated with high mass velocity flow through small diameter tubes. The present study also included very short heated lengths because previous studies have shown decreasing heated length can greatly increase CHF. Aside from attempting to fill a data gap in the CHF literature, specific tests were performed to build a broad range of ultra-high CHF data which address the parametric effects of mass velocity, heated length, tube diameter, pressure, and subcooling on CHF.

The bulk of the data was obtained for tube diameters of 0.406 and 0.902 mm and a heated length of about 5.6 mm; however, additional tests were performed with tube diameters as large as 2.54 mm and heated lengths up to 30.8 mm. The present study covered very broad ranges of mass velocity (G = 5000 to 134,000 kg m^{-2} s^{-1}) and pressure (P_o = 2.5 to 172.4 bars). Figure 6 shows in a mass velocity - pressure plane the present ultra-high CHF study containing a much greater number of high mass velocity and high pressure/high mass velocity data than the prior ultra-high CHF studies. The corresponding CHF values ranged from 9.4 to 276 MW m^{-2}, the upper limit being the highest CHF ever reported in the literature for a uniformly heated tube. This value surpasses the prior CHF record of 228 MW m^{-2} achieved by Ornatskii and Vinyarskii [7].

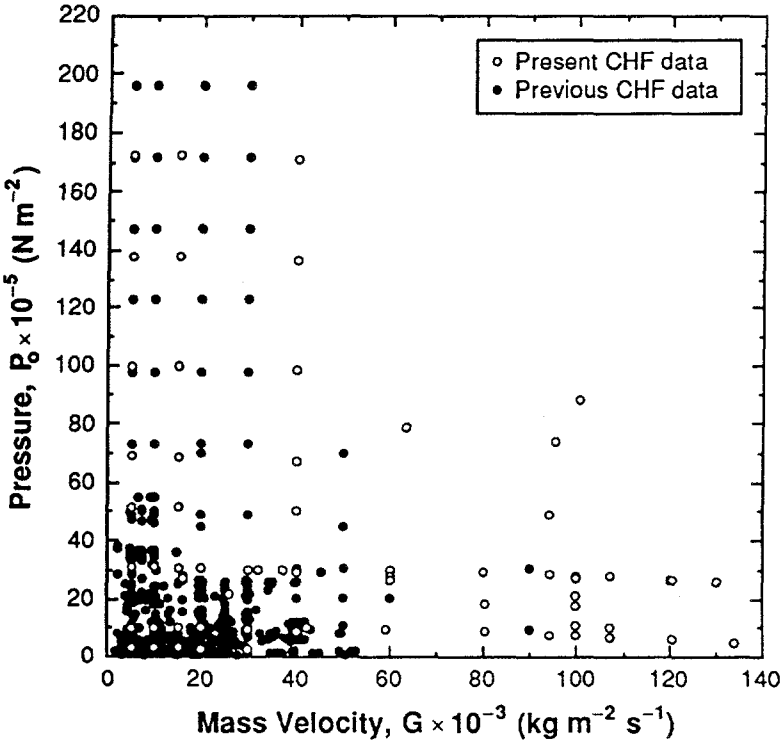

Figure 6. Subcooled High-CHF Data in the Mass Velocity - Pressure Plane.

Pressure Drop Characteristics

Pressure drop results for ultra-high heat flux conditions are presented in Fig. 7. Shown is the pressure drop versus heat flux at mass velocities of 40,000 and 100,000 kg m^{-2} s^{-1} for three different tube diameters. Also indicated is the length-to-diameter ratio for each based on both the heated length, L, and total length, L_t, which includes the unheated inlet and outlet regions of the tube. Referring to the three cases corresponding to the lower mass velocity, the pressure drop increased with decreasing tube diameter with the smallest diameter of 0.406 mm yielding a total pressure drop of approximately 20 bars. An increase in mass velocity to 100,000 kg m^{-2} s^{-1}

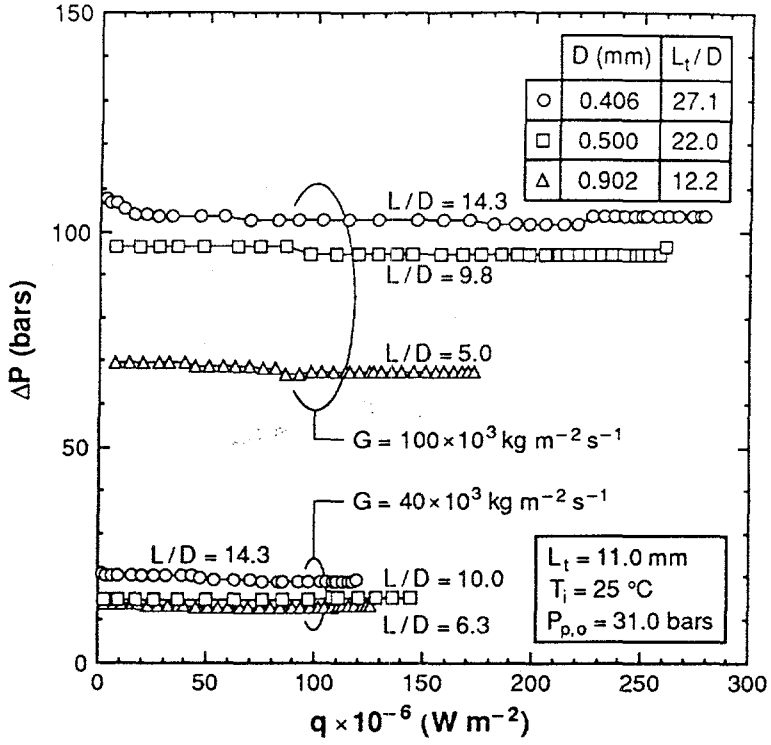

Figure 7. Effect of Heat Flux on Pressure Drop at High Mass Velocities.

resulted in large increases in pressure drop for all three diameters with the smaller diameter yielding a very high pressure drop in excess of 100 bars. Ultra-high heat fluxes above 200 MW m^{-2} were achieved only with very high mass velocities similar to those represented in Fig. 7 at the expense of very large pressure drops. However, in each case, there was little variation in pressure drop over the entire range of heat flux up to CHF. Beginning at low heat fluxes, where the flow was that of pure liquid, an increase in heat flux caused a slight decrease in pressure drop due to a reduction in liquid viscosity with increasing temperature. This trend was generally sustained until the heat flux neared CHF where a slight rise in the pressure drop was detected.

These cases are representative of the bulk of the data obtained in this study and clearly show that high pressure drop should be of great concern when designing a cooling system for ultra-high heat flux dissipation. Under these conditions, the coolant enters the test section subcooled and, as a result of the large mass velocity required to achieve ultra-high CHF, the flow remains subcooled at the exit, resulting in a predominantly single-phase pressure drop. Thus, a simple single-phase model seems most suitable for predicting the pressure drop for these conditions.

Parametric Trends

As indicated above, the present ultra-high CHF data were acquired over broad ranges of both flow and geometrical parameters. A key tactic in the study was to explore the individual effects of key parameters while keeping all other parameters unchanged. The key parameters

include tube diameter, heated length-to-diameter ratio, mass velocity, subcooling, and pressure. Only representative effects of tube diameter and mass velocity are presented here.

The effect of tube diameter for constant values of heated length, inlet temperature, and outlet plenum pressure is illustrated in Fig. 8. CHF data are shown for four mass velocities ranging from 20,000 to 100,000 kg m^{-2} s^{-1}. The plot shows a consistent trend of increasing CHF with decreasing tube diameter.

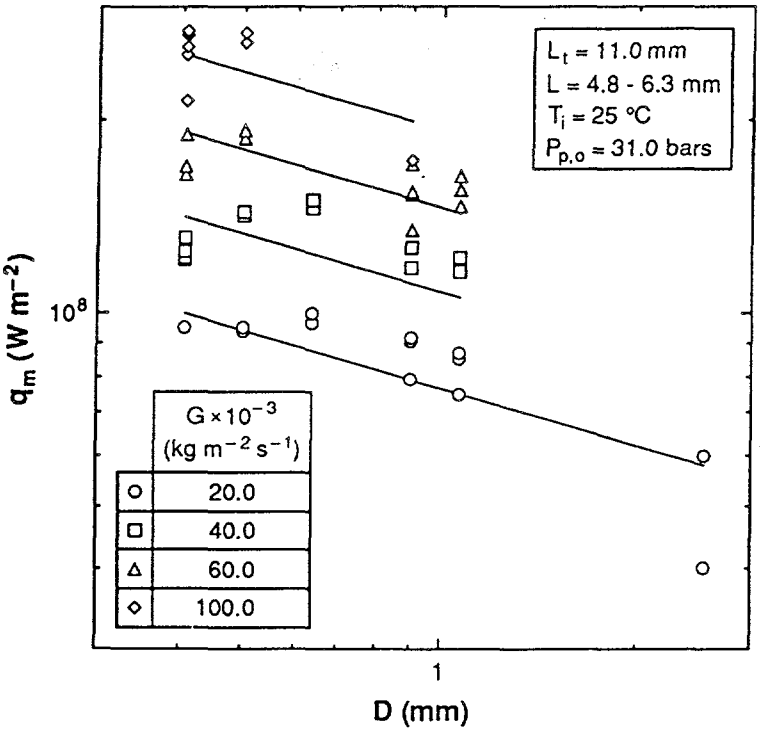

Figure 8. Effect of Diameter on CHF.

The effect of mass velocity on CHF at $P_{p,o}$ = 31.0 bars is presented in Fig. 9 for tubes of D = 0.406 and 0.902 mm with equal lengths. A broad range of mass velocity is shown, from a moderate value of 5000 to a large value of 130,000 kg m^{-2} s^{-1}, which surpasses the mass velocities of any previous CHF study. Figure 9 shows CHF is proportional to $G^{0.446}$, with the smaller tube diameter yielding a higher CHF, despite its greater L/D ratio.

CHF Correlation

A new CHF correlation [10] was formulated for the ultra-high CHF conditions of this and previous studies,

$$Bo = \frac{0.0332\,We_D^{-0.235}\left(\frac{\rho_f}{\rho_g}\right)^{-0.681}\left[1-0.684\left(\frac{\rho_f}{\rho_g}\right)^{0.832}x_i\right]}{1+0.0908\,We_D^{-0.235}\left(\frac{\rho_f}{\rho_g}\right)^{0.151}\left(\frac{L}{D}\right)}, \quad (1)$$

where $Bo = q_m / G.h_{fg}$, $We_D = G^2\,D / \rho_f.\sigma$, x_i is the inlet thermodynamic equilibrium quality, and ρ_f, ρ_g, σ, and h_{fg} are, respectively, the liquid density, vapor density, surface tension, and latent heat of vaporization. This correlation contains only five adjustable constants in contrast to the large number of constants required by previous CHF correlations. As shown in Fig. 10, the mean absolute and RMS errors for equation (1) relative to all available ultra-high CHF data are 15.1% and 19.5%, respectively, 29% and 32% less than the next most accurate correlation available from previous literature [11].

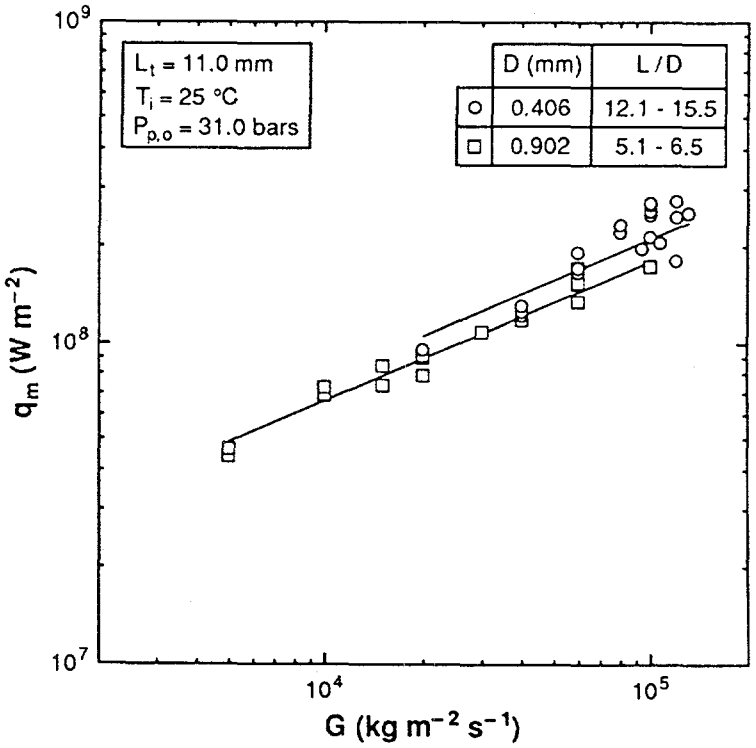

Figure 9. Effect of Mass Velocity on CHF for Two Diameters.

CONCLUSIONS

Ultra-high CHF data were obtained to ascertain the effects of tube diameter, heated length-to-diameter ratio, mass velocity, subcooling, and pressure on CHF. Key findings from the study are as follows:

(1) Ultra-high CHF increases with increasing mass velocity, increasing subcooling, decreasing tube diameter, and decreasing heated length-to-diameter ratio.

(2) Pressure drop for flow boiling at high mass velocity in a short, small diameter tube varies little from the adiabatic single-phase pressure drop, proving CHF is triggered even with negligible net vapor production. Thus, a simple single-phase model seems most suitable for predicting the pressure drop for these conditions.

(3) Ultra-high CHF values in excess of 100 MW m^{-2} can be achieved with subcooled water flow at high mass velocities ($G > 40{,}000$ kg m^{-2} s^{-1}) in small diameter tubes ($D < 1$ mm) of short heated lengths ($L < 7$ mm). The present study yielded the highest recorded CHF value (276 MW m^{-2}) for flow boiling of water in a uniformly heated tube, surpassing Ornatskii and Vinyarskii's [7] prior record of 228 MW m^{-2}.

(4) A new CHF correlation was developed whose accuracy surpasses those of all previous correlations in predicting ultra-high CHF data.

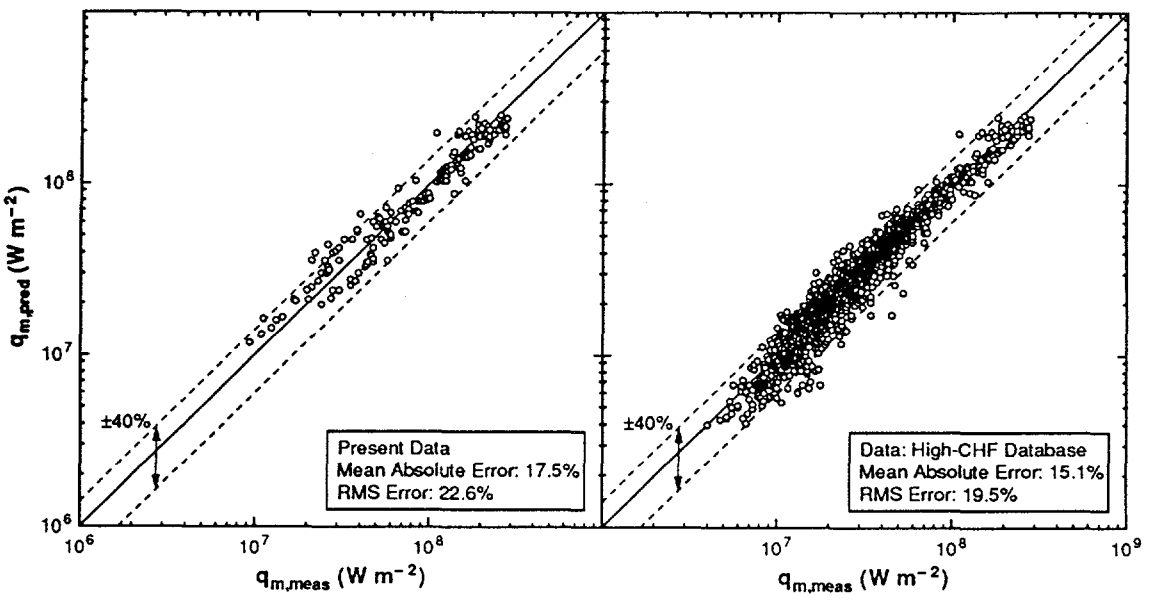

Figure 10. CHF Correlation [10].

ACKNOWLEDGMENT

The author is grateful for the support of the Office of Basic Energy Sciences of the U.S. Department of Energy (Grant No. DE-FG02-93ER14394.A003).

REFERENCES

1. M.B. BOWERS and I. MUDAWAR, "High Flux Boiling in Low Flow Rate, Low Pressure Drop Mini-Channel and Micro-Channel Heat Sinks," *Int. J. Heat Mass Transfer* 37, 321 (1994).
2. M.B. BOWERS and I. MUDAWAR, "Two-Phase Electronic Cooling using Mini-Channel and Micro-Channel Heat Sinks. Part I. Design Criteria and Heat Diffusion Constraints," *ASME J. Electronic Packaging* 116, 290 (1994).
3. M.B. BOWERS and I. MUDAWAR, "Two-Phase Electronic Cooling using Mini-Channel and Micro-Channel Heat Sinks. Part II. Flow Rate and Pressure Drop Constraints," *ASME J. Electronic Packaging* 116, 298 (1994).
4. R.D. BOYD, "Subcooled Flow Boiling Critical Heat Flux (CHF) and its Application to Fusion Energy Components. Part I. A Review of Fundamentals of CHF and Related Data Base," *Fusion Technology* 7, 7 (1985).
5. P.E. JIMENEZ and I. MUDAWAR, 1994, "A Multi-Kilowatt Immersion-Cooled Standard Electronic Clamshell Module for Future Aircraft Avionics," *ASME J. Electronic Packaging* 116, 220 (1994).
6. A.E. BERGLES, "Subcooled Burnout in Tubes of Small Diameter," ASME Paper No. 63-WA-182 (1963).
7. A.P. ORNATSKII and L.S. VINYARSKII, "Heat Transfer Crisis in a Forced Flow of Underheated Water in Small-Bore Tubes," *Teplofizika Vysokikh Temperatur* 3, 444 (1965).
8. G.P. CELATA, M. CUMO and A. MARIANI, "Burnout in Highly Subcooled Water Flow Boiling in Small Diameter Tubes," *Int. J. Heat Mass Transfer* 36, 1269 (1993).
9. C.L. VANDERVORT, A.E. BERGLES and M.K. JENSEN, "An Experimental Study of Critical Heat Flux in Very High Heat Flux Subcooled Boiling," *Int. J. Heat Mass Transfer*, 37 (Suppl. 1), 161 (1994).
10. D.D. HALL and I. MUDAWAR, "Ultra-High Critical Heat Flux (CHF) for Subcooled Water Flow Boiling - II. High-CHF Database and Design Equations," *Int. J. Heat Mass Transfer*, in review.
11. M.M. SHAH, "Improved General Correlation for Critical Heat Flux during Upflow in Uniformly Heated Vertical Tubes," *Int. J. Heat Fluid Flow* 8, 326 (1987).